Max-Planck-Institut für Meteorologie
Max Planck Institute for Meteorology

MAX-PLANCK-GESELLSCHAFT

Simulation of Low-Frequency Climate Variability in the North Atlantic Ocean and the Arctic

Helmuth Haak

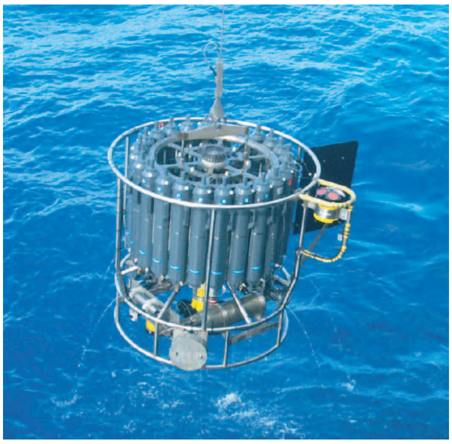

Berichte zur Erdsystemforschung

Reports on Earth System Science

Hinweis

Die Berichte zur Erdsytemforschung werden vom Max-Planck-Institut für Meteorologie in Hamburg in unregelmäßiger Abfolge herausgegeben.

Sie enthalten wissenschaftliche und technische Beiträge, inklusive Dissertationen.

Die Beiträge geben nicht notwendigerweise die Auffassung des Instituts wieder.

Die "Berichte zur Erdsystemforschung" führen die vorherigen Reihen "Reports" und "Examensarbeiten" weiter.

Notice

The Reports on Earth System Science are published by the Max Planck Institute for Meteorology in Hamburg. They appear in irregular intervals.

They contain scientific and technical contributions, including Ph. D. theses.

The Reports do not necessarily reflect the opinion of the Institute.

The "Reports on Earth System Science" continue the former "Reports" und "Examensarbeiten" of the Max Planck Institute.

Anschrift / Address

Max-Planck-Institut für Meteorologie
Bundesstrasse 53
20146 Hamburg
Deutschland

Tel.: +49-(0)40-4 11 73-0
Fax: +49-(0)40-4 11 73-298
Web: www.mpimet.mpg.de

Layout:

Bettina Diallo, PR & Grafik

Titelfotos:
vorne:
Christian Klepp - Jochem Marotzke - Christian Klepp
hinten:
Clotilde Dubois - Christian Klepp - Katsumasa Tanaka

Berichte zur Erdsytemforschung 1/2004

Simulation niederfrequenter Klimavaribilität im nordatlantischen Ozean und der Arktis

Simulation of Low-Frequency Climate Variability in the North Atlantic Ocean and the Arctic

Dissertation zur Erlangung des Doktorgrades der Naturwissenschaften
im Fachbereich Geowissenschaften der Universität Hamburg
vorgelegt von

Helmuth Haak

Hamburg 2004

Reports on Earth System Science 1/2004

ISSN 1614-1199

Helmuth Haak
Max-Planck-Institut für Meteorologie
Bundesstrasse 53
20146 Hamburg
Germany

Als Dissertation angenommen
vom Fachbereich Geowissenschaften der Universität Hamburg

auf Grund der Gutachten von
Herrn Prof. Dr. Jens Meincke und
Herrn Prof. Dr. Mojib Latif

Hamburg, den 05. Juli 2004

Professor Dr. Helmut Schleicher
Dekan des Fachbereiches Geowissenschaften

ISSN 1614-1199

Simulation of Low-Frequency Climate Variability in the North Atlantic Ocean and the Arctic

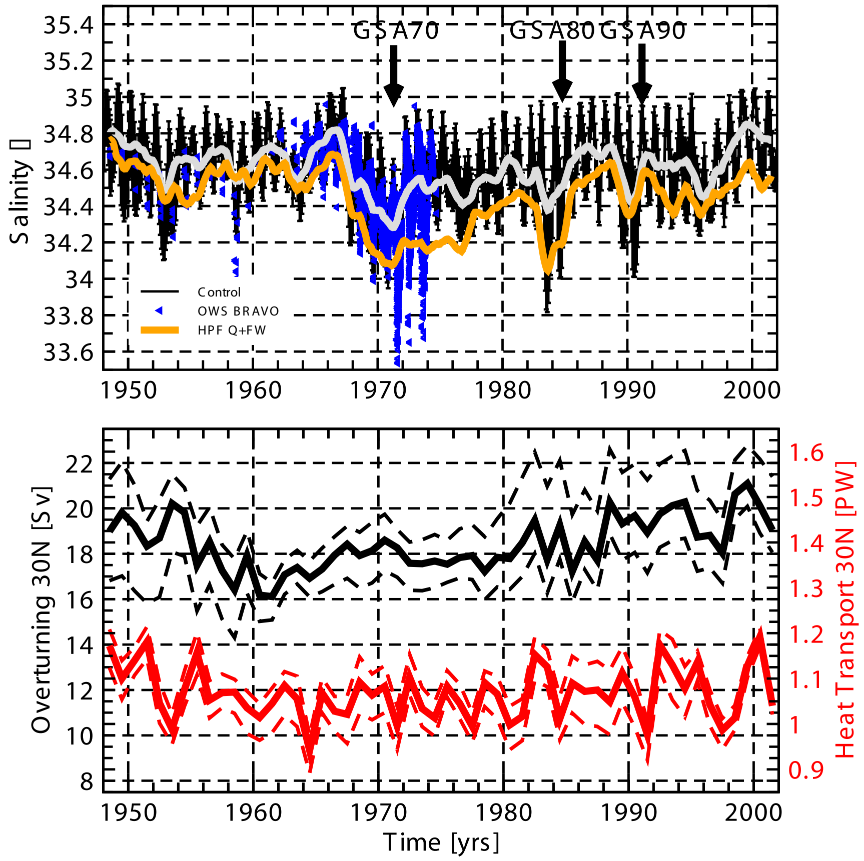

Helmuth Haak

Hamburg 2004

CONTENTS

Abstract

Low-frequency variability in large scale North Atlantic/Arctic properties like Meridional Overturning Circulation, heat transport, deep water formation, overflows, sea ice volume, thickness and extent, as well as the Arctic fresh water budget are studied by means of ensemble simulations with the global coupled ocean/sea ice model MPI-OM forced by realistic daily atmospheric forcing data from the NCEP/NCAR Reanalysis for the period 1948-2001. Major findings are that wintertime deep convection in the Labrador Sea is dominated by atmospheric forcing, in particular by the North Atlantic Oscillation. Intensified Labrador Sea convection induces substantial changes in the Labrador Sea Water (LSW) properties, in particular colder, fresher and denser LSW. The simulation links these changes to an increase in the Atlantic Meridional Overturning Circulation (MOC) strength. However, Labrador Sea deep convection is also strongly influenced by the presence of surface salinity anomalies, which originate from anomalous Fram Strait sea ice export events. These export events are shown to be mainly wind driven and are the most probable cause of the observed Great Salinity Anomalies of the 70th, 80th and 90th. In contrast to the Labrador Sea deep convection, the Greenland-Island-Norwegian (GIN) Sea deep convection shows a less clear imprint of the North Atlantic Oscillation variability. In the simulation, inter-annual to decadal variability in the Atlantic MOC circulation has its origin in the Labrador Sea, while longer term multi-decadal trends in the MOC are governed by the properties of the overflow waters from the GIN Sea. During the simulation period the strength of both overflows decreased, while the overflow water density increased. On one hand low-frequency variability of the Arctic sea ice volume is related to sea ice thickness changes, driven in equal parts through variability of atmospheric thermal and fresh water fluxes, and on the other hand through variability of the wind field. While there is a clear decrease of Arctic sea ice volume during the 1990s, there is no such trend present over the full simulation period. Arctic fresh water budget variability in the simulation is dominated by exports of sea ice via Fram Strait, while the sea ice exports are governed by variability of zonal planetary waves. Generally large parts of the observed low frequency variability in the North Atlantic/Arctic can be understood as a passive response of the ocean/sea ice system to variability of the large scale atmospheric forcing.

Zusammenfassung

Niederfrequente Veränderungen großskaliger Eigenschaften des Nordatlantischen und Arktischen Ozeans (z.B. meridionale Umwälzzirkulation (MOC), meridionaler Wärmetransport, Tiefenwasserbildung, Overflows, Meereisvolumen, -dicke und -ausdehnung, sowie das arktische Frischwasserbudget) werden mittels Ensemblesimulationen mit einem globalen Ozean-Meereismodell studiert. Das Modell wird hierzu mit realistischen, täglichen, atmosphärischen Antriebsfeldern aus den NCEP/NCAR Reanalysen für den Zeitraum 1948-2001 integriert. Ein wichtiges Resultat der Experimente ist, daß winterliche Tiefenkonvektion in der Labradorsee (LS) durch die Variabilität des atmosphärischen Antriebs, insbesondere durch die niederfrequenten Schwankungen der Nordatlantischen Oszillation (NAO), beherrscht wird. Die intensivierte Labradorseekonvektion in der zweiten Hälfte des Experiments verursacht erhebliche Veränderungen in den Eigenschaften des Labradorseewassers (LSW), insbesondere wird ein Trend zu kälterem, frischerem und dichterem LSW simuliert. Die Simulation verbindet diese Änderungen mit einer Zunahme der Stärke der atlantischen MOC. Labradorseekonvektion wird ebenfalls durch Anomalien des lokalen Oberflächensalzgehalts beeinflusst, die aus unregelmässigen Schwankungen des arktischen Frischwasserexports entstehen. Es wird gezeigt, daß die Schwankungen des Framstraßen Meereisexports hauptsächlich windgetrieben, und die wahrscheinlichste Ursache der beobachteten großen Salzgehaltsanomalien der 70er, 80er und 90er Jahre in der LS sind. Im Gegensatz zur LS zeigt die Tiefenkonvektion in der Grönland-Island-Norwegen See (GIN) einen weniger klaren Einfluss der NAO. In der Simulation entstammt die zwischenjährliche bis dekadische Veränderlichkeit der atlantischen MOC hauptsächlich der LS, während längerfristige multi-dekdische Tendenzen vorallem durch Veräbnderungen der Eigenschaften der Overflows hervorgerufen werden. Während des simulierten Zeitraumes verringert sich die Stärke beider Overflows, während sich die Dichte der Overflow Wassermassen jedoch erhöht. Die simulierte niederfrequente Veränderlichkeit des arktischen Meeeisvolumens spiegelt Änderungen der Meereisdicke wieder, welche zu etwa gleichen Teilen durch Veränderlichkeit der atmosphärischen Wärme- und Frischwasserflüsse und durch Veränderlichkeit des Windfeldes hervorgerufen werden. Während es eine deutliche Abnahme des arktischen Meereisvolumens in den neunziger Jahren gibt, existiert kein klarer negativer Trend über den vollen Simulationszeitraum. Veränderungen des arktischen Frischwasserbudgets werden durch Exporte von Meereis aus der Framstraße beherrscht. Diese wiederum werden durch Schwankungen des atmosphärische Massenfelds erzeugt, welche sich durch die Variabilität atmosphärischer, zonaler, planetarer Wellen beschreiben lassen.

1. INTRODUCTION

1.1 The Role of the North Atlantic/Arctic Region in Global Climate

The ocean is an essential component of the Earth's climate system. First it provides the largest reservoir for the most important constituents like heat, fresh water and carbon. Secondly, it exchanges these constitutes with the overlying atmosphere and redistributes them - acting as a powerful regulator of the climate system. With respect to these ocean atmosphere exchanges, the North Atlantic is a key region for global climate. In its high latitude sinking regions, surface waters are transformed into denser deep water masses due to buoyancy loss and mixing, and ventilate the abyssal ocean. Associated with this is a global scale oceanic Meridional Overturning Circulation (MOC), also referred as Thermohaline Circulation (THC) or 'conveyor belt circulation' (Broecker, 1991). This circulation brings warm water northward into high latitudes and cold water southward into low latitudes, therefore reducing the equator to pole temperature gradient. The MOC connects the North Atlantic to the tropical Atlantic and, via the Southern Ocean, to all other ocean basins. Its intermediate depth branch is mainly fed by North Atlantic Deep Water (NADW), produced by the process of wintertime deep convection in the Labrador Sea, and mixing of ambient waters with the two dense overflows across the Greenland Scotland Ridge, namely the Island-Scotland Overflow Water (ISOW) and the Denmark Strait Overflow Water (DSOW) (Dickson and Brown, 1994). The overflows are fed by intermediate and deep water formation processes in the Greenland-Island-Norwegian (GIN) Sea and the Arctic Ocean (Mauritzen, 1996). The deeper part of the NADW also contains small amounts of cold abyssal waters originating in the Southern Hemisphere (McCartney, 1992). The lower limb of the Atlantic MOC forms the Deep Western Boundary Current (DWBC), flowing southward at intermediate depth (1000m-4000m). It is balanced by a warm northward surface flow in the upper 1000m, the North Atlantic's western boundary current, namely the Gulf Stream/North Atlantic Current. These currents form the upper limb of the Atlantic 'conveyor belt'. They are responsible for much of the poleward heat transport, peaking at appr. 1.2 PW at 24°N (Hall and Byrden, 1982; Macdonald and Wunsch, 1996a; Ganachaud and Wunsch, 2000; Talley, 2002). Variability of it's intensity and it's pathway influence European and global climate, mainly due to the associated northward transport of heat (e.g. Maier-Reimer *et al.* (1993); Rahmstorf (1996); Broecker (1997); Blanke *et al.* (2001)).

Adjacent to the North Atlantic are two marginal seas: the Arctic Ocean and the European Mediteranian Sea. Both are classified as mediteranian seas due to their limited exchange with the Atlantic, as well as their prominent and complex thermohaline driven circulation (Dietrich *et al.*, 1975), (Meincke *et al.*, 1997). With respect to their fresh water balance their humid (respectively arid) nature strongly influences the Atlantic's hydrography. They provide sources of cold and fresh (or warm and salty in case of the European Mediteranian Sea) deep waters (Aagaard and Carmack, 1989), (Roether *et al.*, 1996). In particular, the Arctic's permanent sea ice cover, it's seasonal melting and freezing together with the associated process of brine/fresh water release, is important for the Atlantic MOC.

1.1.1 Variability in the Atmosphere

The dominant mode of atmospheric variability in the North Atlantic region is the North Atlantic Oscillation (NAO). It is a large scale seesaw of the atmospheric mass distribution between the Subtropical High and the Polar Low. It extends from the surface well into the stratosphere. A circulation index between the two centers of action - the Azores High and the Island Low - was first defined by Defant (1924) and Walker and Bliss (1932). Basically, this index measures the strength of the westerly winds blowing over the North Atlantic between 40°N and 60°N. The standard NAO index uses the normalized pressure difference between observational stations at Stykkisholmur, Island to the north and Lisbon, Portugal, Gibraltar or the Azores in the south. Although, it is mostly pronounced in winter it can be observed throughout the year (Rodgers, 1990). The NAO index varies strongly from year to year, but also exhibits a tendency to remain in one phase for intervals lasting several years (Rodgers, 1990; Hurrel, 1995; Jones *et al.*, 1997).

The positive NAO phase exhibits a stronger than usual Subtropical High pressure center and a deeper than normal Icelandic Low. The increased pressure difference produces more frequent and stronger winter storms, which cross the Atlantic Ocean on a more northerly track. This results in relatively warm and wet winters in Europe and in cold and dry winters in northern Canada and Greenland. The negative NAO index phase shows a weak Subtropical High and a weak Icelandic Low. The reduced pressure gradient results in fewer and weaker winter storms, which cross on a more zonal pathway. In this phase the atmospheric circulation brings more moist air into the Mediterranean region and more cold air to northern Europe. The NAO is not only confined to the North Atlantic region, rather it is hemispheric (Hurrel, 1995). It shows a close relationship to the Arctic Oscillation (AO) index by Thomson and Wallace (1998). Overviews are given by Greatbatch (2000) or Wanner *et al.* (2001).

While the spatial patterns associated with the NAO are fairly robust, it's time evolution - at least in the low-frequency domain - is less clear. The NAO is usually considered as an internal mode of variability of the atmosphere. This view is supported by several studies using numerical models of the atmosphere which are driven by climatological boundary conditions and show white-noise NAO type modes of variability (James and James, 1989). Yet the observed NAO shows slightly red-noise variability, e.g. over the past 30 it has undergone an upward trend slightly in excess of what is expected from a white time series of internal atmospheric variability (Fig. 1.1), suggesting some dependency on external boundary forcing.

Several studies using atmospheric general circulation models driven by observed SST indicate that substantial parts of the inter-annual to multi decadal variability of the NAO can be reproduced (Rodwell *et al.*, 1999; Latif *et al.*, 2000). However, the individual studies do not show a consistent picture for the relative importance of the contribution from different ocean areas, e.g. North Atlantic (Rodwell *et al.*, 1999), North Atlantic as well as tropical- and North Pacific (Latif *et al.*, 2000), tropical Indian and Pacific Ocean (Hoerling *et al.*, 2001), or mainly Indian Ocean (Bader and Latif, 2003). Nevertheless, these studies indicate that low-frequency changes in the ocean's SST may feed back onto the North Atlantic atmosphere variability, possibly involving different mechanisms on different timescales (Sutton and Hodson, 2003). The observed NAO time series has weak spectral peaks at 2-3, 4-6, 8-10 and around 20 years. However, its low-frequency variability is non-stationary (Walter and Graf, 2002; Raible *et al.*, 2001), e.g. enhanced decadal variability occurs just in the later period of the available observations (Fig. 1.1).

An important question in this context is:

How does the North Atlantic ocean respond to low-frequency changes of the NAO ?

1.1.2 Variability in the North Atlantic Ocean

The observational record of the Northern Hemisphere land and sea surface temperatures indicates the existence of inter-annual to multi decadal and longer variablity (Mann *et al.*, 1998). Already Bjerkness (1964) suggested that on inter-annual timescales SST anomalies are locally driven by the

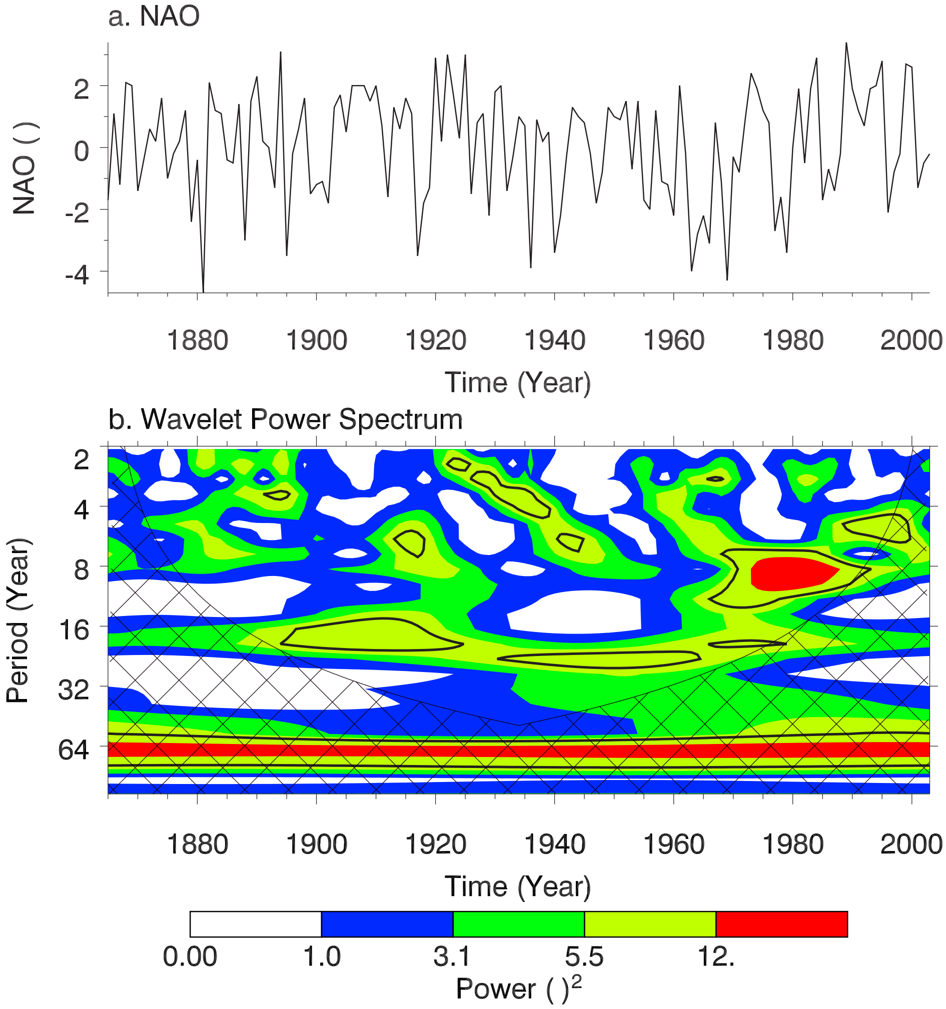

Fig. 1.1: *The upper panel shows the time series of the winter(DJF) NAO Index after Hurrel (1995) for the period 1865-2003. There is a pronounced upward trend between 1960th to the early 1990th superimposed to high inter-annual variability. The lower panel shows a wavelet power spectrum of the time series. The thick black line shows the 90 percent confidence interval for testing against white noise. Note the enhanced decadal variability (with a peak at about 8-10 years) after 1960, and the reduced decadal variability before.*

atmospheric forcing, while on longer time scales changes in the ocean circulation, in particular it's heat transport, become important. Cayan (1992) demonstrates a tri-pole SST pattern forced by atmospheric heat flux related to the NAO. This pattern dominates the inter-annual SST variability and is considered as atmosphere-driven. Sutton and Allen (1997) suggested that ocean-atmosphere coupling is important in generating advectively propagating SST anomalies originating from the tropical Atlantic. On multi decadal time scales the dominant SST pattern has a more homogeneous, monopole structure in the Northern Atlantic (Kushnir, 1994) with an anomaly of opposite sign in the Southern Atlantic. Several numerical model studies associate this pattern with low-frequency variability of the MOC, e.g. Delworth *et al.* (1993); Timmermann *et al.* (1998); Delworth and Mann (2000). Recently Latif *et al.* (2004) related North Atlantic multi decadal SST variability with low-frequency variability of the Atlantic MOC in their coupled climate model, using the same ocean model as in this study.

The lower branch of the Thermohaline Circulation in the Atlantic ocean is driven by two sources: Labrador Sea (LS) wintertime deep convection and the overflows across the Greenland Scotland Ridge mixing with ambient Atlantic water.

Both processes are known to exhibit variability on different timescales reaching from seasonal (and shorter) to multi decadal. The local atmospheric conditions, in particular the NAO, can influence the MOC through it's direct influence on deep water renewal in the LS, e.g. Curry *et al.* (1998) showed a close relationship between the low-frequency variability of the NAO and the thermohaline properties of the Labrador Sea Water (LSW). According to Dickson *et al.* (1996), the NAO triggers the relative importance of the deep water formation regions to the north and to the south of the Greenland Scotland Ridge. When the NAO index is positive the westerly winds are stronger than normal, and outbreaks of cold, dry air from the north over the LS are more frequent. These atmospheric conditions can lead to strong convective overturning in the Labrador Sea, while at the same time the likelihood of deep water renewal in the GIN Sea is reduced. The GIN Sea experiences a less severe winter during NAO high index years. The opposite situation is found when the NAO index is low. Annual to decadal variations in the production of LSW are directly linked to the NAO (Curry and McCartney, 2001). Curry *et al.* (1998) showed that temperature signals in LSW propagate with the Deep Western Boundary Current southward, e.g. they can be observed appr. 6 years later at Bermuda.

Furthermore, the strength of the overflow through Faroer-Bank Channel has been reported to exhibit a decreasing trend during the time spanned in observational record. Associated is a trend towards warmer and fresher overflow water (Hansen *et al.*, 2001). Denmark Strait overflow shows less variability in volume transport (Dickson *et al.*, 1999). Also, it exhibits a freshening (Dickson *et al.*, 2002) and warming (Dickson *et al.*, 1999) trend until the mid 1990th. Measurements at the sill indicate that DSOW salinity decreased between the 1950th to the mid 1990th. However, since 1995 it's salinity is increasing again (Dickson *et al.*, 2002).

Recently, Dickson *et al.* (2002) and Curry *et al.* (2003) show a multi decadal freshening trend in the deep North Atlantic between the 1950th and 1990th. The authors attribute this trend to the freshening of the overflows and an increase in LSW production, as well as an increase in high latitude precipitation, and Arctic fresh water export, and elevated Arctic river runoff. The strength of the Atlantic Subtropical Gyre circulation exhibits low-frequency variability (Curry and McCartney, 2001), e.g. a weaker than normal Gulf Stream/North Atlantic Current during the low NAO index period of the 1960th. Subsequently the gyre strength intensified by appr. 25% during the period of persistently high NAO index after 1970. Salinity of Mediteranien Deep Water increased over the last 40 years (Roether *et al.*, 1996). This trend can be tracked into western mid-depth Atlantic (Curry *et al.*, 2003).

All these observations indicate substantial changes in large scale ocean properties during the second half of the last century.

Important related questions are:

How do the observed hydrographic changes in the LSW and the overflow properties reflect themself in the strength of the MOC ?

Which aspects of the observed changes can/cannot be reproduced by a state-of-the-art Ocean General Circulation Model ?

Has the MOC changed over the last decades or just NADW properties ?

1.1.3 Variability in the Arctic Ocean and Sea Ice

The Arctic is an important fresh water source (Aagaard and Carmack, 1989) that can control the stratification, and therefore the vertical circulation in the North Atlantic sinking regions. Small variations in the fresh water supply from the Arctic, via the East Greenland Current, into the North Atlantic can alter or even stop convection, particularly in the Labrador Sea (Lazier, 1995; Mauritzen and Haekkinen, 1997; Jungclaus *et al.*, 2004). The most prominent examples of this fresh water capping of convection are the Great

Salinity Anomalies (GSA) described by Dickson *et al.* (1988); Lazier (1995); Belkin *et al.* (1998); Häkkinen (2002). However, the formation mechanism of a GSA, as well as it's impact on the strength of the MOC are still under debate (Häkkinen, 1999; Haak *et al.*, 2003; Saenko *et al.*, 2003). Several aspects of the Arctic ocean's response to low-frequency variability of the NAO can be found in Dickson *et al.* (2000). The authors show changes in amount and temperature of Atlantic water inflow to the Arctic via Barents Sea through-flow and West Spitsbergen Current, a decrease in wintertime sea ice extent in the European Subarctic and an increase in annual volume flux of ice through Fram Strait. Variability of the later is of particular interest, since Fram Strait ice exports are the largest known sink for Arctic fresh water (Aagaard and Carmack, 1989). It's high variability (Vinje *et al.*, 1998; Kwok and Rothrock, 1999) is likely affecting the total Arctic fresh water budget. Proshutinsky and Johnson (1997) identified two circulation regimes of the wind driven Arctic ocean circulation, each persisting for appr. 5-7 years. The response of the Beaufort Gyre to these wind regimes may also have a significant role in the variability of the Arctic fresh water budget (Proshutinsky *et al.*, 2002). Recently Cavalieri and Häkkinen (2001) and Cavalieri (2002) showed a close relationship between the sea ice export via Fram Strait and zonal planetary waves in the atmospheric pressure field between 70-80°N. With respect to detection of global warming, changes in Arctic sea ice thickness and volume may be important indicators. Between the 1960-1970th and the 1990th observations indicate a central Arctic sea ice thickness reduction of up to 40% (Rothrock *et al.*, 1999; Wadhams and Davis, 2000). Finally, simulations with increased greenhouse gas emisions (e.g. IPCC Report, 2001) reveal that the Arctic region is most sensitive to global warming.

Important questions are:

What drives the low-frequency variability of the Arctic sea ice properties?

What are the most important components of the Arctic fresh water budget and has the Arctic fresh water export changed?

What is the most likely cause of the GSAs?

2. MODEL DESCRIPTION

2.1 Introduction

The aim of this chapter is to introduce the numerical model used in this study. A complete description of the ocean and sea ice components is given in Marsland *et al.* (2003).

2.2 The Ocean Model MPI-OM

The Hamburg Ocean Primitive Equation model on C-Grid (MPI-OM) is a z-coordinate global general circulation model based on primitive equations for a Boussinesq-fluid on a rotating sphere. It includes parameterizations of sub grid-scale mixing processes like isopycnal diffusion of the thermohaline fields and eddy-induced tracer transport and a bottom boundary layer slope convection scheme. The model contains a free surface and a state of the art sea ice model with viscous-plastic rheology and snow.

2.2.1 Ocean Primitive Equations

The horizontal momentum balance for a hydrostatic Boussinesq fluid on a rotating sphere is

$$\frac{d\vec{v}_o}{dt} + f(\vec{k} \times \vec{v}_o) = -\frac{1}{\rho_w}\left[\vec{\nabla}_H(p + \rho_w g\zeta)\right] + \vec{F}_H + \vec{F}_V \tag{2.1}$$

where $\vec{v}_o = (u_o, v_o)$ is the oceanic horizontal velocity vector on the orthogonal coordinates, t is the time, f is the Coriolis parameter, $\vec{k}$ is a unit vector normal to the earth's center, ρ_w is a constant reference density, $\vec{\nabla}_H$ is the horizontal gradient operator, p is the internal pressure, g is the acceleration due to gravity and ζ is the sea surface elevation. The total derivative is given by $\frac{d}{dt} = \frac{\partial}{\partial t} + \vec{v}_o \cdot \vec{\nabla}_H + w_o \cdot \frac{\partial}{\partial z}$ where w_o is the vertical component of ocean velocity and $\frac{\partial}{\partial z}$ is the vertical partial derivative. $\vec{F}_H$ and $\vec{F}_V$ are parameterizations of horizontal and vertical eddy viscosity, respectively.

Diagnostic treatment of pressure and density is used to close the momentum balance. Density ρ is taken to be a function of model pressure, temperature and salinity according to the equation of state polynomial defined by the Joint Panel on Oceanographic Tables and Standards (UNESCO, 1983). Potential temperatures are converted to *in situ* temperatures for the density calculation. The pressure is calculated using the hydrostatic equation

$$\frac{\partial p}{\partial z} = -g\rho \tag{2.2}$$

Forward integration of the ocean model surface elevation is based on a linearized kinematic boundary condition stating that the time rate of change of surface elevation is equal to the vertical component of oceanic velocity at the surface.

$$\frac{\partial \zeta}{\partial t} = w_o|_{z=\zeta} \tag{2.3}$$

The vertical velocity is calculated from the horizontal velocity field using the incompressibility condition.

$$\frac{\partial w_o}{\partial z} = -\vec{\nabla}_H \cdot \vec{v}_o \tag{2.4}$$

Integrating over the entire depth gives the vertical velocity at the sea surface.

$$w_o|_{z=\zeta} = -\vec{\nabla}_H \cdot \int_{-H}^{\zeta} \vec{v}_o \, dz \tag{2.5}$$

Potential temperature θ and salinity S obey the advection-diffusion equations

$$\begin{aligned} \frac{d\theta}{dt} &= \vec{\nabla}_H \cdot \left(\mathbf{K}\vec{\nabla}_H \theta\right) && (2.6) \\ \frac{dS}{dt} &= \vec{\nabla}_H \cdot \left(\mathbf{K}\vec{\nabla}_H S\right) && (2.7) \end{aligned}$$

where the tensor $\mathbf{K}$ is a sub grid-scale parameterization of horizontal/isoneutral and vertical/dianeutral diffusion.

2.2.2 Ocean Sub Grid-Scale Parameterizations

The coarse horizontal and vertical resolution of OGCMs necessitates the use of sub grid-scale parameterizations. MPI-OM currently has formulations for Bottom Boundary Layer (BBL) slope transport, horizontal and vertical viscosity, vertical and isopycnal diffusivity, eddy-induced mixing, and convection, as described below.

The Thermohaline Circulation of the world's ocean is maintained by the sinking of dense water masses in high latitudes. In most cases these water masses form in marginal seas or on shelves and slide down the continental slopes. One particular phenomenon is the 'overflow', where dense near-bottom waters cross sills between ocean basins (e.g. Price and Baringer, 1994).

This process is not well resolved in coarse-resolution z-coordinate ocean models owing to a lack of a BBL. In such models the dense water passing over a sill is advected horizontally and placed above lighter water. The resulting convection (parameterized as strong mixing or intensified diffusion) leads to an overestimation of the mixing between the overflow and the ambient water. To overcome this problem Beckmann and Döscher (1997) developed a BBL parameterization where the horizontal flow is redirected as if it flowed along the bottom.

The BBL scheme in MPI-OM is similar to that of Beckmann and Döscher (1997) with two notable exceptions. Firstly, the BBL thickness H_{BBL} may be less than the model layer thickness Δz_s of the source cell. That is,

$$H_{BBL} = \min\left(\Delta z_s, BBL_{max}\right) \tag{2.8}$$

where BBL$_{max}$ is a prescribed maximum thickness. The motivation is to limit the BBL transport in coarse vertical resolution ocean models where the deeper grid cells can be of order 1 km thickness.

Secondly, as suggested by Campin and Goosse (1999) the BBL transport is redirected to a level of neutral buoyancy rather than to the bottom cell of a horizontally adjacent water column. For a source cell having density ρ_s at model level k$_s$, the target cell level k$_t$ is chosen by the following condition.

$$k_t = \begin{cases} k_\rho & if \quad \rho_t \leq \rho_s \quad and \quad \rho_{t+1} > \rho_s \\ k_{bot} & if \quad \rho_{bot} \leq \rho_s \end{cases} \tag{2.9}$$

Here, the subscript *bot* denotes the deepest wet model layer in a target column. The neutral buoyancy approach is particularly useful in regions where coarse horizontal resolution does not allow for a gradual descent on a staircase-like slope. The resultant BBL transport M_{BBL} is given by

$$M_{BBL} = u_s \Delta x, y H_{BBL} \tag{2.10}$$

where u_s represents the meridional (parallel) velocity in the model level k$_s$, and $\Delta x, y$ represents the parallel (meridional) source cell width. The remaining advective transport M is given by

$$M = u_s \Delta x, y(\Delta z_s - H_{BBL}) \tag{2.11}$$

and is purely horizontal. Although not used in this study, MPI-OM also includes an improved version of the BBL scheme where H_{BBL} is calculated locally depending on the stratification and friction velocity using the formulation of Killworth and Edwards (1999).

The horizontal and vertical eddy viscosity are treated separately. Horizontal eddy viscosity $\vec{F}_H$ is parameterized using a scale-dependent biharmonic formulation

$$\vec{F}_H = -\vec{\nabla}_H \cdot \left(B_H \vec{\nabla}_H \Delta_H \vec{v}_o \right) \tag{2.12}$$

where B_H is a coefficient proportional to the fourth power of the grid spacing.

Vertical eddy viscosity $\vec{F}_V$ is parameterized as

$$\vec{F}_V = \frac{\partial}{\partial z} \left(A_V \frac{\partial}{\partial z} \vec{v}_o \right). \tag{2.13}$$

The eddy coefficient A_V is partially relaxed to the value at the previous time step by use of a time filter to avoid $2\Delta t$ oscillation. Using n and Λ_V to denote the time increment and relaxation coefficient gives:

$$A_V{}^n = (1 - \Lambda_V) A_V{}^{n-1} + \Lambda_V \left(A_{VO} (1 + C_{RA} R_i)^{-2} + A_w + A_b \right). \tag{2.14}$$

The time linear relaxation coefficient Λ_V is set to 0.6 in accordance with past experience.

Following Pacanowski and Philander (PP; 1981) the Richardson number R_i dependent mixing term includes constant coefficients A_{VO} and C_{RA}. A small constant background viscosity representing mixing by internal wave breaking is denoted by A_b. The PP scheme in its classical form underestimates turbulent mixing close to the surface. Therefore an additional parameterization for the wind induced stirring A_w is included. The near surface wind mixing is proportional to the cube of the local 10 m wind speed V_{10m}, and is reduced in proportion to the fractional sea ice cover I. It decays exponentially with depth and depends on the local static stability $\delta_z \rho$.

$$A_w(1) = (1 - I) W_T V_{10m}^3 \tag{2.15}$$

$$A_w(k) = A_w(k-1) \frac{\frac{\lambda}{\Delta z}}{\frac{\lambda}{\Delta z} + \delta_z \rho} e^{\frac{\Delta z}{z_0}} \tag{2.16}$$

where k=2,3,...,k_{bot} is the vertical level and Δz is the level thickness; λ, z_0, and W_T are adjustable parameters which were tuned for optimal mixed layer depths.

Tracer diffusion in Eqns. 2.6 and 2.7 is represented in two optional ways. The diffusion tensor **K** can be chosen either to represent:

a) standard horizontal/vertical diffusion

$$\mathbf{K} = D_H \begin{bmatrix} 1 & 0 & 0 \\ 0 & 1 & 0 \\ 0 & 0 & \epsilon \end{bmatrix} \tag{2.17}$$

with $\epsilon = \frac{D_V}{D_H}$; or

b) isoneutral/dianeutral diffusion

$$\mathbf{K} = D_H \begin{bmatrix} 1 & 0 & S_x \\ 0 & 1 & S_y \\ S_x & S_y & \epsilon + S_{dif}^2 \end{bmatrix} \tag{2.18}$$

with $\epsilon = \frac{D_V}{D_H}$ and $S_{dif} = (S_x, S_y, 0) = (\frac{-\delta_x \rho}{\delta_z \rho}, \frac{-\delta_y \rho}{\delta_z \rho}, 0)$.

The transformation follows Redi (1982) with the small slope approximation by Gent *et al.* (1995). The scheme is numerically implemented following Griffies (1998). All the experiments presented in this study utilize isoneutral/dianeutral diffusion.

The effect of tracer mixing by advection with the unresolved mesoscale eddies is parameterized after Gent et al. (1995).

The vertical eddy diffusivity coefficient D_V is treated similarly to Eqn. 2.14, except for the cubic dependence on the shear instability-dependent (Richardson number) term:

$$D_V{}^n = (1 - \Lambda_D) \, D_V{}^{n-1} + \Lambda_D \left(D_{VO} \, (1 + C_{RD} R_i)^{-3} + D_w + D_b \right). \tag{2.19}$$

As with the vertical viscosity, D_{VO}, C_{RD} and the small background term D_b are constant. The wind-induced term D_w is treated in the same manner as for viscosity.

There are several choices for parameterization of convection currently available in the MPI-OM model. Convective adjustment follows Bryan (1969). Traditionally this technique involved the full mixing of vertically adjacent grid cells in the presence of static instability. The MPI-OM formulation is similar but only mixes the upper grid cell with an equivalent thickness of the lower grid cell. This approach aims to increase the penetrative depth of convection.

The scheme used in this study, is the parameterization of convection by greatly enhanced vertical diffusion in the presence of static instability (e.g. Marotzke, 1991; Klinger at al., 1996). Such an approach avoids the excessive intermediate mixing associated with the traditional adjustment scheme by introducing a timescale associated with the choice of (constant) convective-diffusion coefficient.

2.2.3 Sea Ice Dynamics and Thermodynamics

Sea ice motion is determined by a two-dimensional momentum balance equation.

$$\frac{d\vec{v}_i}{dt} + f(\vec{k} \times \vec{v}_i) = -g\vec{\nabla}\zeta + \frac{\vec{\tau_a}}{\rho_i h_i} + \frac{\vec{\tau_o}}{\rho_i h_i} + \vec{\nabla} \cdot \sigma_{mn} \tag{2.20}$$

Here f, $\vec{k}$, ζ, g, and t are as in Eqn. 2.1. Sea ice of thickness h_i and density ρ_i has a velocity $\vec{v}_i$ which responds to wind stress $\vec{\tau_a}$, ocean current stress $\vec{\tau_o}$, and an internal ice stress represented by the two dimensional stress tensor σ_{mn}.

In Eqn. 2.20 the stress terms are in units of N m^{-2}. From above $\vec{\tau_a}$ is taken as prescribed forcing, while from below $\vec{\tau_o}$ is parameterized as

$$\vec{\tau_o} = \rho_w C_W |\vec{v}_1 - \vec{v}_i| (\vec{v}_1 - \vec{v}_i) \tag{2.21}$$

where $\vec{v}_1$ is the upper ocean layer velocity and the constant coefficient of bulk momentum exchange is given by C_W. Currently no turning angles are employed for the atmosphere and ocean/ice stress terms.

The choice of sea ice rheology σ_{mn} determines the way in which ice flows, cracks, ridges, rafts and deforms. Following Hibler (1979) internal sea ice stress is modeled in analogy to a nonlinear viscous compressible fluid obeying the constitutive law

$$\sigma_{mn} = 2\eta\dot{\epsilon}_{mn} + \left\{(\xi - \eta)(\dot{\epsilon}_{11} + \dot{\epsilon}_{22}) - \frac{P_i}{2}\right\}\delta_{mn} \tag{2.22}$$

where $\dot{\epsilon}_{mn}$ is the strain rate tensor and δ_{mn} $(m, n \in \{1, 2\})$ is the Kronecker delta. The internal sea ice pressure P_i is a function of sea ice thickness h_i and sub grid-scale areal fractional sea ice compactness

$$P_i = P^* h_i e^{-C(1-I)} \tag{2.23}$$

where P^* and C are empirically derived constants.

The pressure is related to the nonlinear bulk ξ and shear η viscosities according to:

$$\xi = \frac{P_i}{2\Delta} \; ; \; \eta = \frac{\xi}{e^2} \tag{2.24}$$

$$\Delta = \left[\left(\dot{\epsilon}_{11}^2 + \dot{\epsilon}_{22}^2 \right) \left(1 + \frac{1}{e^2} \right) + 4 \frac{\dot{\epsilon}_{12}^2}{e^2} + 2 \dot{\epsilon}_{11} \dot{\epsilon}_{22} \left(1 - \frac{1}{e^2} \right) \right]^{\frac{1}{2}} \tag{2.25}$$

Here e is the ratio of the lengths of the principal axes of the yield ellipse (these correspond to the principal components in stress space, i.e. σ_{11} and σ_{22} from Eqn. 2.22).

The yield ellipse discriminates between linear-viscous (internal) and plastic (boundary) points in stress space, while exterior points cannot be reached. Numerical problems arise when the strain rates are small. Then the Δ in Eqn. 2.25 approaches zero, and the viscosities in Eqn. 2.24 approach infinity.

Following Hibler (1979), the problem is avoided by choosing the viscosities to be a maximum of their function value given in Eqn. 2.24, and an empirically chosen maximum value corresponding to the function value when

$\Delta = \Delta_{min} = 2.0 \times 10^{-9} s^{-1}$.

Thermodynamics of sea ice involves the determination of the local growth or melt rate at the base of the sea ice and the local melt rate at the surface. To allow for the prognostic treatment of the sub grid-scale fractional sea ice cover the surface heat balance is solved separately for the ice covered and ice free areas.

That is, the net atmospheric heat flux Q_a is weighted according to the open water heat flux Q_w and heat flux over sea ice (or sea ice and snow) Q_i.

$$Q_a = (1 - I)Q_w + IQ_i \tag{2.26}$$

A thermodynamic equilibrium is sought at the interface between the atmosphere and the sea ice/snow layer. An initial solution T^*_{srf} is found for the sea ice/snow layer surface temperature T_{srf} from the energy balance equation

$$Q_i + Q_{cond} = 0. \tag{2.27}$$

The conductive heat flux Q_{cond} within the sea ice/snow layer is assumed to be directly proportional to the temperature gradient across the sea ice/snow layer and inversely proportional to the thickness of that layer (i.e. the so-called zero-layer formulation of Semtner, 1976).

$$Q_{cond} = k_i \frac{(T_{freeze} - T_{srf})}{\tilde{h}_i} \tag{2.28}$$

Here k_i is the thermal conductivity of sea ice, T_{freeze} the freezing temperature of sea water and $\tilde{h}_i$ the effective thermodynamic sea ice thickness of the sea ice/snow layer. This effective thickness is defined to be

$$\tilde{h}_i = \frac{1}{I}\left(h_i + h_s\frac{k_i}{k_s}\right) \tag{2.29}$$

where h_s is the snow layer thickness and k_s is the thermal conductivity of the snow. The ratio of the thermal conductivity of sea ice with respect to that of snow is approximately 7. This means that snow is seven times more effective as an insulator against oceanic heat loss to the atmosphere than sea ice. Hence, even a relatively thin snow cover will result in a much increased effective sea ice thickness. Atmospheric precipitation is converted to snow fall when T_a is below 0°C. Snow loading on the sea ice may result in the submerging of the sea ice/snow interface. In such cases the thickness of the snow draft is converted to sea ice. Since the heat of fusion of snow is slightly greater than the heat of fusion of sea ice this process results in a net heat gain to the sea ice/snow layer. To close the heat balance of the conversion process a small additional amount of snow is also melted.

When the initial solution T^*_{srf} in Eqn. 2.28 is greater than 0°C the left-hand side of Eqn. 2.27 is recalculated with T_{srf} replaced by 0°C and the resultant energy is used to melt snow and then sea ice from above. In the case where the entire sea ice/snow layer is melted from above any remaining heat flux is added to Q_w in Eqn. 2.26.

To complete the sea ice thermodynamic evolution a heat balance equation must be applied at the ocean/sea ice and ocean/atmosphere interfaces. The balance equation takes the form

$$\rho_w c_w \Delta z_1' \frac{\partial \hat{\theta}_1}{\partial t} = (1 - I)Q_w + I(Q_{cond} - h_i \rho_i L_i) \tag{2.30}$$

and is solved for an interim upper layer oceanic temperature $\hat{\theta}_1$. Here c_w is the specific heat capacity of sea water, L_i is the latent heat of fusion of sea ice and $\Delta z_1'$ is the thickness of the upper ocean layer, given by

$$\Delta z_1' = \Delta z_1 + \zeta - h_{draft} \tag{2.31}$$

where Δz_1 is the defined constant thickness of the ocean model's upper layer. The draft of the sea ice/snow layer h_{draft} is given by

$$h_{draft} = \frac{1}{\rho_w}\left(\rho_i h_i + \rho_s h_s\right). \tag{2.32}$$

where ρ_i and ρ_s are the densities of the sea ice and snow layers respectively. Note that the treatment of a sea ice draft is purely for thermodynamic considerations, and that the ocean momentum balance is not effected. The embedding of sea ice into the upper ocean layer, as opposed to allowing sea ice to exist in multiple ocean layers, is for computational convenience. However, such treatment introduces an upperbound to the sea thickness. In MPI-OM the sea ice draft is not allowed to remain above a local maximum sea ice draft specified as

$$h_{maxdraft} = 0.7(\Delta z_1 + \zeta). \tag{2.33}$$

Any additional sea ice draft is converted to water in a salt (but currently not heat) conserving way. It is noted that this critical sea ice thickness is never reached in the simulation presented here. For the sea ice undersurface to be in thermal equilibrium with the upper ocean it is required that $T_{melt} \leq \theta_1 \leq T_{freeze}$. To maintain this inequality sea ice/snow is melted when the solution for $\hat{\theta}_1$ from Eqn. 2.30 is above T_{melt} and new sea ice is formed when $\hat{\theta}_1$ is below T_{freeze}. For the purposes of this study the effect of salinity on the freezing and melting temperatures is ignored and constant values of T_{freeze} and T_{melt} are used. The model upper layer ocean temperature θ_1 is only allowed to rise above T_{melt} when all of the sea ice/snow layer has been melted within a grid cell. Then the new upper ocean temperature θ_1 and the change in sea ice thickness Δh_i are given by

$$\theta_1 = \hat{\theta}_1 - \min\left\{\frac{h_i \rho_i L_f}{\rho_w c_w \Delta z_1'}, \hat{\theta}_1 - T_{freeze}\right\} \tag{2.34}$$

$$\Delta h_i = \max\left\{(T_{freeze} - \hat{\theta}_1)\frac{\rho_w c_w \Delta z_1'}{\rho_i L_f}, 0\right\}. \tag{2.35}$$

For freezing conditions, the upper ocean temperature and the sea ice thickness change are

$$\theta_1 = T_{freeze} \tag{2.36}$$

$$\Delta h_i = \frac{\hat{\theta}_1 - T_{freeze}}{\rho_i L_f}\rho_w c_w \Delta z_1'. \tag{2.37}$$

Sub grid-scale thermodynamic processes of sea ice growth and melt are assumed to effect the sea ice compactness within a grid cell in the following ways. When freezing occurs over open water areas the sea ice compactness increases (i.e. leads concentration decreases) at a rate given by

$$\Delta I^{thin} = \max\left\{\frac{\Delta h_i^{thin}(1 - I)}{h_o \Delta t}, 0\right\} \tag{2.38}$$

where Δt is the model time step, $\Delta h_i^{thin} = \Delta t Q_w/(\rho_i L_f)$ is the thickness of new sea ice formed and h_o is an arbitrary demarcation thickness (taken to be 0.5 m following Hibler, 1979). When melting of thick sea ice occurs the sea ice compactness decreases (i.e. leads concentration increases) at a rate given by

$$\Delta I^{thick} = \min\left\{\frac{\Delta h_i^{thick} I}{2h_i \Delta t}, 0\right\} \tag{2.39}$$

where Δh_i^{thick} is the change in sea ice thickness due to the melting. This formulation is based on the assumption that sea ice thickness within a grid cell has a uniform distribution between 0 and $2h_i$. The change in compactness of sea ice due to thermodynamic lead opening and closing is then calculated as the sum of both these terms.

$$\frac{\partial I}{\partial t} = \Delta I^{thin} + \Delta I^{thick} \tag{2.40}$$

Completion of the sea ice thermohaline coupling to the ocean model requires consideration of salt and fresh water exchanges during sea ice growth and melt. Sea ice is assumed to have a constant salinity independent of it's age and denoted by S_{ice}. While multi-year Arctic sea ice has a salinity of around 3 psu, thinner ice in both hemispheres has a much higher salinity (Cox and Weeks, 1974; Eicken, 1992). For the simulations presented here an intermediate value of 5 psu representing this global diversity has been chosen. The ocean model's upper layer salinity S_1 is changed by an amount ΔS due to the surface fresh water flux (modified by snow fall which accumulates on top of the sea ice) and due to sea ice growth or melt, according to:

$$\left(S_1 + \Delta S\right)\Delta z'^{old} + \frac{\rho_i h_i^{old}}{\rho_w} S_{ice} = S_1 \Delta z'^{new} + \frac{\rho_i h_i^{new}}{\rho_w} S_{ice} \tag{2.41}$$

Here $\Delta z'^{old}$ is the upper ocean layer thickness accounting for sea surface elevation and sea ice draft as in Eqn. 2.31, and also for the atmospheric precipitation minus evaporation. $\Delta z'^{new}$ is $\Delta z'^{old}$ modified by the new sea ice draft due to melt or growth, and $h_i^{new} - h_i^{old}$ is the amount of sea ice growth (if positive) or melt (if negative).

3. EXPERIMENTAL DESIGN

3.1 Introduction

This section gives an overview on the model setup, i.e. the resolution, the forcing data sets and the applied bulk formulae, as well as the integration procedure and the sensitivity experiments.

3.2 Model Grid

The model setup used in this study is global, but coarser resolution than in Marsland *et al.* (2003) is employed here. It maintains, however, high resolution in the Arctic and the high latitude sinking regions. This was achieved by shifting the North Pole of a formal 3°grid to Greenland. The horizontal resolution gradually varies between a minimum of 20 km in the Arctic and a maximum of about 350 km in the Tropics (Fig. 3.2). The model has 40 vertical levels with increasing level thickness. 20 of them are located in the upper 600 m. The models bathymetry was created by interpolation of the ETOPO-5 dataset (Data Announcement 88-MGG-02, Digital relief of the Surface of the Earth. NOAA, National Geophysical Data Center, Boulder, Colorado, 1988) to the model grid.

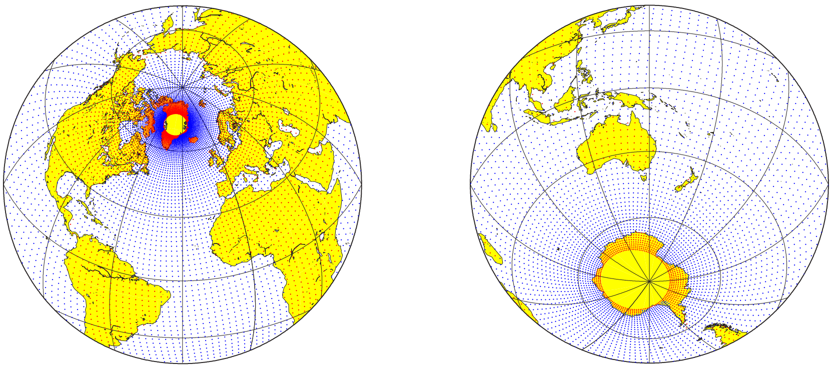

Fig. 3.1: *Curvilinear orthogonal grid of the coarse resolution global version of MPI-OM used in this study.*

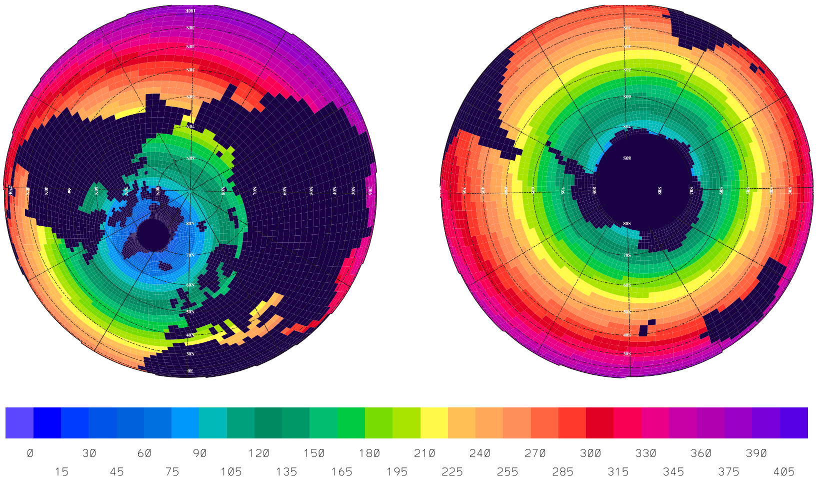

Fig. 3.2: *Resolution of the model used in this study. Units are [km].*

3.3 Bulk Formulae

Simulation with the ocean model requires the specification of heat, fresh water and momentum fluxes at the air/sea interface. Introducing Q_{srf} to denote either Q_w or Q_i in Eqn 2.26 the surface heat balance is given by

$$Q_{srf} = Q^{se}_{srf} + Q^{la}_{srf} + Q^{lw}_{srf} + Q^{sw}_{srf} \tag{3.1}$$

where Q^{se}_{srf}, Q^{la}_{srf}, Q^{lw}_{srf} and Q^{sw}_{srf} are parameterizations of the sensible, latent, long and short wave heat fluxes, respectively.

Following Oberhuber (1993) the turbulent fluxes are parameterized as

$$Q^{se}_{srf} = \rho_a c_a C_H V_{10m}(T_a - T_{srf}) \tag{3.2}$$

$$Q^{la}_{srf} = \rho_a L_{srf} C_L V_{10m}(q_a - q_{srf}) \tag{3.3}$$

Constants ρ_a, c_a and L_{srf} denote the air density, the air specific heat capacity and the latent heat of vaporization or sublimation as appropriate. The 10 m wind speed V_{10m} and 2 m air temperature T_a are taken as prescribed forcing. Variable coefficients of sensible C_H and latent C_L heat transfer are formulated according to Large and Pond (1982). The surface temperature T_{srf} represents either the ocean model upper layer temperature or the sea ice/snow layer skin temperature as in Eqn 2.28. The specific humidity q is a function of water vapor pressure e (units of Pascal) and air pressure p (in this study approximated by a constant 1000 hPa).

$$q = (0.623e)/(p - 0.378e) \tag{3.4}$$

At the 2 m level (q_a) the water vapor pressure is a function of dew point temperature, while at the surface (q_{srf}) the saturation vapor pressure is a function of the water or ice/snow surface temperature. In both cases the vapor pressures (e) are calculated according to the formulae of Buck (1981).

The radiant fluxes are parameterized as

$$Q^{lw}_{srf} = \varepsilon\sigma T_a^4(.39 - .05\sqrt{e/100})(1 - \chi n^2) + 4\varepsilon\sigma T_a^3(T_{srf} - T_a) \quad (3.5)$$

$$Q^{sw}_{srf} = (1 - \alpha_{srf})Q^{incsw} \quad (3.6)$$

The parameterization of net longwave radiation is based on that of Berliand and Berliand (1952), with the fractional cloud cover n taken as prescribed forcing. The surface thermal emissivity and Stefan-Boltzmann constant are denoted by ε and σ respectively. The saturation vapor pressures e depend on water or sea ice/snow conditions and are also calculated according to the formulae of Buck (1981). The cloudiness factor χ is a modified form of that proposed by Budyko (1974) and is a function of latitude ϕ.

$$\chi = 0.5 + 0.4(\min(|\phi|, 60^\circ))/90^\circ \quad (3.7)$$

The incident shortwave radiation Q^{incsw} is provided as part of the forcing data and implicitly modified by cloud cover. The surface reflectivity α_{srf} in Eqn 3.6 is either that appropriate for open water or takes one of four possible values determined by both the absence or presence of snow and by whether the surface temperature of the sea ice or snow is below 0°C (freezing) or equal to 0°C (melting).

$$\alpha_{srf} = \begin{cases} \alpha_w & \text{open water} \\ \alpha_{im} & \text{sea ice surface and melting} \\ \alpha_{if} & \text{sea ice surface and freezing} \\ \alpha_{sm} & \text{snow surface and melting} \\ \alpha_{sf} & \text{snow surface and freezing} \end{cases} \quad (3.8)$$

Over open water Q^{sw}_w is allowed to penetrate beyond the upper model layer with an exponential decay profile.

The surface fresh water forcing effect on sea level displacement is given by

$$Q_\zeta = P - E + R + G \quad (3.9)$$

where P, E, R and G are fluxes of fresh water in units of m s^{-1} due to precipitation, evaporation, river runoff and glacial meltwater, respectively. For the ocean only simulations considered here P is taken as prescribed forcing, R is taken from the observed mean monthly discharge of the world's 50 largest rivers (Dümenil *et al.*, 1993), and G is neglected. Finally, E is calculated from the latent heat flux (Eqn 3.3) as

$$E = Q^{la}_{srf}/(L_{srf}\rho_w) \quad (3.10)$$

where ρ_w is the density of sea water and L_{srf} is once again the latent heat of vaporization or sublimation as appropriate for water or ice/snow surfaces respectively. The corresponding change in surface model layer salinity ΔS_1 is given by

$$\Delta S_1 = \left(\frac{\Delta z_1 + Q_\zeta}{\Delta z_1}\right) S_1 + (S_1 - S_{obs})/S_R \quad (3.11)$$

where S_R is a time-linear restoring coefficient (units s^{-1}), and S_{obs} is a prescribed observed annual surface salinity. Salinity restoring for the experiments considered in chapters 4-7 has a timescale (inverse) of 180 days and is only applied in the ice-free part. The salinity restoring helps to correct for an unbalanced globally integrated surface fresh water flux, along with errors in the poorly known forcing fields (P, R, and G). The restoring has the positive effect of reducing long term model drift. However, it does damp model variability. A more thorough discussion of the effects of surface relaxation is given by Killworth *et al.* (2000).

Momentum forcing by atmospheric wind stress over sea ice is applied directly in Eqn. 2.20. For the ocean surface layer velocity $\vec{v_1}$, the wind stress over open water and the ocean-ice stress result in a change of

$$\frac{\partial \vec{v_1}}{\partial t} = \frac{1-I}{\rho_w \Delta z_1}\vec{\tau_a} + \frac{I}{\rho_w \Delta z_1}\vec{\tau_i} \tag{3.12}$$

where the ice to ocean stress is $\vec{\tau_i} = -\vec{\tau_o}$ from Eqn 2.21.

3.4 NCEP/NCAR Atmospheric Forcing

In this study use is made of the NCEP/NCAR reanalysis dataset with daily temporal resolution and atmospheric synoptic scale variability (Kalnay, 1996). Daily 2 m air and dewpoint temperatures, precipitation, cloud cover, downward shortwave radiation, 10 m wind speed and surface wind stress are used for the full period that is covered by the NCEP/NCAR reanalysis (1948-2001). Dew point temperature T_{Dew} is derived from specific humidity q and air pressure p according to Oberhuber (1988).

$$\begin{aligned} e &= q * p/(0.378 * q + 0.623) && (3.13) \\ \alpha &= 1/7.5 * (log_{10} * e/611) && (3.14) \\ T_{Dew} &= (273.16 - (35.86 * \alpha))/(1-\alpha) && (3.15) \end{aligned}$$

On global average NCEP/NCAR downward short wave radiation is appr. 10% higher than ECMWF reanalysis data and 20% higher than ERBE estimates. To correct for this systematic error in the NCEP/NCAR downward shortwave radiation a global scaling factor of 0.89 is applied.

3.5 Initialization and Spin-Up

The model is initialized with annual mean temperature and salinity data from Levitus *et al.* (1998) climatology and the ocean velocities at rest. It is integrated for one year using daily NCEP/NCAR data for 1948 forcing and a global three dimensional restoring of temperature and salinity to the Levitus climatology. The subsurface restoring is applied everywhere below 40 m with a time constant chosen to be 1 month during this first year. This procedure brings the models velocities and sea ice distribution to near equilibrium with the Levitus climatology. After this initialization procedure the subsurface restoring is switched off. The surface salinity relaxation within the upper model level (0-12 m) is released to a time constant of 180 days.

After this initialization the model is integrated eleven times trough the period 1948-2001. The second and all subsequent cycles use the conditions at the end of the previous run as new initial condition. The total lengths of the integration including the initial spin-up is 595 years (Tab. 3.1). The simulated ocean mean state, in particular the strength of the Atlantic Meridional Overturning Circulation initially drifts. However, it stabilizes during the second NCEP/NCAR cycle. The first two cycles are neglected in the following analysis to account for the models adjustment towards the NCEP/NCAR climatology. Note, that deep ocean properties continue to drift slightly during the full integration period. Results are presented by the ensemble mean of the nine remaining runs.

Year	Procedure	Forcing	Relaxation	Time Const.
0	Initialization	Levitus (1998)		
0-1	Spin-Up	NCEP (48)	T,S (3-D)	30 days
1-54	EXPERIMENT	NCEP (48-01)	S (2-D)	180 days
54-108	EXPERIMENT	NCEP (48-01)	S (2-D)	180 days
108-162	EXPERIMENT	NCEP (48-01)	S (2-D)	180 days
162-216	EXPERIMENT	NCEP (48-01)	S (2-D)	180 days
162-216	SENSITIVITY	HPF ALL	S (2-D)	180 days
162-216	SENSITIVITY	HPF Q+FW	S (2-D)	180 days
162-216	SENSITIVITY	HPF TAU	S (2-D)	180 days
216-270	EXPERIMENT	NCEP (48-01)	S (2-D)	180 days
270-324	EXPERIMENT	NCEP (48-01)	S (2-D)	180 days
324-378	EXPERIMENT	NCEP (48-01)	S (2-D)	180 days
378-432	EXPERIMENT	NCEP (48-01)	S (2-D)	180 days
432-486	EXPERIMENT	NCEP (48-01)	S (2-D)	180 days
486-540	EXPERIMENT	NCEP (48-01)	S (2-D)	180 days
540-594	EXPERIMENT	NCEP (48-01)	S (2-D)	180 days

Tab. 3.1: *Initialization, spin-up procedure and experiments.*

3.6 NCEP Hindcast Ensemble

Performing a hindcast simulation is usually a combined initial condition / boundary value problem. While the surface boundary conditions can be taken from atmospheric reanalysis data, there exists almost no knowledge about the ocean initial conditions of the past. Due to this uncertainty the experiments where carried out in ensemble mode with different initial conditions. The individual ensemble members are calculated subsequently and use the end to the previous run as initial condition. Certain properties like the strength of the Atlantic MOC show some dependence to the initial conditions, while other properties like sea ice thickness agree almost perfectly in between the individual realizations (Fig. 3.3).

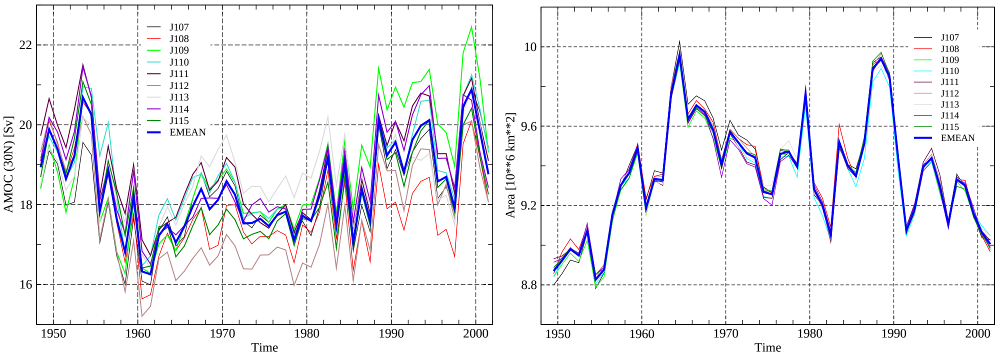

Fig. 3.3: *Left panel shows Atlantic Meridional Overturning Circulation at 30°N and right panel shows annual mean Northern Hemisphere sea ice covered area. Shown are individual ensemble members (thin lines) and the ensemble mean (thick line). Units are [Sv] and* $[10^6 km^2]$*, respectively.*

3.7 Sensitivity Experiments

In order to assess the influence of low-frequency atmospheric variability, three additional sensitivity studies with high pass filtered forcing field are compared to the control integration. The high pass filter removes the low-frequency component (variability longer one month) from certain forcing fields but maintains the high-frequency variability and a climatological seasonal cycle. The following experiments where conducted: (1) all forcing field high-pass filtered (HPF ALL), (2) only wind stress high-pass filtered (HPF TAU), and (3) all forcing field except wind stress high-pass filtered (HPF Q+FW). Note, that fresh water and thermal forcing are linked due to the interactive calculation of evaporation and latent heat flux in the bulk formulae. Therefore they are not considered individually in the sensitivity experiments. An example of the damping by the hp-filter is shown in

Fig. 3.4. The figure shows a spectrum of 2 m air temperature at a single grid point in the central North Atlantic with and without the hp-filter applied. Variability on frequencies below $0.5 Month^{-1}$ is damped, but the climatological seasonal cycle is maintained.

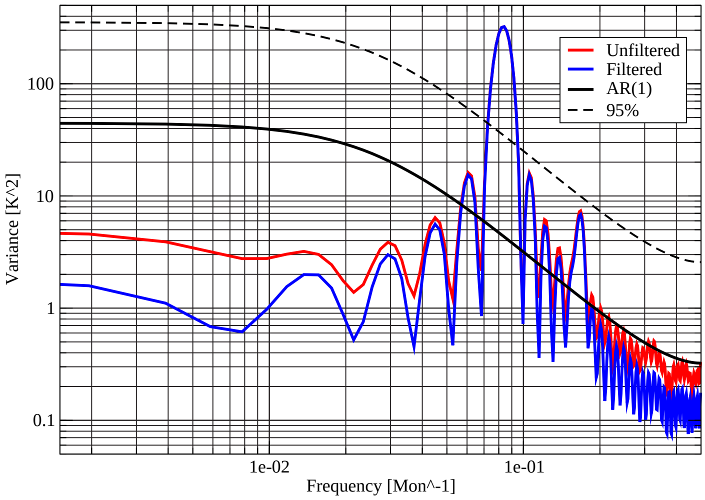

Fig. 3.4: *Example of the damping of the hp-filter used in the sensitivity studies for an arbitrarily chosen 2 m air temperature grid point in the central North Atlantic.*

3.8 Coupled Experiments

Additionally to the uncoupled ocean experiments some results originate from a 500 year control integration (for present day conditions) of the coupled model MPI-OM/ECHAM5. The coupled model consists of the latest cycle of the atmosphere model ECHAM (ECmwf HAMburg) and the ocean model MPI-OM. The atmosphere model is applied at a spectral T42 (2.8°) resolution and 19 vertical layers. The ocean model setup is the same as described in Marsland *et al.* (2003). Both models are coupled using the OASIS coupling software (Terray *et al.*, 1998). Once per day the fluxes of momentum, heat and fresh water are transfered from the atmosphere to the OASIS coupler, where the interpolation onto the ocean model grid is performed, and are then passed to the ocean. In exchange SST, sea ice thickness, sea ice concentration and snow thickness fields are passed via OASIS to the atmosphere. River runoff and a simplified glacier calving scheme are treated interactively as part of the atmosphere model and are passed with the fresh water flux to the ocean. No flux corrections is applied. Results from the same experiment are presented in Latif *et al.* (2004) and Jungclaus *et al.* (2004).

4. RESULTS: SIMULATED MEAN STATE

4.1 Introduction

The following chapter describes the simulated mean state of the ocean and sea ice model and compares it to observations or other models. Deficiencies in the simulation are shown and discussed. The simulated mean state is presented in terms of the ensemble mean from the cycles 3 to 11 of the integrations, averaged over the period 1948-2001. The focus is on the North Atlantic/Arctic region.

4.2 General Circulation

The mean vertically integrated barotropic stream function is shown in Fig. 4.1. The model simulates a volume transport of 44 Sv in the western part of the North Atlantic Subtropical Gyre, associated with the Gulf Stream/North Atlantic Current (NAC). The North Atlantic Subpolar Gyre has a strength of -31 Sv, the South Atlantic Subtropical Gyre -82 Sv. These numbers represent the depth integrated flow (including inverse flowing deep and bottom waters) and therefore do not represent solely the wind driven circulation in the upper ocean. A direct comparison of the vertically integrated mass transport against observations is not possible. However, simulated transports compare reasonably with previous results from other models, e.g. Legutke and Maier-Reimer (1999); Gent *et al.* (1997); Furevik *et al.* (2002). Simulated mass flux through the Drake Passage is approximately 210 Sv, while the observational estimate is $134 \pm 14 Sv$ (Nowlin and Klinck, 1986). The strong overestimation by almost 60% is probably related to excessive wintertime deep convection in the Weddell Sea. Simulated Bering Strait transport is approximately 0.5 Sv and therefore 40% weaker than the observational estimate of $0.83 \pm 0.1 Sv$ (Roach *et al.*, 1995). The northward inflow of warm Indian ocean water associated with the Agulhas leakage is approximately 17 Sv and therefore somewhat larger than observational estimates of 2 - 15 Sv (de Ruijter *et al.*, 1999). Transports for key locations are summerised in Tab. 4.1.

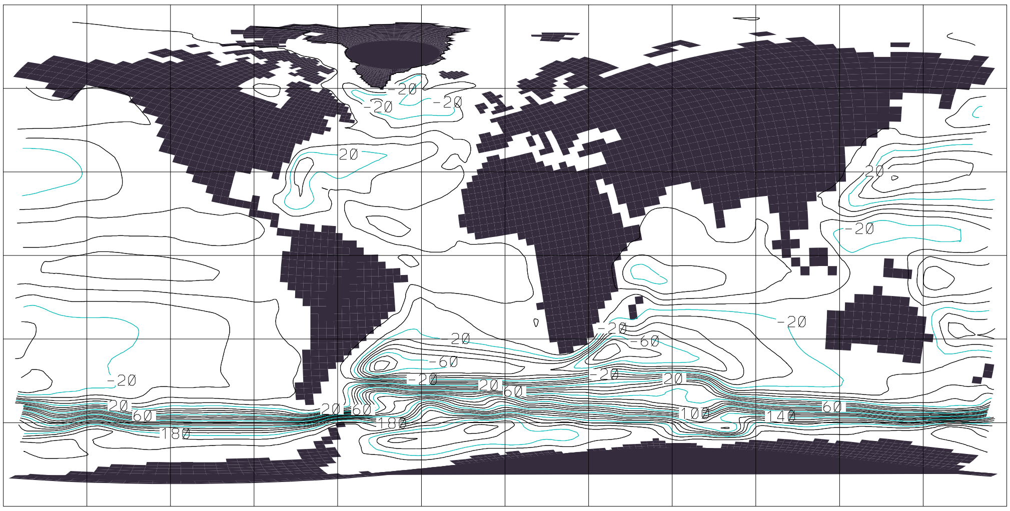

Fig. 4.1: *Ensemble mean barotropic stream function averaged for the period 1948-2001. Contour interval is 10 Sv.*

Current/Location	Transport	Unit
N. Atl. Subtropical Gyre	44.3 ± 2.4	Sv
N. Atl. Subpolar Gyre	-31.0 ± 2.5	Sv
S. Atl. Subtropical Gyre	-82.7 ± 4.8	Sv
N. Pac. Subtropical Gyre	61.7 ± 3.0	Sv
Drake Passage	210.2 ± 7.0	Sv
Bering Strait	0.46 ± 0.05	Sv
Banda Strait	13.2 ± 2.9	Sv
Agulhas leakage	16.9 ± 5.2	Sv
Max. Atl. Overturning (NADW)	20.3 ± 1.0	Sv
Min. Atl. Overturning (AABW)	-5.7 ± 0.6	Sv
S. Atl. Subtropical Convergence (SACW)	-9.9 ± 1.3	Sv
Outflow of NADW at 30°S	16.2 ± 0.9	Sv

Tab. 4.1: *Volume transports in key locations as ensemble mean and standard deviation with respect to annual values for the period 1948-2001.*

4.3 Deep Water Formation

Simulated mixed layer depth for late winter (March) and late summer (September) are shown in Fig. 4.2. Here mixed layer depth is diagnosed as depths, where the density criteria $\sum_1^k \delta\rho_{insitu}(z) < 0.125$ is fulfilled. The ocean model realisticly simulates the two main sinking sites in the northern North Atlantic. In the central Labrador Sea the March mixed layer depth reaches 2300 m ± 800 m, while in the central Greenland Sea it is 1100 m ± 1000 m. Note, that these values represent long term averages.

Deep convection does not occur in every winter. Secondly, GS convection is not always shallower than LS convection. Individual convection events in the GS exceed 3500 m in the simulation. Longterm averaged convection in the Irminger Sea is rather shallow, with wintertime mixed layer depth of appr. 500 m. However, during few years Irminger Sea convection can penetrate down to 1200 m, preferablely during years with lower than normal Fram Strait sea ice export, and thus weaker stratification south east of Greenland. Bacon *et al.* (2003) show that Irminger Sea convection to appr. 1000 m depth occured in winter 1996/97. Pickart *et al.* (2003) point to the local atmospheric conditions, in particular the Greenland Tip Jet, as main forcing agent. However our simulation indicate also a strong connection to the upper ocean salinity in the East Greenland Current. Mixing to intermediate depths in the Irminger Sea may contribute to the preconditioning of Labrador Sea convection by bringing more haline water to the surface. Spurious convection to intermediate depths occurs in the Baffin Bay domain. Presence of convection in this location depends strongly on the representation of Canadian Archipelago through-flow, in particular on the representation of Lancaster Sound and Narres Strait. In the applied model setup Lancaster Sound is open while Narres Strait is closed. A sensitivity study with an open Narres Strait does not show convection in the Baffin Bay area due to the additional fresh water input through this relative shallow passage. However, large scale variability seems not affected.

In the Southern Hemisphere the main convective regions are the Weddell and the Ross Sea. Bottom water formation takes place predominantly in coastal polynyas and areas of sea ice divergence along the Antarctic shelf. Also open ocean convection to abyssal depth has been observed in the Weddell Sea (Gordon, 1978), though observations are limited in time and space. The simulated Weddell Sea convection reaches down to depths below 4000 m almost every winter. Consequently, the major part of bottom water is formed by open ocean convection in the simulation. A reason might be that the ocean models rather coarse horizontal resolution of about 100 km around Antarctica. The resolution does not allow a proper simulation of convection on the continental shelfs. A surface manifestation of the Weddell Sea open ocean convection is the occurance of a polynya around 65°S and 20°W to 40°E. The Weddell polynya was observed in mid 1974, 1975 and 1976 (Martinson *et al.*, 1981). In the simulation an area with reduced sea ice concentration is present in almost every winter in the position of the observed Weddell Sea polynya. In general the persistent presence of the Weddell Sea polynya is quite sensitive to the surface fresh water flux, therefore the inclusion of a glacial melt scheme for the Antarctic would help in its removal by adding stability to the water column (Marsland and Wolff, 2001). Furthermore, details of the experimental setup, e.g. the time constant of sea surface salinity relaxation, the choice of the climatological sea surface salinity data set or the treatment of salinity relaxation in the vicinity of sea ice have a large impact.

Mixed Layer Depth Year 48-01 (m)

a) March b) September

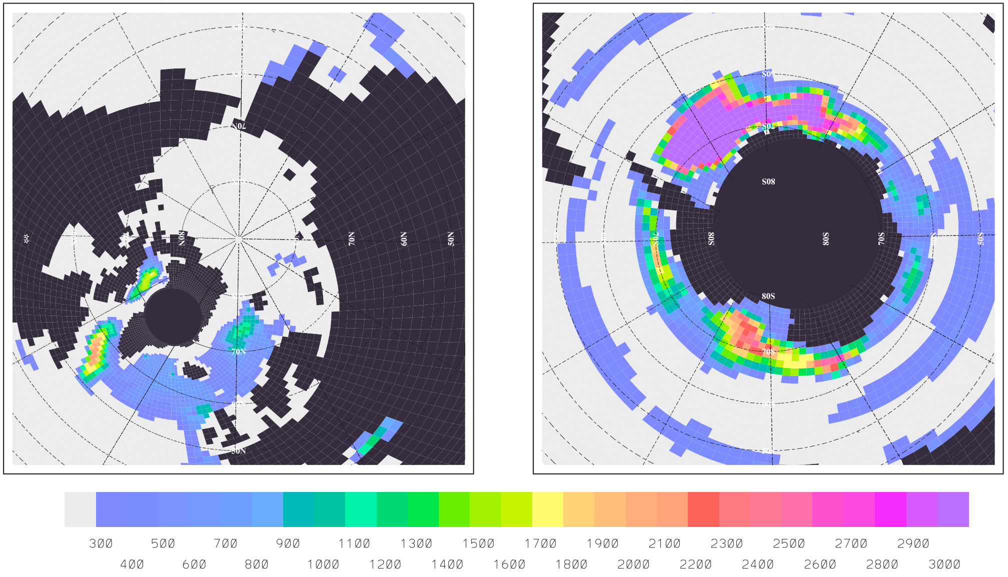

c) March d) September

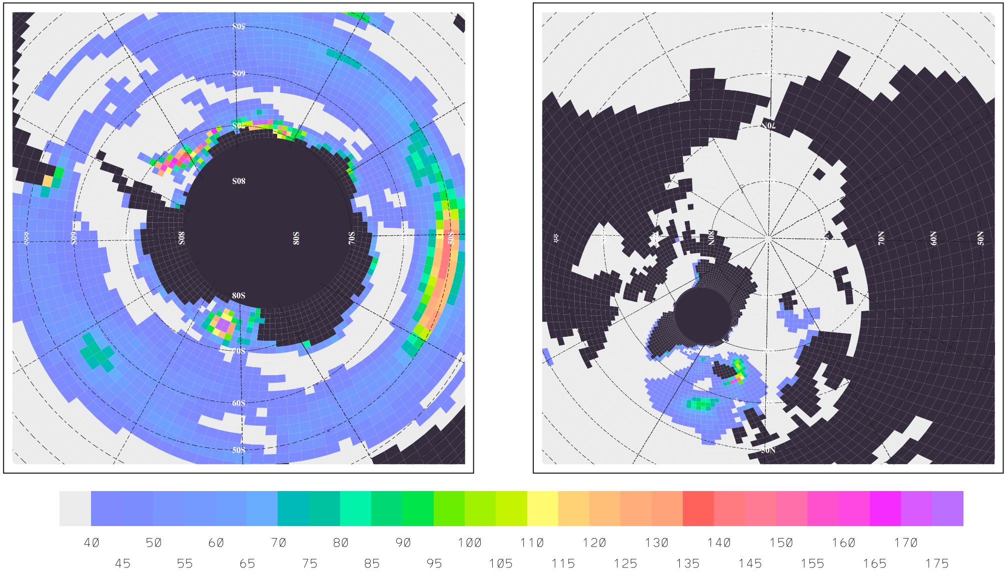

Fig. 4.2: *Simulated mixed layer thickness [m] for March and September. Contour interval is 200 m.*

4.4 Thermohaline Circulation

Global and Atlantic meridional overturning stream functions are shown in Fig. 4.3. The model simulates the typical two cell structure associated with the MOC. The upper overturning cell has a global maximum of 20 Sv at 40°N at a depth of about 1000 m. This maximum is associated with the production and spreading of NADW. The overturning strength at 24°N is 17 Sv and compares well to the observational estimates of 17-18 Sv by Hall and Byrden (1982) and Roemmich and Wunsch (1985). The outflow from the Atlantic into the Southern Ocean at 30°S is approximately 16 Sv at about 1200 m depth. The upper overturning cell has an average thickness of approximately 3200 m in the Atlantic. The lower overturning cell has maxima of 18 Sv and 6 Sv at the equator, Global and Atlantic respectively. This lower cell is associated with the production and spreading of AABW formed around Antarctica. The observational estimate for the amount of AABW crossing the equator in the Atlantic is 4.3 Sv (McCartney and Curry, 1993). The inflow of AABW to the Atlantic at 30°S is approximately 5 Sv at 4000 m depth. The corresponding observational estimates by Speer and Zenk (1993) are 6-7 Sv. The meridional overturning stream function shows the subtropical convergence cells (STC) associated with the formation of Central Water (CW) due to subduction along the subtropical convergence zones and uppwelling in the equatorial current system. The South Atlantic STC strength is appr. 10 Sv in the simulation and in estimates by Zhang *et al.* (2003). Volume transports for key properties are summarized in Tab. 4.1.

Global and Atlantic long term averaged poleward transports of heat implied by the net surface atmosphere-ocean heat flux are shown in Fig. 4.4. The simulation compares reasonably well with observational estimates from inverse methods (Rintoul and Wunsch, 1991; Macdonald and Wunsch, 1996b; Johns *et al.*, 1997) and the estimates for 1988 from the Earth Radiation Budget experiment (ERBE) (Trenberth and Solomon, 1994). On the Northern Hemisphere the simulated poleward heat transport has a maximum of appr. 1.8 PW at 20°N, while in the Atlantic the simulated heat transport is appr. 1.1 PW at 25°N.

In addition to the traditional diagnostic of the MOC by a depth-latitude coordinate stream function Fig. 4.5 shows the three dimensional structure of the MOC diagnosed in σ_2 density classes. A similar diagnostic has been proposed by Bleck and Sun (2004). Horizontal transports are sampled into density classes, here $\sigma_2 < 36.8$, $36.8 < \sigma_2 < 37.05$ and $\sigma_2 > 37.05$. These density classes are chosen to represent the upper and intermediate, deep and bottom water masses in the Atlantic. Diapycnal fluxes between these layers where calculated by integrating the divergence of the isopycnal transports from the bottom to the respective layer.

Combining the five maps in Fig. 4.5 yield a quantitative picture of the modeled three-dimensional circulation. Dominant features of the isopycnal transports in the upper and intermediate density range are the warm-water path of the MOC, e.g. in Subtropical and Subpolar Gyres as well as the Agulhas leakage. The prominent feature in the deep density class is the Deep Western Boundary Current fed by the entrainment of the overflows into

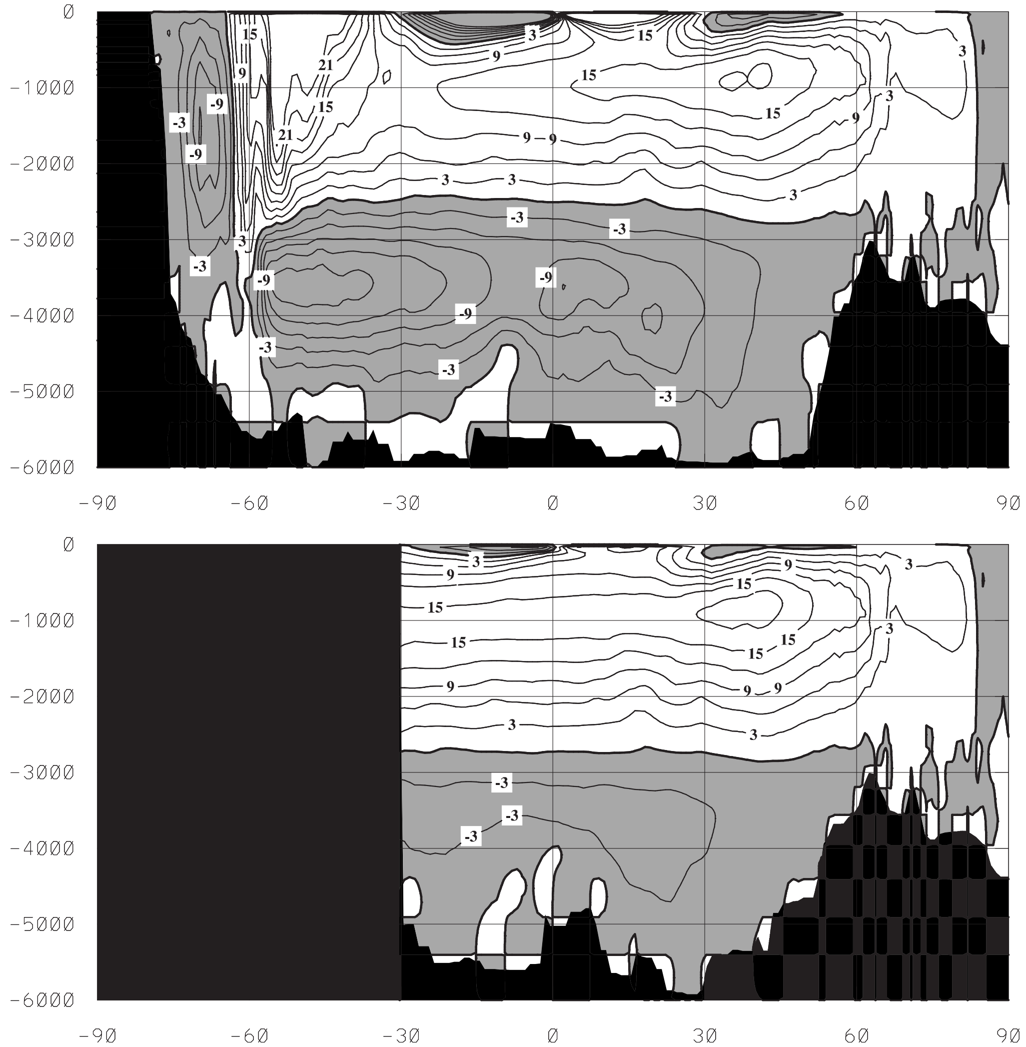

Fig. 4.3: *Global (upper panel) and Atlantic (lower panel) meridional overturning stream function averaged over the last integration cycle (1948-2001). Contour interval is 3 Sv, negative values are shaded. Left axes show depths and lower axes show latitude.*

the ambient North Atlantic deep water as well as the spreading of LSW. The diapycnal fluxes between the upper and deep layer reveal downward fluxes of appr. 8 Sv in the LS and appr. 2-3 Sv entrainment by both overflows respectively. Downward flux in the GIN Seas is appr. 6 Sv. Appr. 3 Sv are detrained from the deep layer upward by vertical mixing along the NAC path. The lower class exhibits the overflows north of the sills of the Greenland-Island-Scottland Ridge and the Antarctic Bottom Water. The diapycnal fluxes between deep and the bottom class reveal upward fluxes of appr. 3 Sv by overflow water feeding from the bottom into the deep layer. The balancing downward flux in the GIN Seas is appr. 7 Sv feeding into both overflows and via a third branch a deep inflow in the Arctic basin.

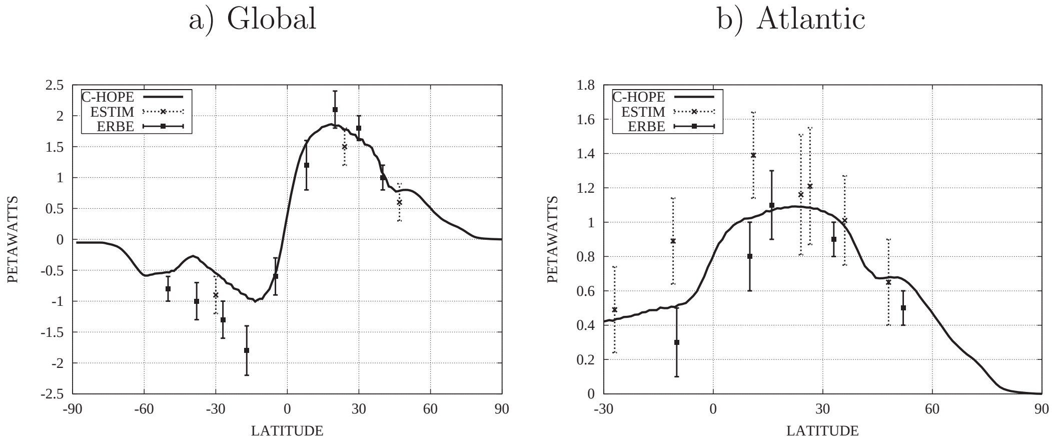

Fig. 4.4: *Meridional heat transport [PW] implied by ocean to atmosphere heat flux for (a) the global Ocean and (b) the Atlantic. Ocean heat transports are averaged over the last integration cycle (1948-2001). Estimates (ESTIM) with error bars are based on in situ observations are taken from Rintoul and Wunsch (1991), Macdonald and Wunsch (1996b) and Johns* et al. *(1997). 1988 estimates are derived from top of the atmosphere as part of the Earth Radiation Budget Experiment (ERBE) using ERA data to remove atmospheric heat transport are taken from Trenberth and Solomon (1994). Left axes show heat transport and lower axes show latitude.*

There is also a inflow from Arctic Ocean contributing to the overflows. In total appr. 16 Sv of deep water ($36.8 < \sigma_2 < 37.05$) are formed by LS convection (8 Sv), both overflows (6 Sv), entrainment (5 Sv) and detrainment (-3 Sv) in the region between 50°N and 60°N.

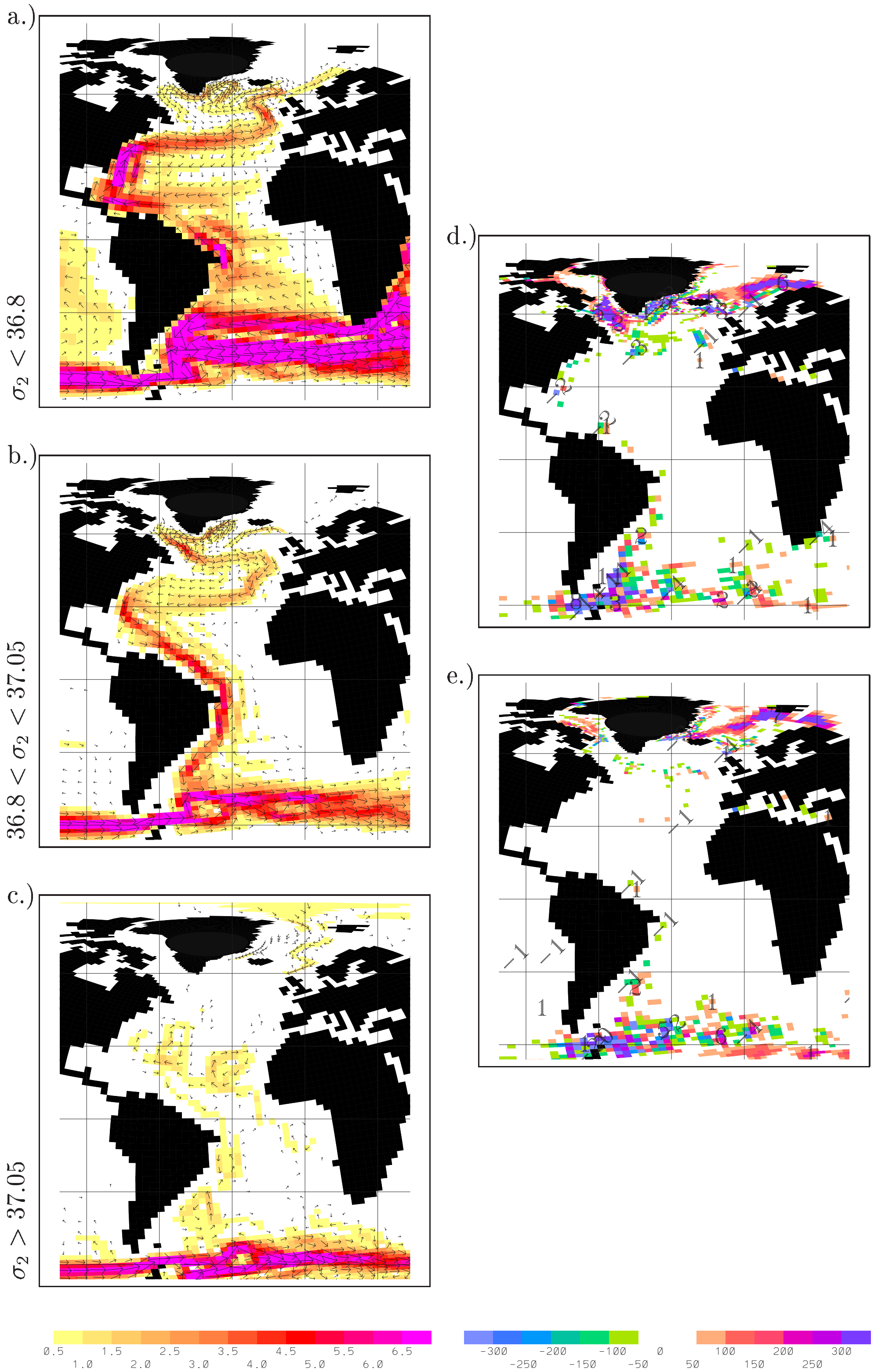

Fig. 4.5: *Ensemble mean iso- and diapycnal mass fluxes in three density layers corresponding to upper and intermediate, deep and bottom waters averaged for the period 1948-2001. Left column (a,b,c) shows local isopycnal fluxes in each layer; every second arrow is plotted. Units are [Sv]. Right column (d,e) shows diapycnal fluxes in between the layers. Colors indicates diapycnal velocities and numbers indicate the associated diapycnal transports (negative = upward). Units are [m/yr] and [Sv], respectively.*

4.5 Water Mass Structure

Fig. 4.6, 4.7 and 4.8 show sections of potential temperature, salinity and potential density with depth through the western Atlantic and Arctic Oceans inspired by a similar GEOSECS section. Also shown are the differences with respect to the initial state (Levitus *et al.*, 1998) of the integration in order to assess the models drift. Three regions with large temperature and salinity drifts are found in the upper 1000 m. Firstly, the position of the Northern Hemisphere subpolar frontal system is shifted southward in the simulation. Too cold temperatures and too low salinities are found around 45°N, due to a mismatch between observed and modeled Gulf Stream path (in particular in the region of the North West Corner). This unsatisfactory result is common to coarse resolution ocean models (Dengg *et al.*, 1996) with a simulated Gulf Stream/NAC path that is often too zonal. Secondly, the simulation poorly resolves the properties of the Antarctic Intermediate Water (AAIW) around 45°S. Simulated AAIW is too salty and too warm. This bias might be a consequence of the too strong ACC/Drake passage transport in the simulation. Third, too little Mediteranien Water reaches the western Atlantic, resulting in too cold and too fresh water mass properties around 30°N at intermediate depth. Furthermore, the abyssal water masses originating in the Southern Ocean are simulated slightly too cool and too fresh, while NADW is slightly too warm and too salty. This results in a slightly overestimated vertical density gradient between the deep and bottom water masses. Finally, intermediate waters in the Greenland Sea are too warm and too salty, probably related to a too deep inflow of North Atlantic Water via the North Atlantic Current into the GIN Seas. However, the overall model drift seems to be acceptable, if one considers the overall integration length of almost 600 years.

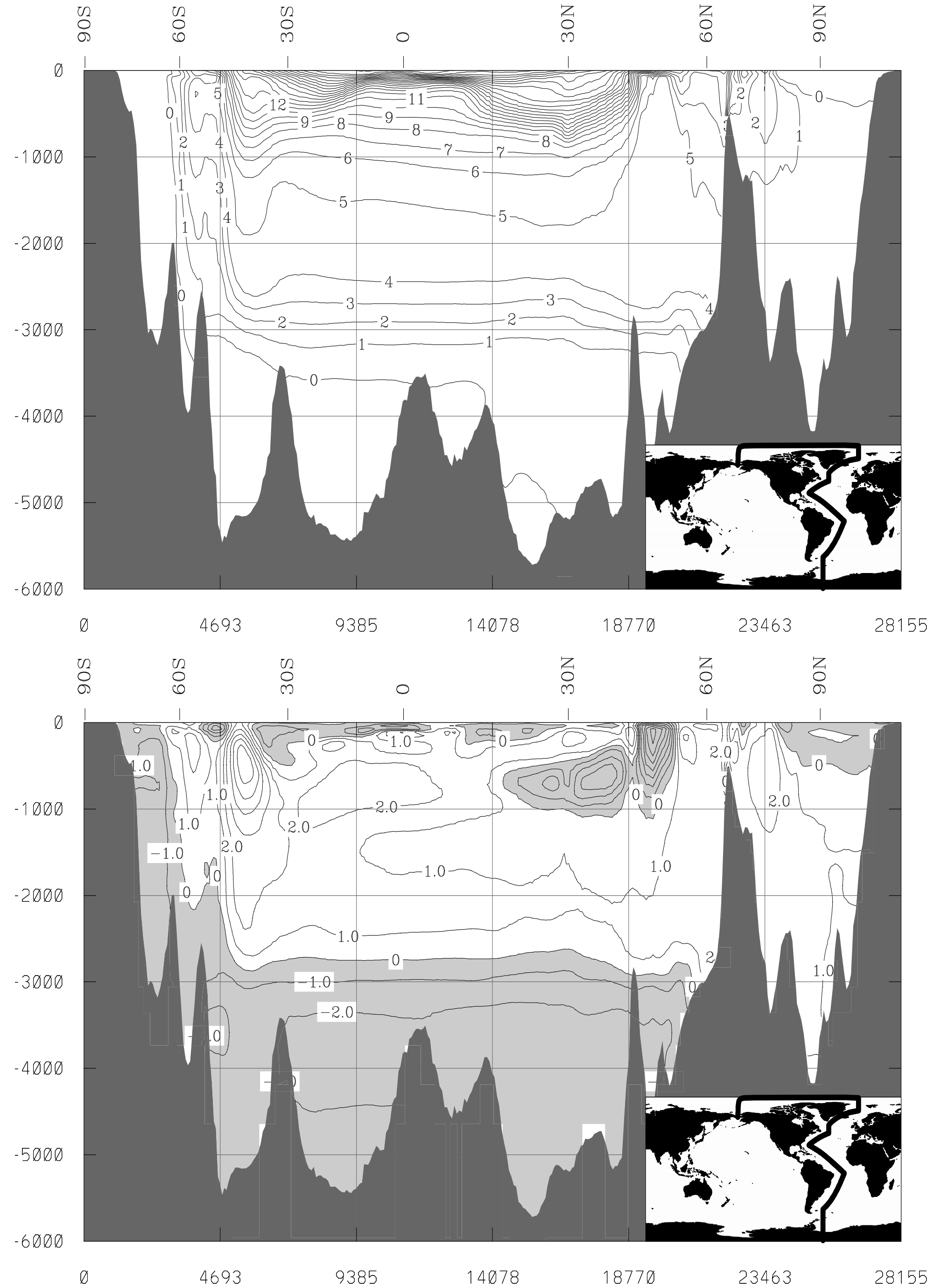

Fig. 4.6: *Potential temperature along a section through the western Atlantic and Arctic ocean. The upper panel shows the time average over the last integration cycle. The lower panel shows the difference with respect to the initial state (Levitus* et al.*, 1998). Latitudes (unequally spaced) are marked on the upper axis of each panel and on-track distance is shown on the lower axis. Depth is shown in units of m on the left axis. The inset shows the geographic location of the section. Contour interval is 1° C and negative values are shaded in the difference plot.*

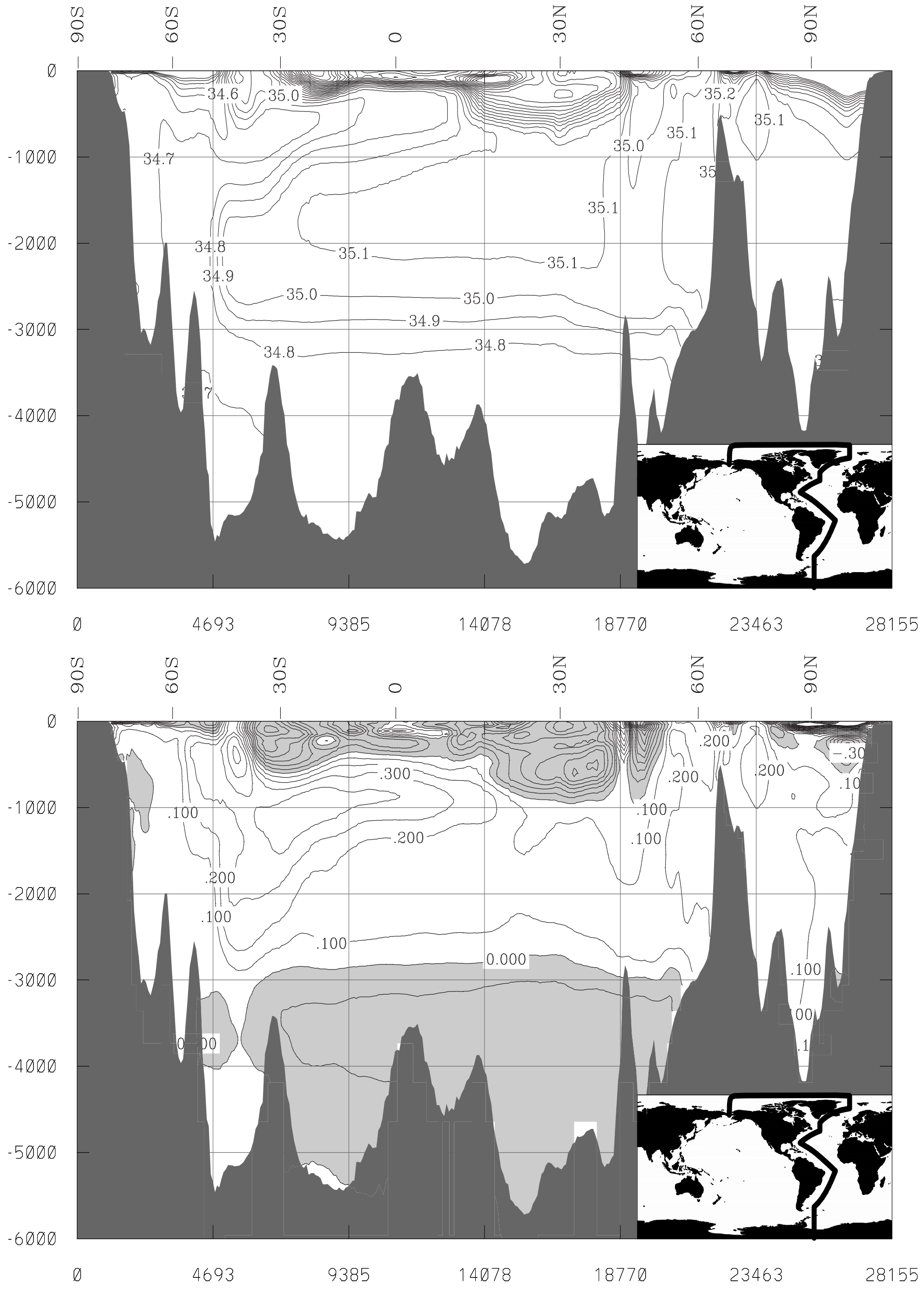

Fig. 4.7: *Salinity along a section through the western Atlantic and Arctic ocean. The upper panel shows the time average over the last integration cycle. The lower panel shows the difference with respect to the initial state (Levitus* et al.*, 1998). Latitudes (unequally spaced) are marked on the upper axis of each panel and on-track distance is shown on the lower axis. Depth is shown in units of m on the left axis. The inset shows the geographic location of the section. Contour interval is 0.1 psu and negative values are shaded in the difference plot.*

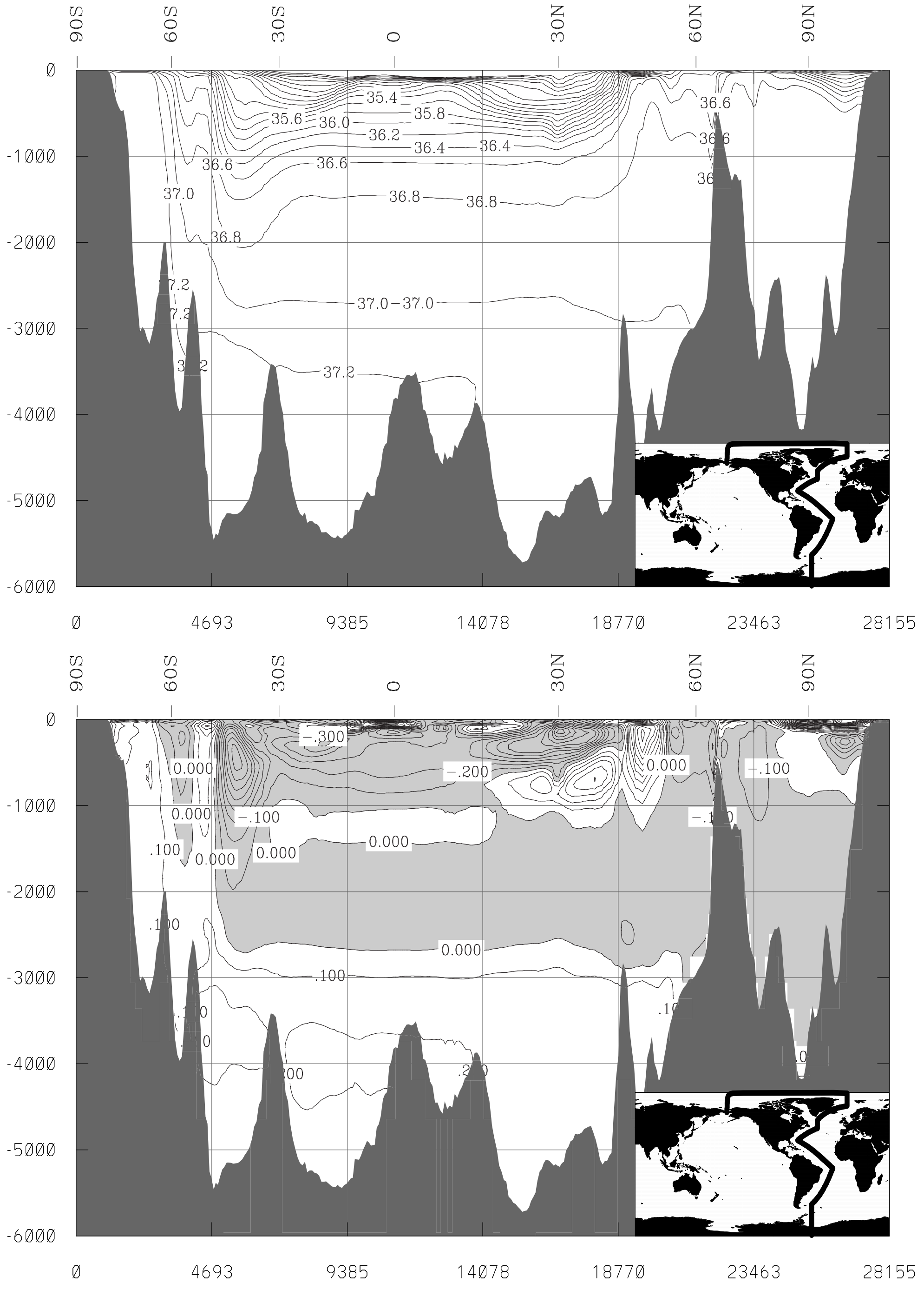

Fig. 4.8: *Potential density (σ_2) along a section through the western Atlantic and Arctic ocean. The upper panel shows the time average over the last integration cycle. The lower panel shows the difference with respect to the initial state (Levitus* et al.*, 1998). Latitudes (unequally spaced) are marked on the upper axis of each panel and on-track distance is shown on the lower axis. Depth is shown in units of m on the left axis. The inset shows the geographic location of the section. Contour interval is 0.1 sigma units and negative values are shaded in the difference plot.*

4.6 Arctic Ocean and Sea Ice

Although the Arctic ocean represents only appr. 1% of the worlds ocean volume, it is an important source of fresh water for the North Atlantic. Precipitation and river runoff into the Arctic ocean exceeds evaporation, letting the region act as a dilution basin for the Atlantic ocean. In this way Arctic properties can influence the stratification and thus the vertical circulation in the North Atlantic sinking regions. Furthermore the region is of special interest since its properties, e.g. summertime sea ice covered area, are expected to be a early indicators of global climate change due to anthropogenic greenhouse gas emissions.

4.6.1 Arctic Sea Ice Area

Satellite based observations of the Arctic sea ice extent exist back into the late 1970th. A comparison of observed mean sea ice extent (Johannessen *et al.*, 2002) between 1978-1998 with the corresponding period of the simulation is shown in Fig. 4.9. The large scale spatial pattern of the Northern Hemisphere sea ice extent is captured by the simulation. Note, that the observed data has a horizontal resolution of appr. 25 km and resolves many small island that are not represented in the model grid. To ensure that the ocean and land areas are the same in both data sets, the observational data was interpolated to the ocean model grid. Furthermore, no observations are available north of 85°N. For the purpose of this analysis 100% ice cover was assumed in both data sets in this region. The seasonal cycle of Northern Hemisphere sea ice extent (excluding the Seas of Okhotsk and Japan) is shown in Fig. 4.10. The simulated maximum value of sea ice extent is $12.8 * 10^6 km^2$ in March. The corresponding observed value is $12.2 * 10^6 km^2$. Simulated March sea ice cover is overestimated in the Baltic Sea and slightly underestimated in the Sea of Okhotsk (see Fig. 4.9). In September minimum values occur in the simulation as well as in the observation. September sea ice extent is $7.9 * 10^6 km^2$ in the simulation and $7.5 * 10^6 km^2$ in the observation. Too low sea ice concentrations are simulated all over the central Arctic, and particularly in the Siberian sector in the late Arctic summer. Ice growth is rather rapid from September to December and decreases afterwards until March. The maximum of melting occurs between July and August. The overall error in the simulated climatological sea ice extent is less than 5% and equally distributed over year. It should be noted, that due to the experimental setup the sea ice covered area is rather strongly constrained by the prescribed surface forcing (e.g. by using the 2 m air temperature).

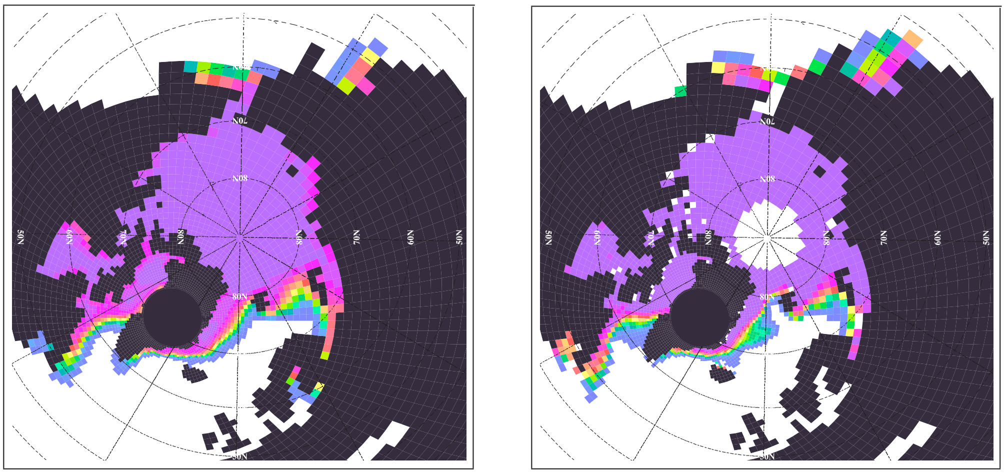

a) Sea Ice Conc. (March)

b) Sea Ice Conc. (March)

c) Sea Ice Conc. (September)

d) Sea Ice Conc. (September)

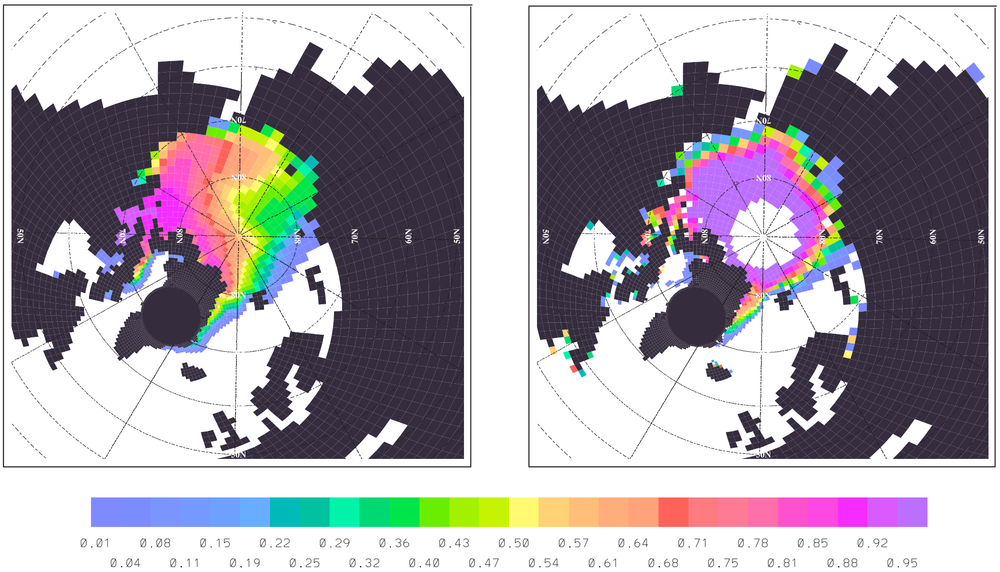

Fig. 4.9: *Simulated (left row) and observed (right row) monthly mean sea ice concentration [ ] for March (a,b) and September (c,d) averaged for the period 1978-1998. The observational data was taken from Johannessen* et al. *(2002); the data were interpolated to the ocean model grid for easy intercomparison. There are no observations available north of 85°N.*

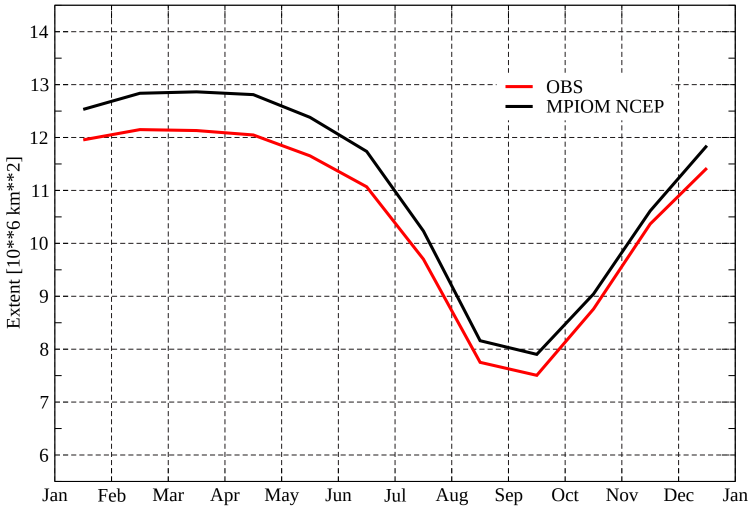

Fig. 4.10: *Northern Hemisphere (excl. Sea of Okhosk) sea ice extent [Mio. km^2] from the the simulation and observations (Johannessen* et al.*, 2002).*

4.6.2 Arctic Sea Ice Thickness

Due to spatial and temporal sampling deficiencies in submarine ice draft data, the distribution of sea ice thickness and the amplitude of its seasonal cycle are relatively poorly known. Observed annual mean sea ice thickness is estimated to be between 2 m and 3.5 m in the deep water portion of the Arctic (Rothrock *et al.*, 1999). However, a large uncertainty in this estimate is the amplitude of the seasonal cycle. Based on a numerical model Rothrock *et al.* (1999) estimates the amplitude to be appr. 1.7 m between March and September. Secondly, the observations indicate the presence of pronounced decadal variability. Therefore the sea ice thickness estimates depend largely on the averaging period. Fig. 4.11 shows simulated climatological mean sea ice thickness [m] for March (a) and September (b) and sea ice drift [cm/s] for March (c) and for September (d) averaged between 1948 and 2001. In general thicker sea ice is found in the Canadian Basin, at the North Pole and in the Nansen Basin north of Greenland, while in the Eastern Arctic, the Chucki Sea and the Beaufort Gyre the mean ice thickness is considerably thinner. The climatological thickness distribution and the seasonal cycle are captured by the model consistently to the few observations.

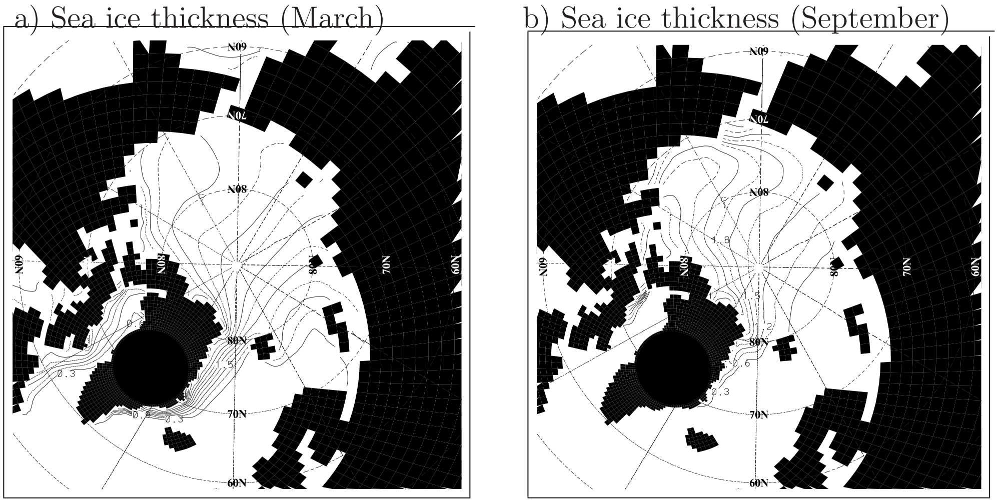

a) Sea ice thickness (March)

b) Sea ice thickness (September)

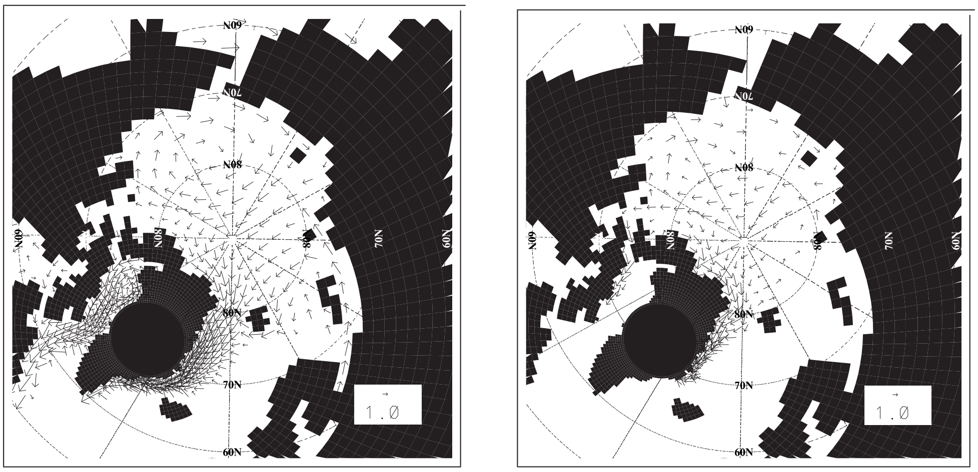

c) Sea ice drift (March)

d) Sea ice drift (Sept)

Fig. 4.11: *Simulated properties of the Arctic sea ice: (a) climatological mean sea ice thickness for March (a) and September (b) and sea ice drift for March (c) and for September (d) averaged between 1948 and 2001. Isoline distance is 30 cm; reference arrow is 1 cm/s. Every other arrow is shown.*

4.6.3 Arctic Sea Ice Drift

Arctic sea ice drift is controlled by wind stress, ocean currents and internal deformation stresses. The main features in the Arctic ice drift pattern are an anti-cyclonic gyre in the Beaufort Basin and the Transpolar Drift Stream from the Laptev Sea to Fram Strait. These features are more pronounced during winter and less pronounced in summer (Proshutinsky *et al.*, 2002). During winter the wind stress and the geostrophic ocean currents coincide in setting a strong anti-cyclonic gyre in the Beaufort Sea, while during summer the ocean geostrophic circulation prevails the weaker wind stresses and may drive the ice eventually against the wind motion. The largest drift velocities of up to 10 cm/s occur east of Greenland during winter, corresponding to the region and season with the largest wind stresses. In the Nansen and the Canadian Basin large ice buildups result in smaller drift velocities due to increased internal deformation stress. The model simulates the mean sea ice drift pattern and its seasonal cycle consistently to previous results, e.g. by Proshutinsky and Johnson (1997); Emery *et al.* (1997); Proshutinsky *et al.* (2002); Hilmer (2001).

4.6.4 Arctic Sea Ice Export

Fresh water is exported from the Arctic into the GIN Seas and the North Atlantic through Fram Strait and the Canadian Archipelago. The fresh water export consists mainly of solid sea ice and snow, but includes a considerable liquid component in the upper ocean currents. The time-mean Fram Strait sea ice export by solid sea ice and snow, and its standard deviation with respect to annual values, amounts to $2874 \pm 674 km^3/yr$. Fram Strait sea ice export in the simulation is consistent with observational estimates of 2790 km^3/yr by Aagaard and Carmack (1989) and $2565 \pm 600 km^3/yr$ for the 1990th by Vinje *et al.* (1998) and Vinje (2001). Uncertainty is appr. 15% for the latter. Drainage of sea ice west of Greenland is largely unkwown. Simulated sea ice exports through the Canadian Archipelago (CAA) via Lancaster Sound ($391 \pm 134 km^3/yr$) as well as the exports from Hudson Bay ($205 \pm 68 km^3/yr$) are both smaller than one standard deviation of the Fram Strait transports.

4.6.5 Arctic Fresh Water Budget

A climatological fresh water budget for the Arctic domain is shown in Tab. 4.2. All transports are calculated with respect to a reference salinity of 34.8, a common value from the literature, e.g.(Aagaard and Carmack, 1989) and close to the models climatological mean of 34.79 for the Arctic domain. The largest source of fresh water in the Arctic are the Siberian and Canadian rivers (appr. $3000km^3/yr$) and the net atmospheric fresh water flux (appr. $1100km^3/yr$). In the simulation there is also an artificial contribution from the surface salinity restoring in ice free regions off appr. $570km^3/yr$. The total surface fresh water input amounts to $4720 \pm 250km^3/yr$. The second largest source with $711 \pm 182km^3/yr$ is the lateral inflow of fresh North Pacific water via Bering Strait. The simulated liquid Bering Strait inflow amounts to $769 \pm 96km^3/yr$, which is appr. 50% smaller than the observational estimate of $1670km^3/yr$ by Aagaard and Carmack (1989). These fresh water sources are balanced by the outflows through Fram Strait ($-3372 \pm 666km^3/yr$) and the Canadian Archipelago ($-502 \pm 162km^3/yr$), as well as the inflow of saline Atlantic Water onto the Barents Shelf ($-1262 \pm 130km^3/yr$). For Fram Strait the simulated liquid fresh water export is $-983 \pm 373km^3/yr$, which is close to the estimate of $980km^3/yr$ by Aagaard and Carmack (1989) or $757km^3/yr$ by Steele *et al.* (1996). The simulated liquid fresh water export via the Canadian Archipelago ($-161 \pm 48km^3/yr$) is considerably smaller than observational estimates of $-920km^3/yr$ by Aagaard and Carmack (1989). As mentioned earlier, the models horizontal resolution does not allow a proper representation of all the minor Canadian Archipelago passages, and so some caution is advised considering the previous result. Finally, the fresh water storage in the Arctic domain shows a small negative drift of appr. $-25km^3/yr$ due to slight increase in upper ocean salinity. Diagnosing the lateral liquid fresh water transports offline involves spatial and temporal averaging, as well as the choice of a reference salinity. Furthermore, the fresh water budget analysis is based on monthly averaged quantities and a simlpyfied advection formulation. Sub grid-scale transports are neglected. These inaccuracies add up to an imbalance in the net fresh water flux of appr. $319km^3/yr$, so some caution is advised regarding the result.

Source	Solid	Liquid	Total	Reference
Atlantic inflow (Barents Shelf)	-159 ± 115	-1103 ± 174	-1262 ± 130	-790 (liquid) A&C89
Pacific inflow (Bering Strait)	-58 ± 112	769 ± 96	711 ± 182	1670 (liquid) A&C89
Canadian Archipelago	-340 ± 127	-161 ± 48	-502 ± 162	-920 (liquid) A&C89
Fram Strait	-2388 ± -530	-983 ± 373	-3372 ± 666	-2790 (solid) -980 (liquid) A&C89
$\delta FW/\delta t$			-25 ± 615	
P-E + Runoff + Restoring			4720 ± 250	4200 (total) A&C89

Tab. 4.2: *Arctic fresh water budget (solid, liquid and total) mean and standard deviation with respect to annual values for the simulation period 1948-2001. Units are [km^3/yr]. For the liquid fresh water fraction a reference salinity of 34.8 was chosen (Aagaard and Carmack, 1989).*

5. RESULTS: SIMULATED VARIABILITY IN THE NORTH ATLANTIC

5.1 Introduction

The water mass transformation of cold and fresh Polar and relative warm and salty North Atlantic Water into North Atlantic Deep Water (NADW) is an essential part of the Atlantic Meridional Overturning Circulation (MOC). Two major processes are contributing to this transformation: first, winter time deep convection due to buoyancy loss at the ocean surface induced by the local atmospheric conditions and secondly, cross frontal mixing of the source waters within the horizontal circulation. Understanding the variability of the Atlantic MOCs strength and the associated northward transport of heat is of particular interest for understanding the European/Arctic climate system (Broecker, 1997). However, currently no direct measurements of the MOC exist and consequently much of the current knowledge is based on models. The following chapter addresses aspects of MOC variability between 1948-2001 from inter-annual to multi decadal times scales by means of forced and coupled simulations with MPI-OM.

5.2 Deep Convection

Simulated wintertime deep convection occurs in the central Labrador Sea, Irminger Sea and Greenland Sea. In order to address the time evolution of the associated vertical mixing an index based on March mixed layer depth (MLD) is constructed for two of these locations. Irminger Sea mixing is combined with Labrador Sea mixing, rather than taken as independent index since both locations are part of the Subpolar Gyre. However, suggestions exist that Irminger Sea mixing might work independent (Pickart *et al.*, 2003) from LS mixing and might even pre-condition LS deep convection by bringing relative warm and saline water to the surface (Drange, pers.com.).

The locations and number of deep mixing events ($MLD > 1500m$) are shown in Fig. 5.1. Deep convection events in the central LS occur in almost 90% of the winters (47 out of 54) during the integration period. Irminger Sea convection occurs just a few times (less than 10% or 4 out of 54 winters) and Greenland Sea convection occurs in appr. 45% of the winters (24 out of 54).

For constructing the mixing index only grid points with a March MLD larger than 1500m at least once during the time period 1948-2001 are considered. Spatial averages of the MLD are calculated from these points. The time evolution of the two mixing indices is shown in Fig.5.2 (together with NAO index). A cross correlation between the two mixing indices of LS and GIN for different time lags shows a weak, not significant anti-correlation ($r = -0.3$) at the time lags -5 to -2 and 0 to 2 years. This anti-correlation holds only for certain periods, in particular for the end 1960th to early 1970th and early 1980th to mid 1990th. During the other periods the indices seem to be uncorrelated.

A cross correlation between the individual mixing indices and the overlaying atmospheric forcing, here the NAO index, shows significant covariability for certain time lags. An anti-correlation of $r = -0.4$ occurs for the lags -5 to -2 years between the GIN index and the NAO, while the LS index and the NAO correlate by almost $r = 0.5$ at lag 0.

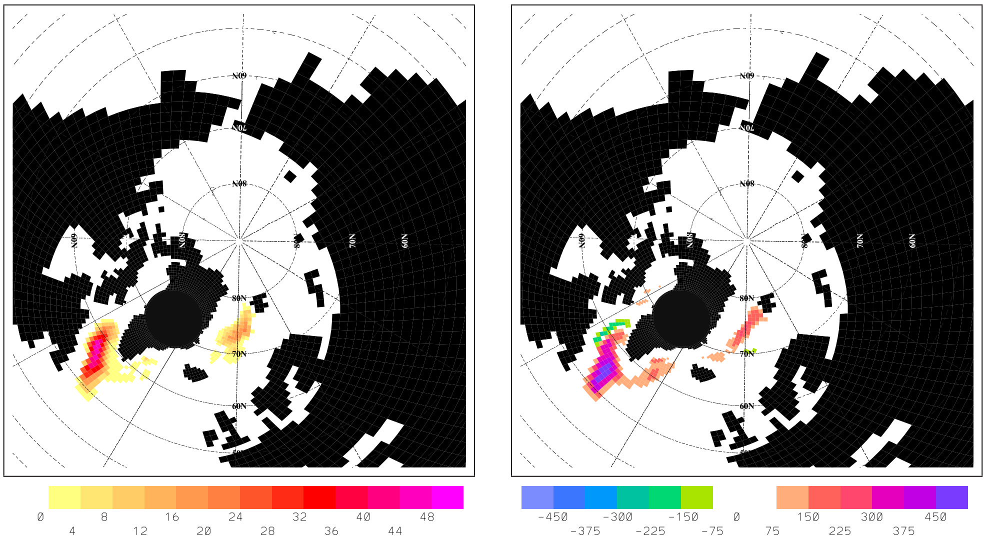

Fig. 5.1: *Left panel shows deep mixing events in the Labrador Sea and GIN Sea based on March mixed layer depth. Colors indicate number of winters during the 54 year NCAR/NCEP period with a mixed layer depth larger 1500m. Right panel shows a regression of the NAO index (DJF) on March mixed layer depth [m]. Units are [ ] and [m], respectively.*

A regression of the NAO index onto the ensemble mean simulated March mixed layer depth (Fig. 5.1) shows the largest impact over the LS area. Late winter MLD is enhanced by appr. 400 m per one standard deviation of the NAO index. The more pronounced Islandic Low during winters with positive NAO index drives a cyclonic atmospheric circulation anomaly over

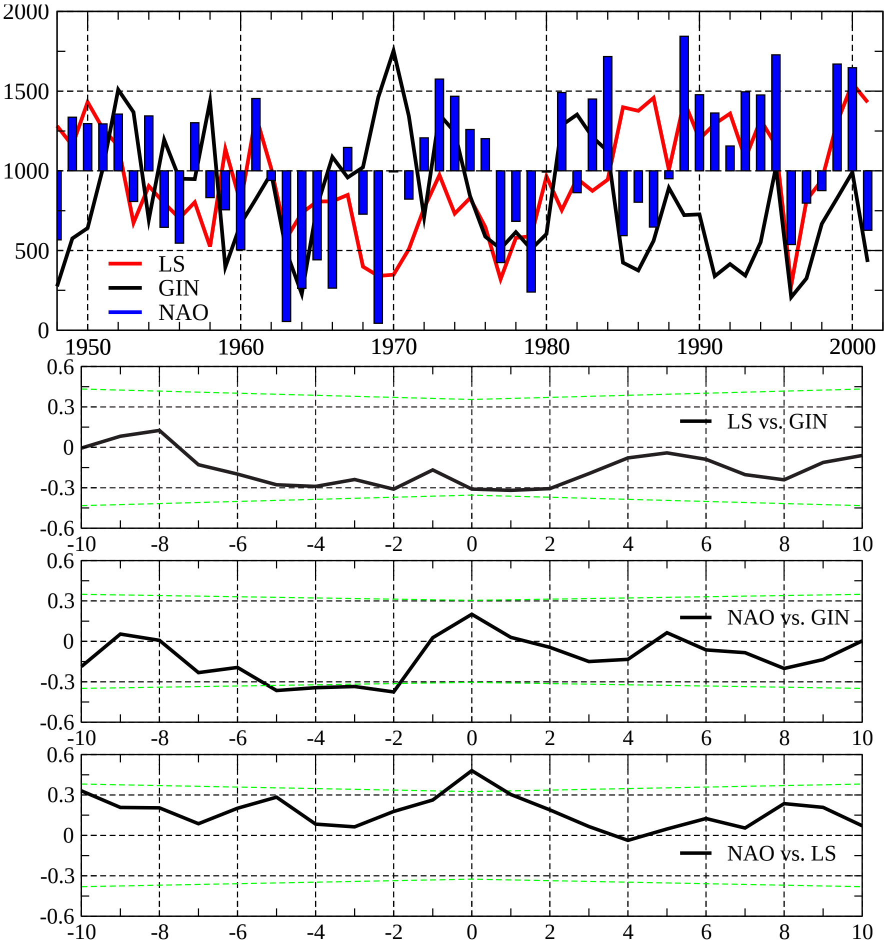

Fig. 5.2: *Upper panel shows the time evolution of the two mixing indices from LS (red), GIN (black) and the NAO (blue). Lower panels show cross correlations between the individual indices for different time lags. Green dashed lines indicate the 95% confidence level. Units are [m] and [], respectively.*

the Greenland/Island region. This anomalous atmospheric circulation induces enhanced advection of cold air from the inner Baffin Bay towards the LS, while at the same time more southerly winds over the GIN Sea causes reduced oceanic heat loss and a northward shift of the sea ice edge. Over the LS these northerly winds are associated with above normal sea ice conditions in Baffin Bay and Davis Strait (Deser *et al.*, 2002), and an enhanced buoyancy loss by the stronger atmospheric heat flux. Low-frequency variability in the atmospheric conditions on inter-annual time scales, and the associated changes in the vertical mixing, affects the production rate and properties of LSW, consistent with the results from Curry *et al.* (1998) and Dickson *et al.* (2002), e.g. LSW temperature anomalies (Fig. 5.3). However, beside the NAO forcing other factors like surface salinity conditions also play an important role in modulating deep water formation (see chapter

6).

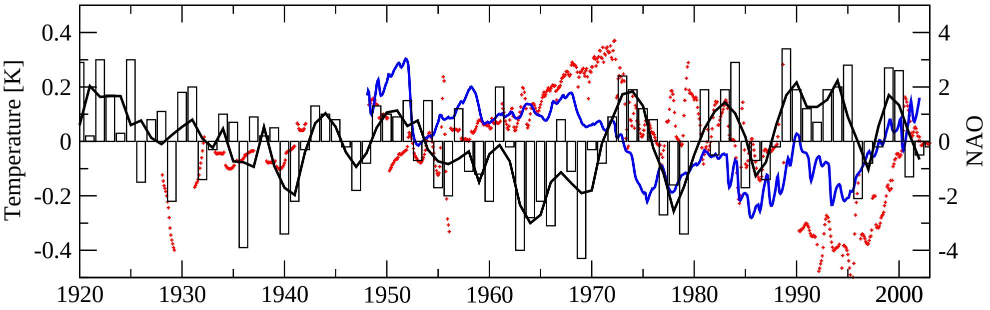

Fig. 5.3: *Central Labrador Sea temperature anomalies averaged between 1000-2000m depth. Shown are observations (red) taken from BIO database, the ensemble mean from the simulations (blue) and the DJF NAO index (black bars) and DJF NAO index smoothed by a 3 year running mean (black line).*

5.3 Labrador Sea Water

During the absence of substantial surface salinity anomalies the inter-annual to decadal variability of North Atlantic wintertime deep convection is dominated by the local atmospheric forcing. In particular, there exist a close relation between the Labrador Sea deep convection and the forcing by the NAO during the full simulation period as pointed out in the previous section. The low frequency shift in the NAO between the early and the late part of the second half of the last century manifests itself in a clear shift of the LSW properties. Caused by an almost persistent increase in LS convective activity after 1970 LSW properties change from warmer and saltier conditions in the 1950-1960th to a colder and fresher state in the 1980-1990th, consistent with observations, e.g. Curry *et al.* (1998); Dickson *et al.* (2002); Curry *et al.* (2003). Fig. 5.4 shows anomalous profiles of temperature and salinity in the center of the Labrador Sea near the position of Ocean Weather Ship (OWS) BRAVO from observations and the simulations. Observational data is taken form the Bedford Institute of Oceanography data base (*www.mar.dfo-mpo.gc.ca*). For the purpose of easy intercomparison the observational data is sampled and averaged into bins corresponding to the vertical model levels. Anomalies are calculated in respect to the climatological mean for each of these levels. The simulation captures the observed shift in the LSW properties between the warmest, saltiest conditions during 1960th to mid 1970th and mid 1980th to 1990th. The temperature between 1500 m and 2500 m decreases by appr. 1 K, while salinity decreases by almost 0.3 during the same time. Like in the observations there seems to be no renewal of cold fresh LSW after mid 1990th, salinities are slightly increasing afterwards. Consistent with the observations, production of the coldest, freshest LSW peaks in 1987 and 1994. LSW is drained southward into the North Atlantic. Signals in the LSW properties propagate with the Deep Western Boundary Current (DWBC) further southward and can be found with a time lag of 7 years at Bermuda (Curry *et al.*, 1998) and a few years later at the equator.

Dickson *et al.* (2002) argued that the low-frequency changes in the upper and intermediate layers of the LS are to a substantial part driven by the steady increase of the NAO and the associated increase in convective activity. Furthermore, they argue that the deep part of the anomalies, which is not directly affected by the LS convection, may originate upstream from a fresher upper column of the Nordic Seas and is communicated via the dense overflows in the resident deep waters from the northern North Atlantic. A freshening trend in the overflows would therfore show up in a freshening of the North East Atlantic Deep Water. However, the ensemble mean of the simulation fails to reproduce the observed freshening trend of both overflows (Dickson *et al.*, 2002). While there seems to be some correspondence for intermediate higher salinities during the 1970th in DSOW the simulation does not show the steady freshening after 1980. Instead the simulated salinities in both overflows have the tendency to slightly increase during this period. Yet the Arctic ocean and the Nordic Seas show a freshening trend in the ensemble mean. The simulated freshening in the Nordic Seas seems to be too much confined to the surface while the overflow properties seems to be influenced by an increased inflow of Atlantic water into the Norwegian Sea. This would be consistent with the generally too warm and salty conditions in the simulated overflows. This model shortcoming indicates that a large part of the LSW shift in the simulation might be locally forced in the LS by the trend in the atmospheric conditions rather than by a trend in the overflow properties. Wu *et al.* (2004) found a similar LSW freshening trend in their coupled atmosphere-ocean simulations for the 20th century. They attribute the trend to an upstream freshening of the Arctic Ocean and the Nordic Seas which is also present in the MPI-OM simulation, e.g. Arctic fresh water export through Fram Strait is increasing by appr. 10% during the simulation period. More details on the Arctic fresh water budget are shown in the next chapter. Furthermore, Wu *et al.* (2004) find an increase in LS convection and MOC strength, however in their case not associated with any trend in the NAO. Their results are in this aspect somehow contrary to the MPI-OM results presented above. They conclude that the observed freshening might not be an early signal of climate change. Differences of water-mass properties along the West Atlantic section between the decades 1957-1966 and 1990-1999 are shown in Fig. 5.5. Fresher and colder LSW can be found in the depth range from 1000 to 3000m between 40°and 60°N. Associated with the freshening is a cooling, compensating and even overcoming the salinity decrease effect on LSW density consistent with the observations documented in Dickson *et al.* (2002). As in the results from Wu *et al.* (2004) the LSW density increase is associated with an increase in MOC strength in this simulation (see next section). The trend towards colder and fresher conditions can also be found in other areas of the North Atlantic (Dickson *et al.*, 2002), e.g. an increasing trend in the fresh water transport of the LS current. At the same time temperature and salinity of the ocean in the tropical and subtropical upper North Atlantic have the tendency to increase due to a net increase in evaporation (Curry *et al.*, 2003). Southward between 20°N and 40°N in the depth interval 1000 m to 2000 m salinity increases. This increase is associated with an elevation of Mediteranien Deep Water salinity during this period consistent with observations, e.g. Roether *et al.* (1996) has documented an increasing salinity trend in the Mediteranian Deep Water during the last 40 years.

The question that arises is how these hydrographic changes are related to changes in the MOC.

a) Obs. Central LS Salinity b) Obs. Central LS Temperature

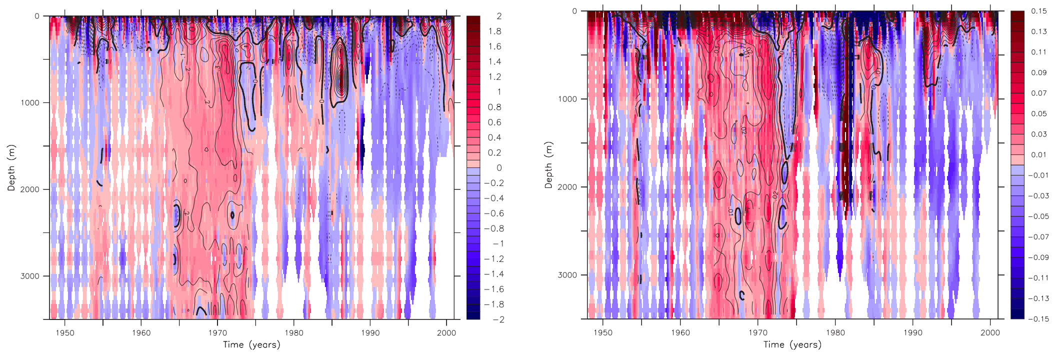

c) Sim. Central LS Salinity d) Sim. Central LS Temperature

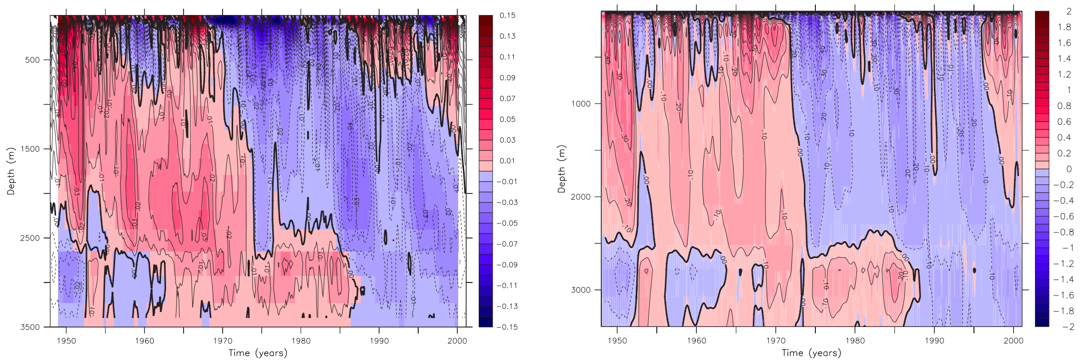

Fig. 5.4: *Observed (a,b) and simulated (c,d) anomalous salinity and potential temperature profiles in the central Labrador Sea near the position of OWS BRAVO. Units are [K] and [ ], respectively.*

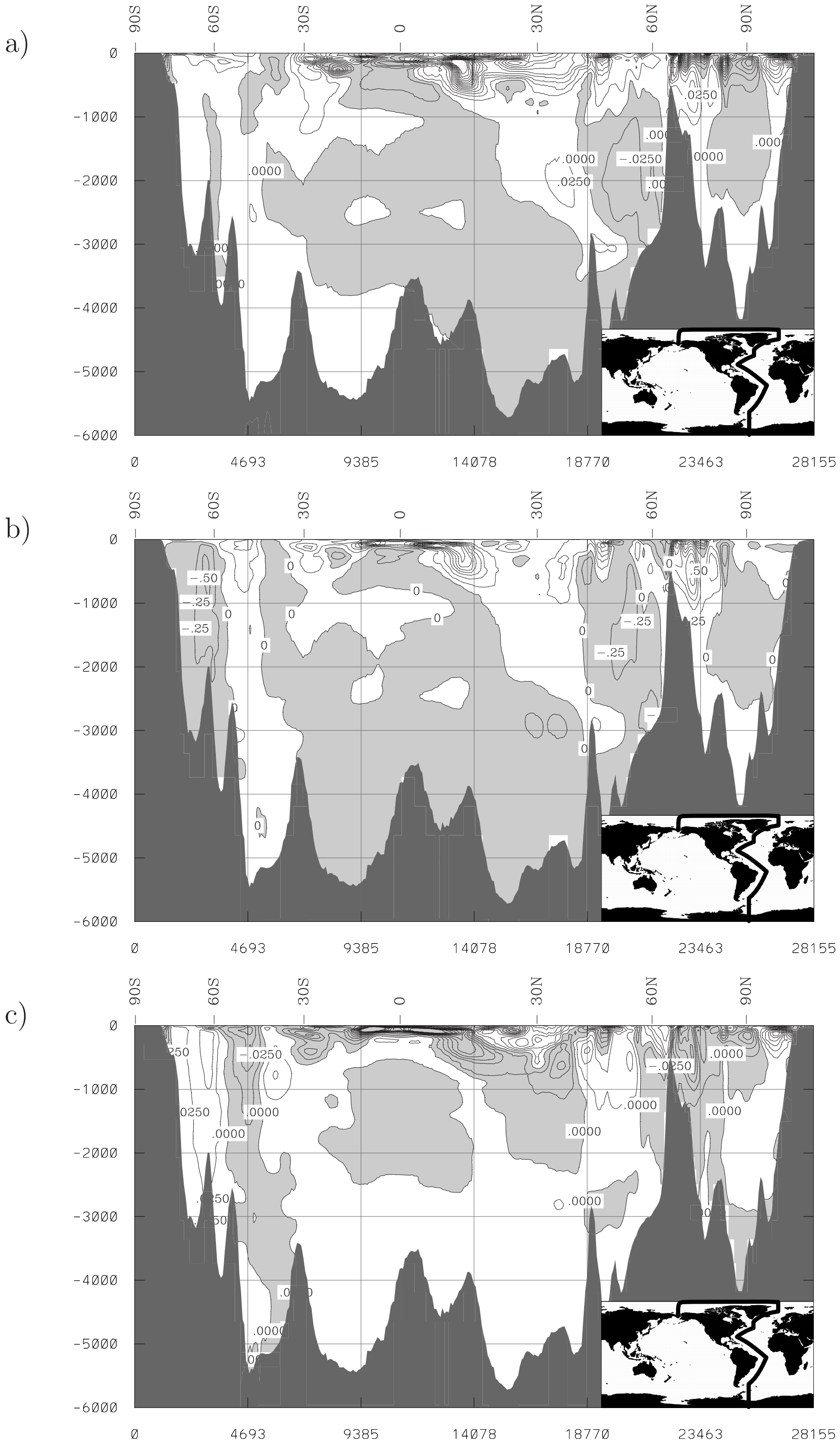

Fig. 5.5: *Simulated salinity, potential temperature and density (σ_2) difference in the West Atlantic for the decadal averages 1990-1999 minus 1957-1966. Units are [ ], [k] and [kgm^{-3}].*

5.4 Meridional Overturning Circulation

Simulated changes of the Atlantic MOC and heat transport are shown in Fig. 5.6. The inter-annual to decadal variability of the simulated MOC at 30°N shows a considerable spread in between the ensemble members. However, all model realizations yield minima around 1960 and 1980, and maxima in the late 1990th. The ensemble mean MOC at 30°N shows a gradually increasing trend from the 1960th to 2000 of 0.5 Sv per decade, while individual realizations have trends between 0 and 1 Sv. Still the coherent behavior of the individual realizations in the inter-annual to decadal frequency band indicates just a weak dependency of this variability from the ocean initial state. Similar findings where made with the MICOM model (Drange, pers. com.). The simulated increase in Atlantic MOC is consistent with an increase in LSW/NADW production, and a strengthening of the DWBC.

North of 62°N (LS excluded) there seems less MOC variability on the inter-annual to decadal band. However, just south of the LS at 50°N this inter-annual to decadal variability seems well developed, suggesting the LS to be the major source for variability in this frequency band. The same holds for the associated heat transport. At 30°N the heat transport has an increasing trend of appr. 0.025 PW per decade, while at 62°N no obvious trend exists.

Associated with changes of the Atlantic MOC are changes in the meridional heat transport. Fig. 5.7 shows a Hovmoeller diagram of the Atlantic MOC anomalies. Values where diagnosed as local maxima of the meridional stream function below 1000m depth. Inter-annual MOC anomalies have their largest amplitudes between 20°N - 50°N in the subtropical North Atlantic and are associated with variability of the Gulf Stream/NAC and the Deep Western Boundary Current return flow. Inter-annual anomalies can reach $\pm 2Sv$. Anomalies north of the Greenland-Scotland Ridge are considerable smaller, again pointing to the LS as source region for inter-annual to decadal MOC variability. Across all latitudinal bands MOC anomalies can reach appr. 10% to 15% of the climatological mean mass transports.

The simulated meridional heat transport has most variability in the southern and tropical Atlantic between 30°S and 20°N, probably related to variability in the deep Atlantic outflow and inflow in the Agulhas Current. In the North Atlantic individual anomalies can reach 0.1 to 0.15 PW, again appr. 10% to 15% of the climatological mean.

Diagnosing the evolution of the three-dimensional structure of the MOC during the simulation period reveals considerable changes. Differences between the decade of minimal MOC strength (1957-1966) versus maximal MOC strength (1990-1999) are shown in Fig. 5.8 and can be compared against the climatological mean in Fig. 4.5. The intensification of the MOC

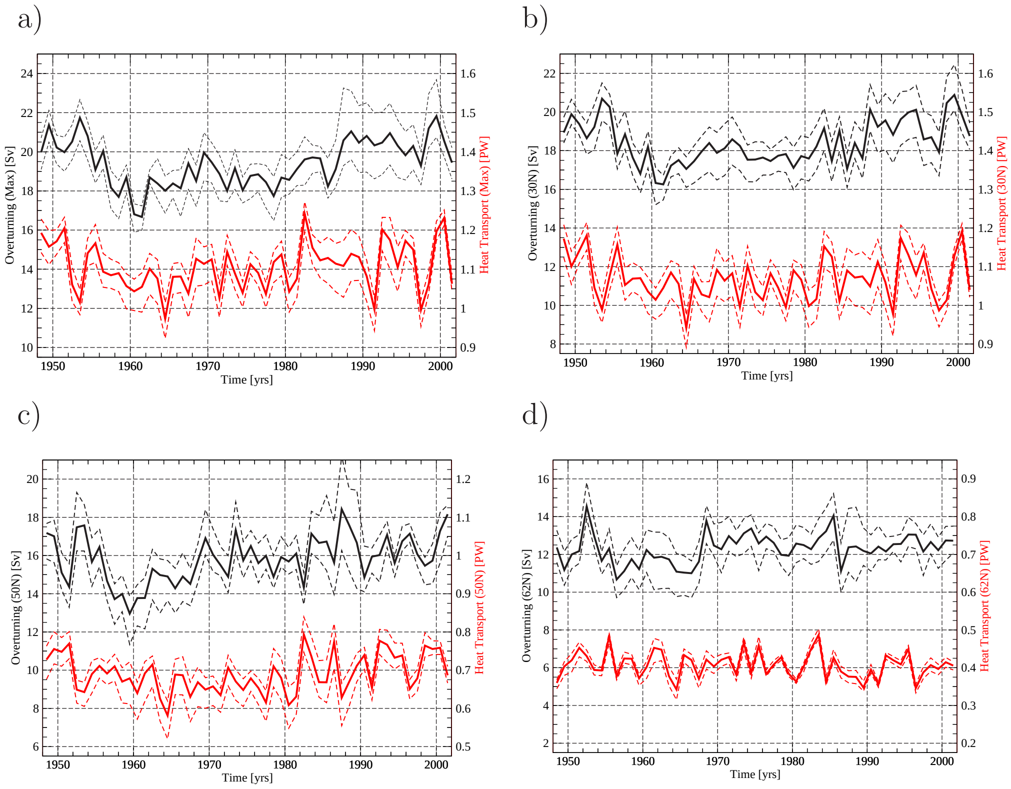

Fig. 5.6: *Ensemble mean Atlantic heat transports [PW] (red) and strength of the Meridional Overturning Circulation [Sv] (black) as maximum between 30°S and 62°N (a) and across the latitudes 30°N (b), 50°N (c) and 62°N (d). Dashed lines indicate the spread between the ensemble members.*

is clearly visible in the individual branches. In the upper and intermediate density class ($\sigma_2 < 36.8$) the prominent signal is an intensification and northward shift of the NAC. These simulated changes are consistent with the results of Frankignoul *et al.* (2001) and Curry and McCartney (2001). At the same time the North Equatorial Current shifts southward, resulting in a larger and stronger Subtropical Gyre. In the deep density class ($38.8 < \sigma_2 < 37.05$) the strength of the DWBC increases. Between 30°N and 50°N the current's position shifts westward, possibly related to the northward shift of the NAC, as both currents are known to interact.

Downward diapycnal fluxes into the deep density class layer in the LS increase by appr. 1-2 Sv (appr. 40%), as does the entrainment of the Faroer Bank Channel overflow (1 Sv or 30%). In the bottom density class ($\sigma_2 <$

a) Atlantic Meridional Overturning Anomaly

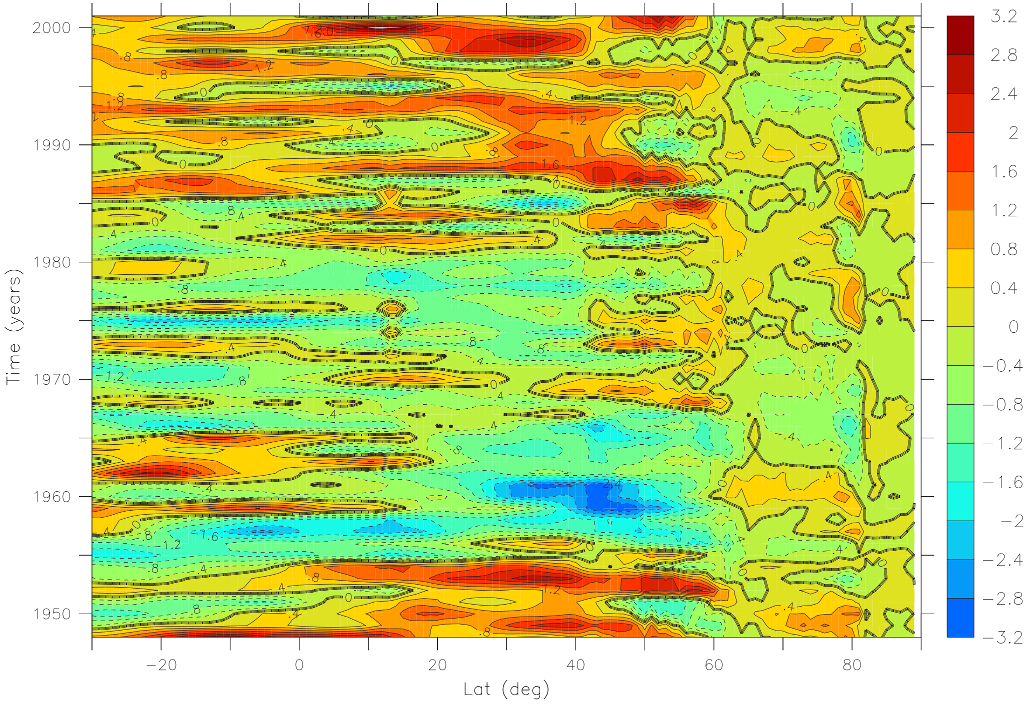

b) Atlantic Heat Transport Anomaly

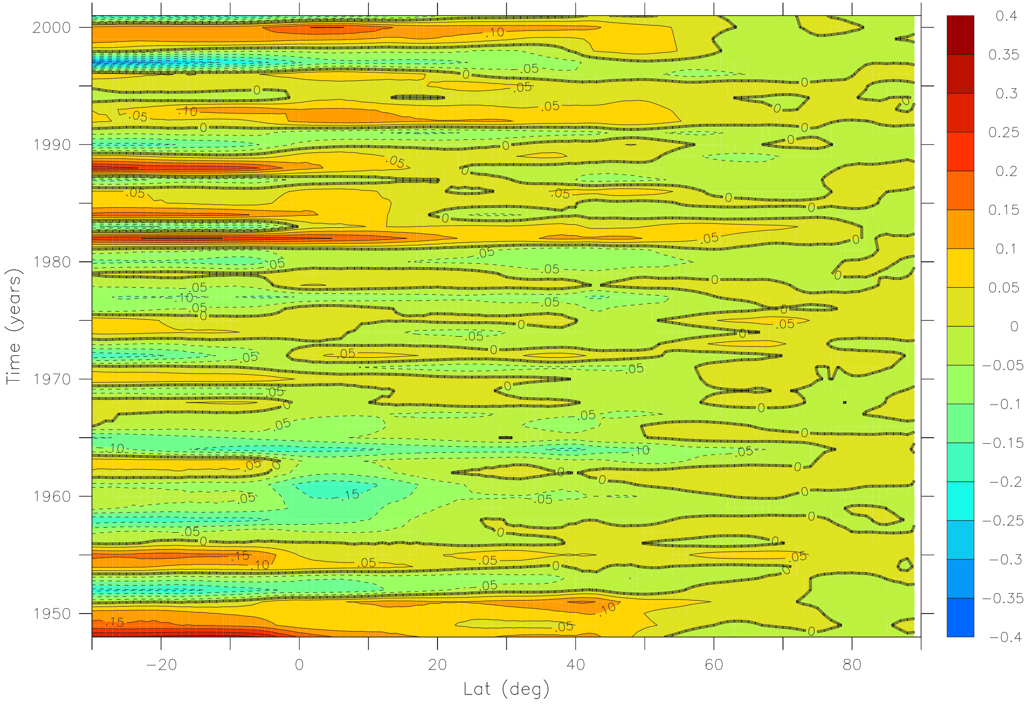

Fig. 5.7: *Ensemble mean Atlantic MOC (a) and heat transport (b) anomaly. Units are [Sv] and [PW], respectively.*

37.05) a clear reduction of both overflows occurs. The upward diapycnal mass fluxes from the Faroer Bank channel and Denmark Strait overflow into the deep water layer reduces by appr. 1 Sv, respectively. Downward diapycnal flux in the bottom layer of the Nordic seas is reduced by 2 Sv (appr. 30%). These findings are consistent with the estimates by Hansen *et al.* (2001), in which a reduction of the Faroer Bank Channel overflow by 20% between the 1950th and 1990th is suggested.

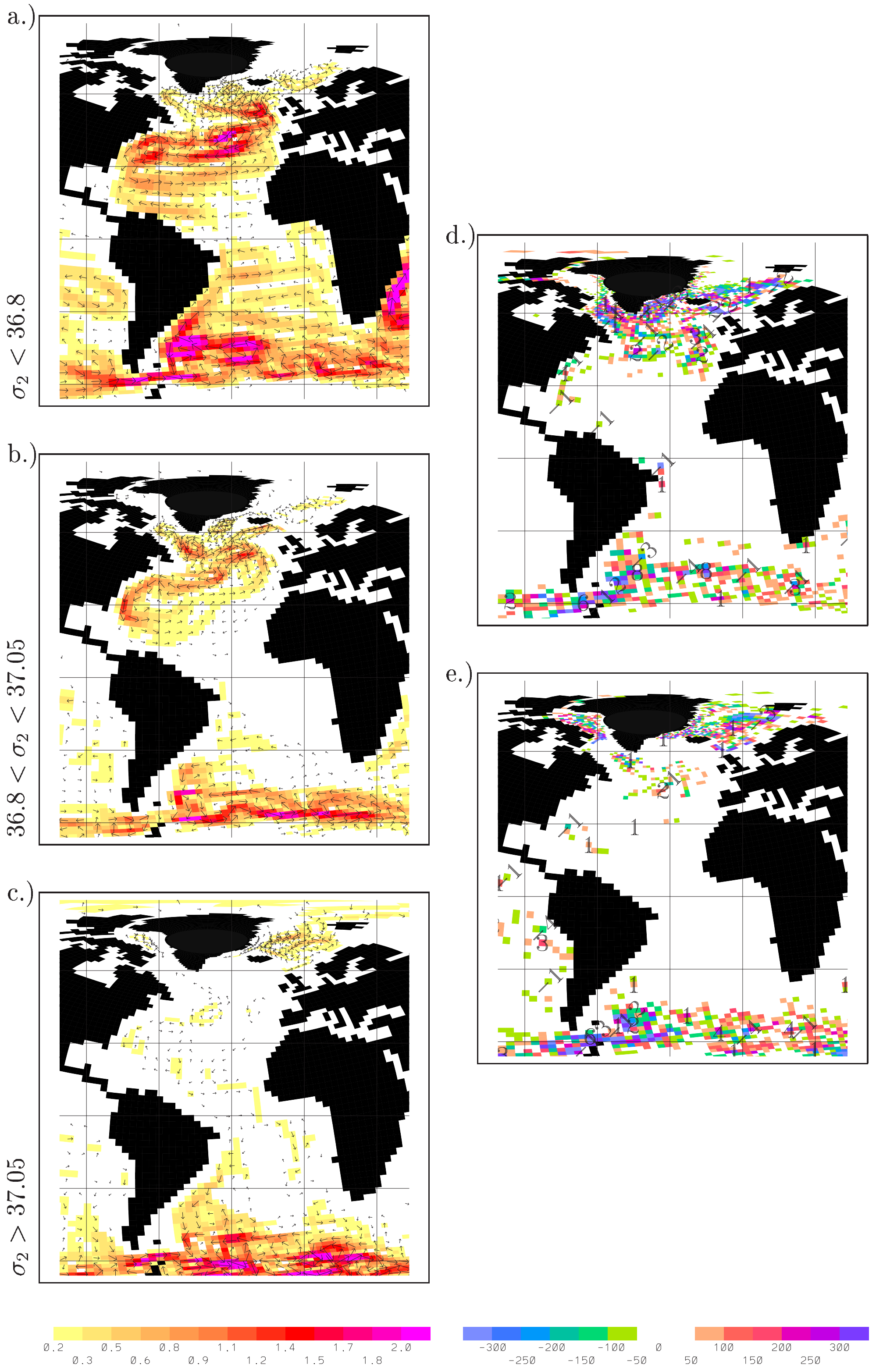

Fig. 5.8: *Ensemble mean iso- and diapycnal mass fluxes in three density layers corresponding to upper and intermediate, deep and bottom waters. Shown is the difference between the two periods 1990-1999 minus 1957-1966. Left column (a,b,c) shows local isopycnal fluxes in each layer; every second arrow is plotted. Units are [Sv]. Right column (d,e) shows diapycnal fluxes in between the layers. Colors indicates diapycnal velocities and numbers indicate the associated diapycnal transports (negative = upward). Units are [m/yr] and [Sv], respectively.*

5.5 Multi Decadal Variability in the MOC

Additional to the inter-annual to decadal variability of the Atlantic MOC, that does show only moderate dependency from the initial state in the ocean, there are low-frequency trends of MOC strength underlying. In contrast to the shorter time variability these trends seem to depend largely on the ocean initial conditions. Some ensemble members have a positive, some a neutral trend in MOC strength, some even show a negative trend. Fig. 5.9 shows the MOC evolution in all experiments and the non-deterministic part with the ensemble mean removed. Amplitudes of the individual trends are in the order of $\pm 1.5 Sv$. Since all realizations use the same atmospheric forcing as boundary conditions, these low-frequency trends seem to be determined by the ocean initial state, in particular the oceanic density field. This points towards the possibility of large predictability for longer term trends of the MOC, if the ocean initial state is sufficiently accurate known. Pessimisticly formulated this would mean, without knowledge of the ocean state in 1948 it seems difficult to estimate an reliable trend for the last 50 years in the MOC from this integrations. The spread of the ensemble members provides some estimate for the uncertainty in respect of the ocean initial condition.

The time evolution of overflow water density across Denmark Strait and the Island -Scotland Ridge shows a close relationship to the multi decadal variability of the Atlantic MOC. Fig. 5.10 shows anomalies in respect to the ensemble mean of the MOC at 30°N and the anomalous density of the DSOW. Both time series are significantly correlated, with correlation coefficient larger 0.3 for time lag between -20 to 20 years. The maximum correlation is found at -5 years time lag with MOC leading DSOW density anomalies. However, a clear lead/lag relationship cannot be identified. During increasing phases the MOC seems to lead, while for the decreasing phases the overflow density seems to lead. Jungclaus *et al.* (2004) finds an stochasticly forced ocean only mode of multi decadal variability in coupled integration with ECHAM5/MPI-OM that behaves similar. The underlying mechanism involves an interplay between Arctic fresh water exports and LS convection on multi decadal timescales. In particular, changes in the Nordic Sea circulation feeds back on Arctic fresh water exports, which in return influence the MOC strength.

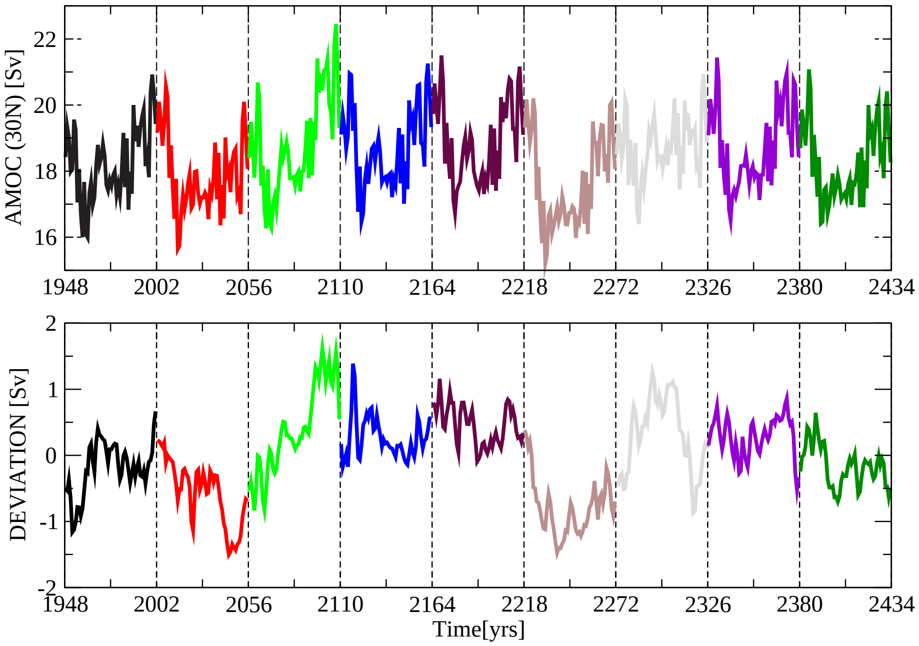

Fig. 5.9: *Time evolution of the MOC at 30°N for all the individual realizations. Lower panel show the deviation of the ensemble mean. Units are [Sv].*

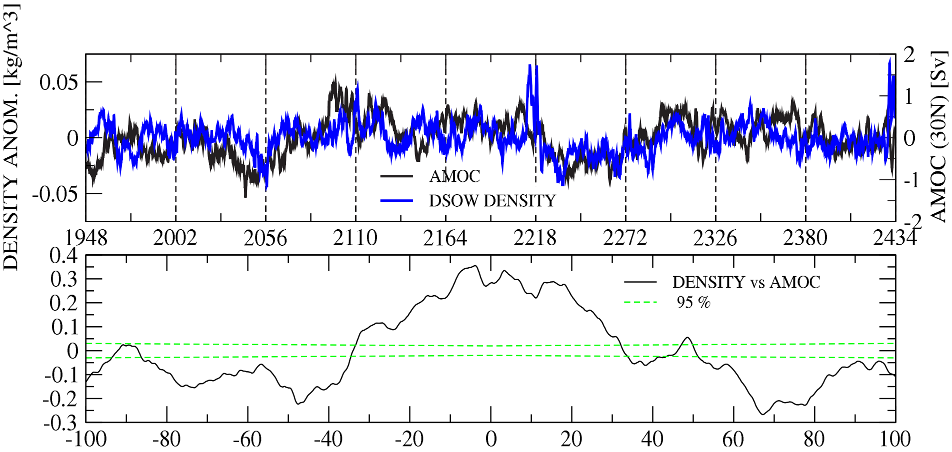

Fig. 5.10: *Anomalous MOC strength and density anomalies in the Denmark Strait overflow for the individual realizations. Lower panel shows a cross correlation between the two upper curves. Dashed green line indicates the 95% confidence level. Units are [Sv],and [kgm^{-3}], respectively.*

5.6 MOC and NAO

The close relation of MOC and NAO during the simulation is presented in Fig. 5.11. The MOC at 30°N and NAO covary closely linked, in particular after the 1980th. A lag correlation analysis reveals a significant correlation above 0.4 with NAO leading MOC by appr. 1 year. In the coupled experiments the correlation is weaker but still significant with a lag of zero years. A cross spectral analysis of NAO and MOC variability reveals significant coherence at periods between 2-3 years and 5-8 years (Fig. 5.12). In these bands NAO and MOC covary in phase. However, no indication for a link between NAO and MOC on longer time scales can be found in the coupled simulation. The NAO spectrum shows white-noise variability, while the MOC spectrum shows increased variability in the low-frequency band. This indicates that in the coupled model other factors dominating low-frequency MOC variability, e.g. Arctic fresh water exports (Jungclaus *et al.* (2004)).

MOC strengths at 30°N from the sensitivity runs with the filtered forcing fields are shown in Fig. 5.13. The control runs with the unfiltered forcing shows a close correspondence with the NAO index. The sensitivity runs reveal that much of the inter-annual variability is related to the mechanical forcing by the atmosphere, in particular the winds associated with NAO. The experiment with the full wind stress, but damped thermal and fresh water forcing reproduces the inter-annual variability of the control run, while the complementary run does not. The lower-frequency variability of the MOC, in particular its increase after 1970 seems to large parts thermal and fresh water driven. The experiment with the damped wind stress and full thermal and fresh water forcing can reproduce the trend from the control run. The run with all forcing fields filtered, as well as the run with the damped thermal and fresh water forcing, show a clear reduction in the MOC strength by appr. 3 Sv. Since the mean seasonal cycle is maintained in all experiments, this indicates that the variability in NAO signal itself contributes to a strenghtning of the MOC. This is further supported by sensitivity studies where just an persistent NAO high (respectively NAO low) forcing was applied. While the NAO low forcing leads to a weakening of the MOC due to decreased LS convection, the NAO high forcing has the tendency to increase MOC strength. However this reverses after a few decades. The elevated NAO index is associated with increased Fram Strait sea ice exports and leads to a continuously freshening of the LS and consequently a reduction of the MOC strength.

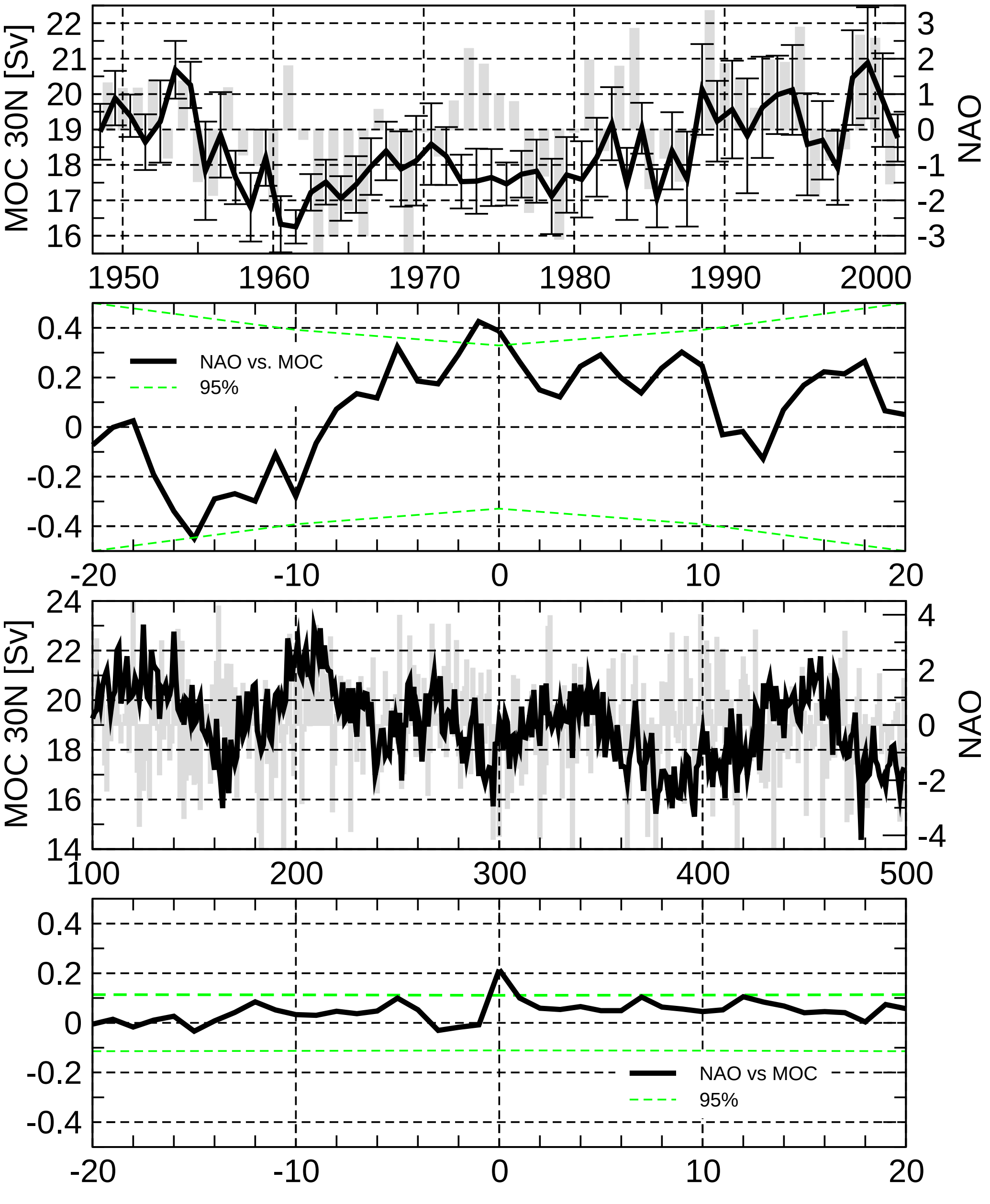

Fig. 5.11: *Ensemble mean Atlantic MOC [Sv] at 30°N and NAO Index (gray). Bars indicate the spread between the ensemble members. Also shown is a cross correlation for several time lags, negative lags mean that NAO is leading MOC. Green dashed lines indicate the 95% confidence level. Lower two diagrams show the same from the coupled model ECHAM5/MPI-OM.*

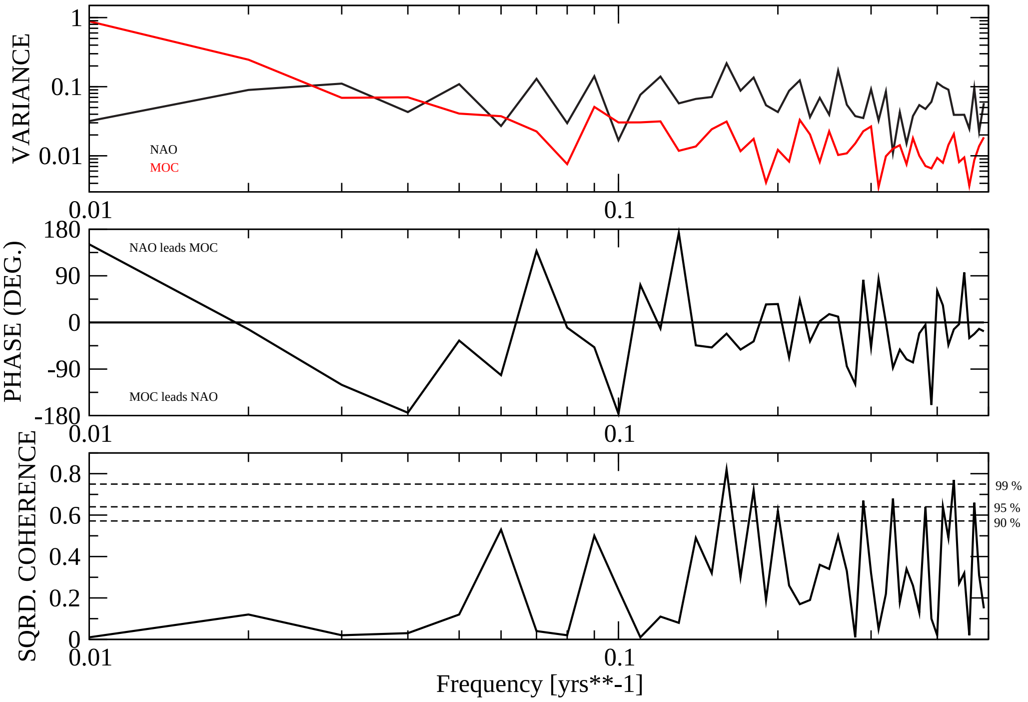

Fig. 5.12: *Cross spectral Analysis between NAO and MOC from coupled model ECHAM5/MPI-OM.*

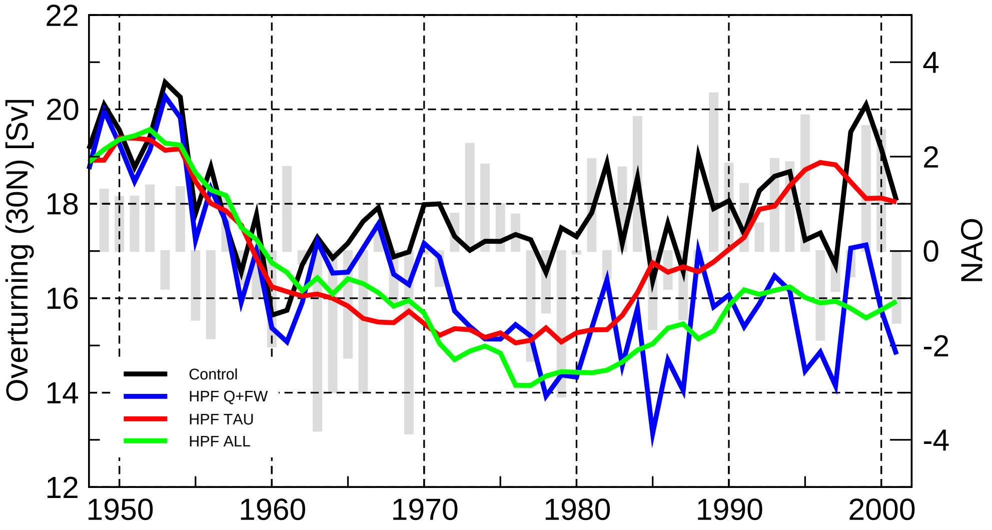

Fig. 5.13: *Atlantic meridional overturning at 30°N from control run (black) and runs HPF Q+FW (blue), HPF TAU (red) and HPF ALL (green). Gray bars indicate the NAO index. Units are Sv* $(= 10^6 m^3/s$.

5.7 MOC and SST

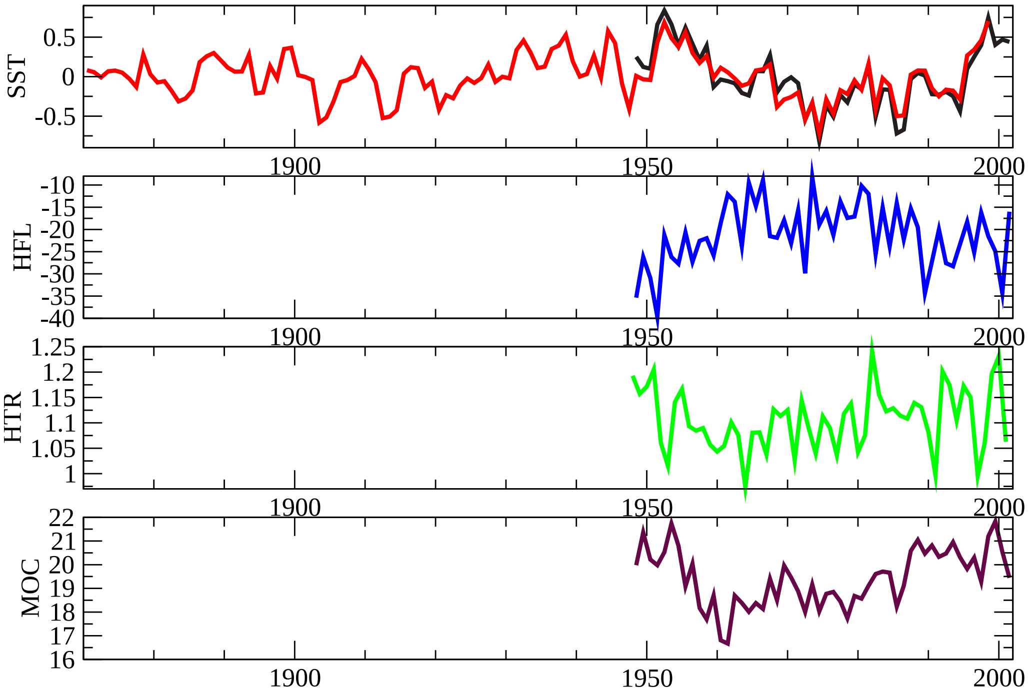

Fig. 5.14: *SST index as suggest by Latif* et al. *(2004) from observations and the ensemble mean of the simulation. Also show is the atmospheric heat flux over the index region, the ocean heat transport and the strengths of the Atlantic MOC at 30°N. Units are* $K, W/m^2, PW and Sv$

.

As pointed out by Latif *et al.* (2004) a close relationship between the Atlantic MOC (and the associated northward heat transport) and North Atlantic SST exist in the region between 40 - 60°N. The authors suggest that an index based on SST of this region can be used as a proxy to monitor and reconstruct MOC variability. Fig. 5.14 shows the ensemble mean SST index from the uncoupled simulations. SST anomalies in the index region start at elevated values in the 1950th and drop until mid 1970th, afterward SST anomalies increase again until today. The simulation captures SST variability of the observations (here Hadley Center SST) well. The atmospheric heat flux over the region acts to damp the SST anomalies, while the ocean heat transport and the MOC at 30°N lead the SST anomalies by appr. 5-10 years. This suggests that ocean heat transport is strongly affecting SST variability in this region, consistent to the results from the coupled atmosphere-ocean simulations by Latif *et al.* (2004). The increase in the observed SST index indicates an increase of the MOC strength during the last 4 decades, consistent to the results presented in this study.

6. RESULTS: SIMULATED VARIABILITY IN THE ARCTIC

6.1 Introduction

The Arctic is an important fresh water source for the North Atlantic, influencing stratification and thus the vertical circulation in the North Atlantic sinking regions. Small variations in fresh water supply from the Arctic (via the East Greenland Current) into the North Atlantic can alter or even prevent convection in the LS for several years. The GSA of the early 1970th Dickson *et al.* (1988) is an example of such an event. The previous section demonstrated that LS winter time deep convection is strongly influenced by the North Atlantic Oscillation on inter-annual to decadal timescales. This chapter addresses North Atlantic/Arctic interactions and their impact on the THC. In particular, the chain of processes that led to GSAs in the LS is presented.

6.2 Arctic Ocean Sea Ice Variability

Figure 6.1 illustrates the time evolution of Arctic/North Atlantic sea ice properties during the simulation period. The sea ice time series exhibit pronounced inter-annual to multi decadal variability with a relatively small spread between the individual ensemble members (less than 0.5 standard deviation of the ensemble mean). This indicates that the simulated sea ice variability is dominated by the atmospheric boundary conditions, rather than by the initial conditions. The annual, winter centered (Aug.-Jul.) mean sea ice volume reaches maxima in the mid 1960th, early 1980th and late 1980th. The lowest values in the simulation occur in the mid 1950th and the late 1990th. During the first two decades sea ice volume increases from its initial value of appr. 17000 km^3 by almost 47% to over 25000 km^3 in 1966. The sea ice covered area increases at the same time by roughly 10% from 7.2 $*10^6 km^2$ to 8.0 $*10^6 km^2$. The area-averaged central Arctic sea ice thickness increases by over 33% from 2.4 m to almost 3.2 m. Sea ice thickness stays at rather high values for the next two decades of the simulation, with a weak intermediate maximum in 1980/81 and a third pronounced maximum in 1987/88. During the last 15 years of the simulation a decrease in sea ice thickness occurs. Sea ice volume drops by approximately 30% from 25000 to 18000 km^3, sea ice area by 10% from 8.0 to 7.2 $*10^6 km^2$ and sea ice thickness by 20% from 3.1 m to 2.5 m. Typically simulated sea ice-covered-area changes are less than 10% of the long term average, whereas sea ice volume changes are in the order of 30-40%. Consequently the major sea ice volume changes have to occur mainly by changes in sea ice thickness.

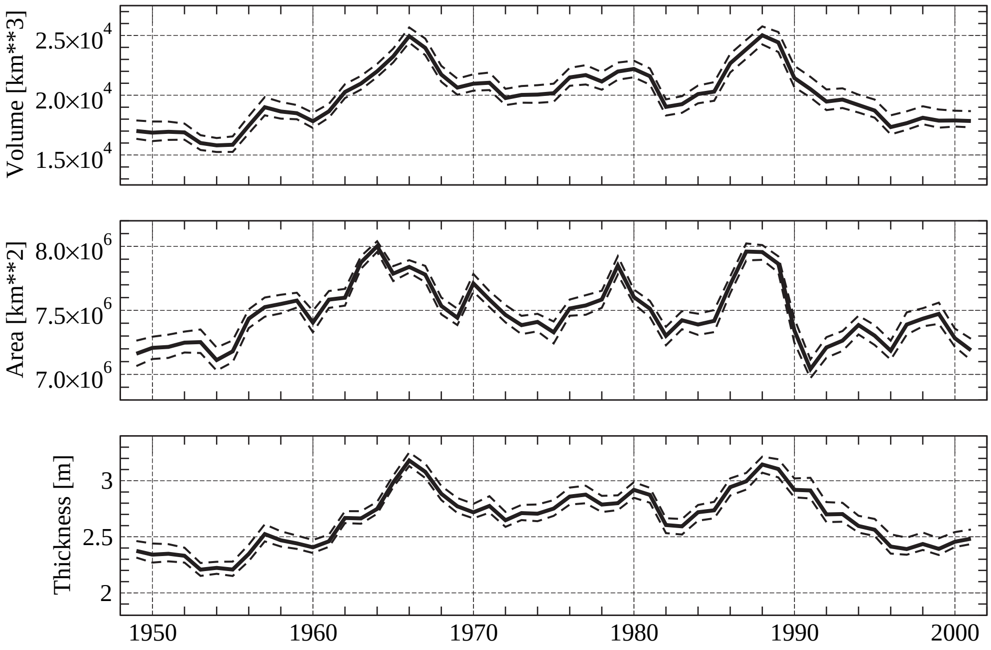

Fig. 6.1: *Time evolution of simulated Arctic/North Atlantic sea ice properties. Upper panel shows sea ice volume, middle panel shows sea ice area and lower panel shows sea ice thickness. Units are [km^3], [km^2] and [m]. All values are annual means centered on winter (Aug.-Jul.). Thin dashed lines indicate the ensemble range.*

The simulated sea ice thickness decrease after the late 1980th is consistent with the estimates by Rothrock *et al.* (1999) and Wadhams and Davis (2000) based on submarine sea ice draft data. Both studies show central Arctic sea ice thickness reduction of appr. 40% between the period 1958-1976 and the mid 1990th. Winsor (2001) showed that there is no significant negative trend during the mid 1980th and mid 1990th for the central Arctic and the Beaufort Sea. However, a clear negative trend shows up in a 20 year record (1978-1998) of sea ice thickness estimates based on observations of sea ice surface oscillations presented by Johannessen *et al.* (1999). Their estimates show an intermediate peak in sea ice thickness around 1988, which is reproduced in the simulation. Finally, no obvious long-term trend in the Arctic sea ice properties can be seen in the simulation if one considers the full period. Sea ice properties in the late 1990th, for instance are as low as during the early 1950th.

As mentioned earlier, sea ice covered area variability is largely constrained by the prescribed surface forcing. A comparison between simulated and observed sea ice extent variability provides still useful information on the quality of the model and the forcing data set. A comparison for inter-annual variability of sea ice extent anomalies is shown in Fig. 6.2. Satellite based observations are taken from Johannessen *et al.* (2002) . The model captures the inter-annual variability reasonably well, in particular the miminum in 1995 is reproduced. However, the observed maximum of sea ice extent in 1982 is underestimated by the model, while the intermediate maximum of 1989 is overestimated. Summer minimum sea ice extent variability is much larger than that of the winter maximum, consistent with observations. A slight negative trend in sea ice extent of appr. $25000 km^2/yr$ is present in the simulation and the observations after 1980. This trend corresponds to observations by Parkinson *et al.* (1999), but cancels if one considers the full simulation period.

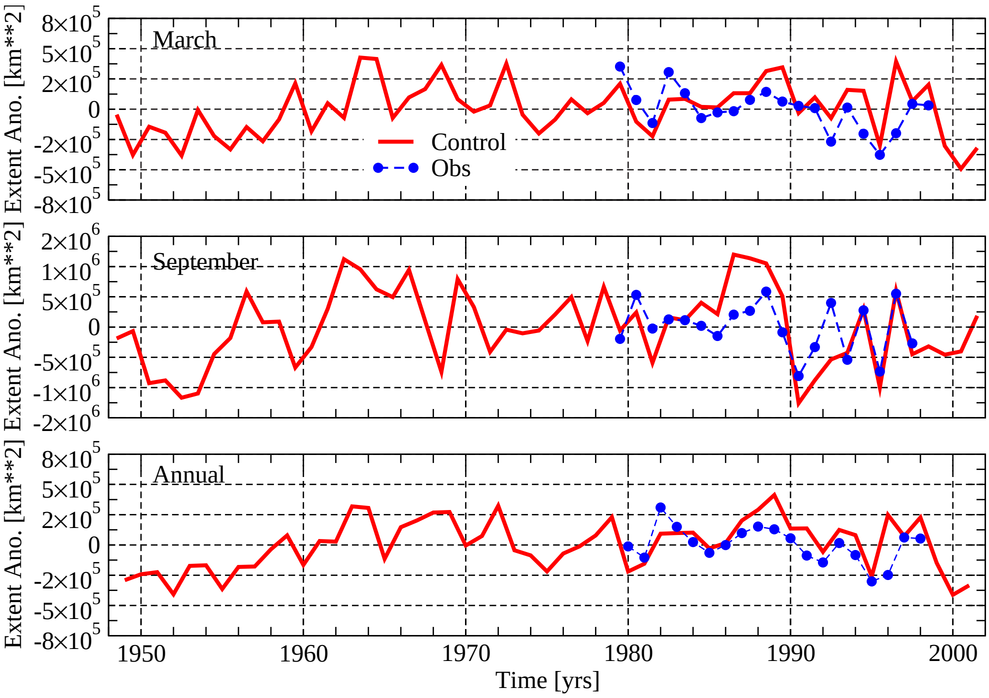

Fig. 6.2: *Time evolution of sea ice extent anomalies (solid red) for March, September and annual mean (Aug.-Jul.) and the corresponding observations by Johannessen* et al. *(2002). Units are [km^2].*

A regression of annual mean sea ice volume anomalies onto sea ice thickness and concentration is shown in Fig. 6.3. While thickness changes mainly occur in the eastern Arctic/Laptev Sea region, as well as along the Canadian Archipelago, most changes in sea ice concentration are located in the Barents Sea. Additionally, sea ice concentration changes lead thickness changes by app. one year, suggesting that both anomalies are linked to the same atmospheric forcing anomaly. The relative small spread between the individual ensemble members indicates that atmospheric boundary conditions dominate the sea ice variability of the Arctic. However, in the region of the Barents Sea also oceanic interaction, e.g. the Barents Shelf inflow of relative warm, saline water of North Atlantic origin, can become important.

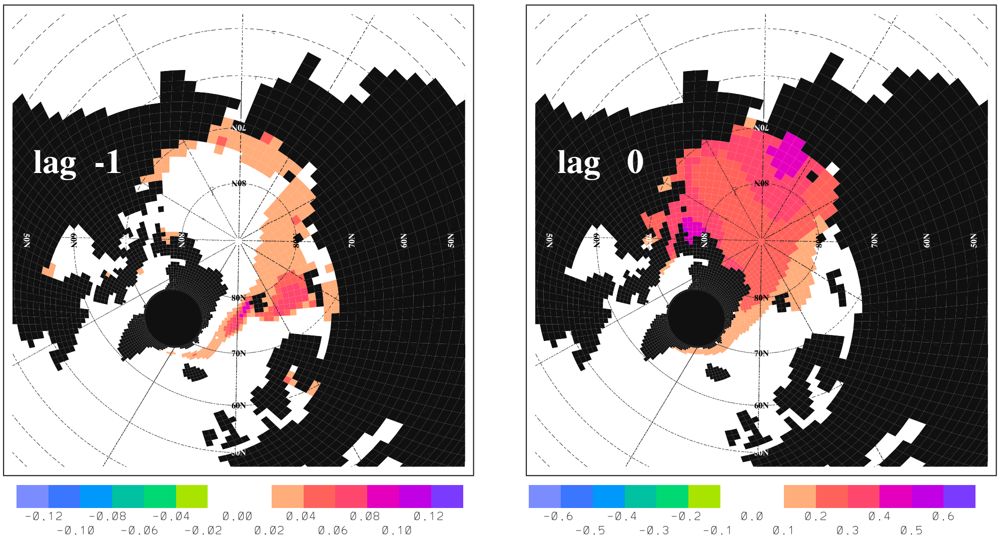

Fig. 6.3: *Regression of Arctic sea ice volume on sea ice concentration (left) and sea ice thickness (right) for the lags -1 and 0 years, respectively. All values are annual means centered on winter (Aug.-Jul.). Units are [ ] and [m], respectively.*

6.2.1 Sensitivity Experiments

Variations in sea ice cover reflect variations in the local sea ice production as well as variations in the sea ice transport. The sensitivity experiments with the modified forcing fields (3.1) reveal that Arctic sea ice volume, area and thickness variability is forced to equal parts by the wind and by the thermal + fresh water forcing, respectively. A linear superposition of the sensitivity runs with hp-filtered wind stress and hp-filtered thermal + fresh water forcing reproduces the variability of the control run reasonably well (Fig. 6.4). In particular, the sea ice volume maxima and minima are reproduced in both sensitivity experiments. However, the longer term trends, e.g. the increase of sea ice volume from the late 1950th to the mid 1960th and the decrease after the late 1980th, are not reproduced by the sensitivity experiment with hp-filtered thermal + fresh water forcing. These longer term trends seem to depend on low-frequency atmospheric thermal and fresh water anomalies, rather than on low-frequency dynamical changes in the atmospheric circulation. A lag regression of Arctic sea ice volume anomaly on atmospheric forcing fields is shown in Fig. 6.5 for the lags -2 and 2 years. Five to zero years prior to the peaks in sea ice volume the air temperature over the Arctic is considerably colder than normal. The associated temperature decrease is 0.5 to 1°C per standard deviation of ice volume change, which adds up to -1.5 to -3°C. The cold temperature anomalies are accompanied by above normal SLP anomalies over the Beaufort Gyre and north east of Island. Anti-cyclonic wind stress anomalies reduce the Fram Strait Sea ice export and increase the strength of the anti-cyclonic Beaufort Gyre. Proshutinsky *et al.* (2002) showed in their model that an increased Beaufort Gyre can store substantial amounts of fresh water by tilting the isohaline surfaces inside the gyre downward. Similar fresh water accumulation takes place in this simulation, which provides a positive feedback on sea ice growth, due to further freshening and cooling of the ocean surface layers. In this way both - atmospheric wind and temperature anomalies - contribute to an increased sea ice production. The situation is almost reversed after the sea ice volume maximum. While surface air temperatures are at normal conditions, there is a pronounced negative SLP anomaly over the central and eastern Arctic. The associated cyclonic wind stresses increase the Fram Strait sea ice export and weaken the Beaufort Gyre. The anomalous fresh water stored in the gyre is released during the spin down. The simulations support the hypothesis from Proshutinsky *et al.* (2002) that the Beaufort Gyre could act as an additional storage space for fresh water, beside sea ice.

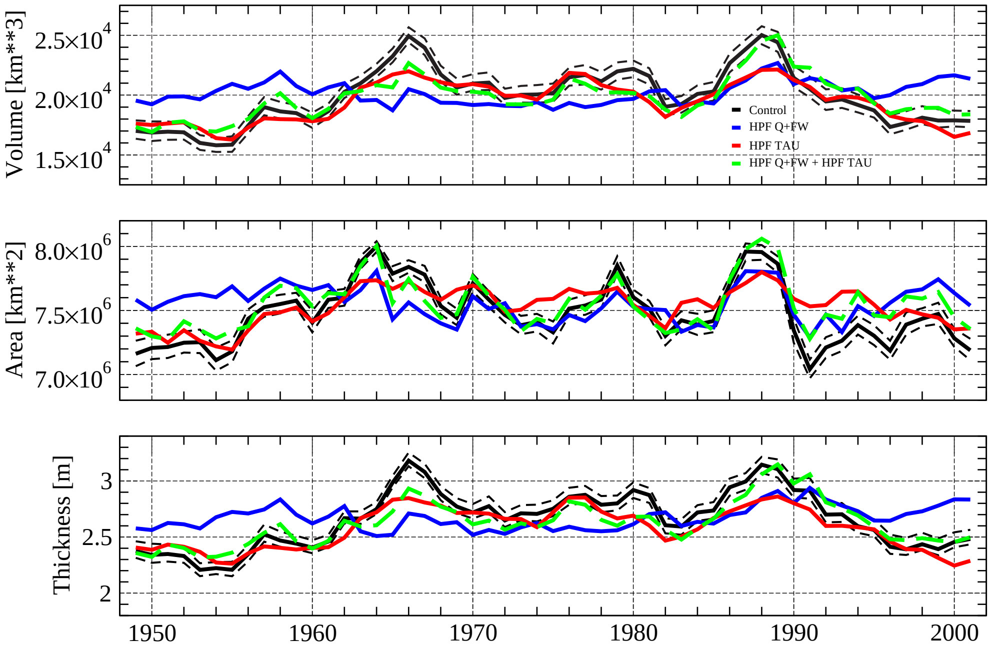

Fig. 6.4: *The same as Fig. 6.1, but for the control run (ensemble mean, solid black, thin dashed lines indicate the ensemble range) and the sensitivity runs HPF Q+FW (solid blue) and HPF TAU (solid red) and their linear superposition (dashed green).*

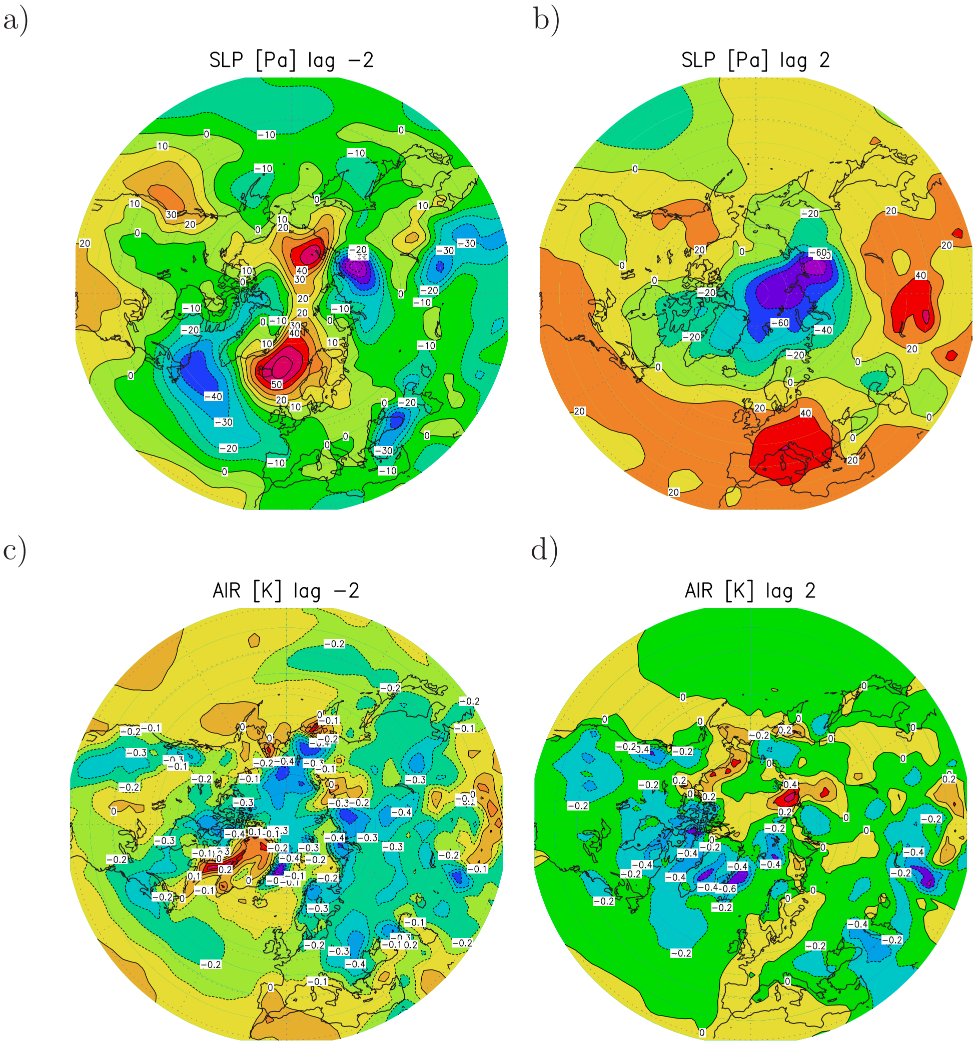

Fig. 6.5: *Lag regression of Arctic sea ice volume on sea level pressure (upper row) and 2m air temperature (lower row) for the lags -2 (left column) and 2 years (right column). All values are annual means centered on winter (Aug.-Jul.). Units are [Pa] and [°K], respectively.*

6.3 Arctic Ocean Sea Ice Export Variability

Arctic sea ice exports are shown in figure 6.6. Volume transports are given in units of liquid fresh water. As discussed earlier, Fram Strait sea ice export is the most important contributor to total sea ice export. The simulated variability of the sea ice volume transport agrees well with numerical experiments by Hilmer et al.(1998) and Gerdes and Köberle (2002). As in their studies, Fram Strait sea ice export is highly variable with individual anomalies reaching more than 60% of the mean value e.g. the maxima in winter 1967/68 ($4658 km^3/yr$) and 1988/89 ($4557 km^3/yr$). A few weaker peaks occur in 1958/59, 1980/81, 1992/93 and 1994/95. All peaks in ice export correspond, as discussed in the previous section, with a lag of about two years, to decreases in the Arctic sea ice volume, indicating at least parts of the sea ice volume drops are caused by anomalous Fram Strait export events.

Recent observational estimates indicate substantial Fram Strait export events in the early and late 1980th and in the mid 1990th prior to LS GSAs, e.g. the observed Fram Strait sea ice area flux by Kwok and Rothrock (1999) shows pronounced maxima in the early (1980/81) and late 1980th (1988/89) and the mid 1990th (1994/95).

If one considers the ice covered area between Fram Strait and Denmark Strait as a loose indicator for fresh water volume flux, the findings by Parkinson *et al.* (1999) are consistent to the former results. They also show maxima in the early and late 1980th for Greenland-Island sea ice covered area. Dickson *et al.* (2000) provide a compilation of different Fram Strait ice volume flux estimates for the period 1976-1998. A comparison to the simulation is shown in Fig. 6.7. The different observational estimates show a pronounced maximum around winter 1994/95. This maximum is captured by the simulation. However, the simulation exhibits a second, weaker maximum in 1992/93, that is not present in the observational estimates. Prior to 1991 are only a few estimates available. The estimate by Dickson *et al.* (2000) shows a weak maximum in the late 1980th. Again the simulation is consistent, although the model predicts a much stronger export. Schmith and Hansen (2003) provide a reconstructed time series of Fram Strait sea ice export going back to 1800. For the period 1950-2000 they show 3 major export events, all consistent with this simulation.

The liquid fresh water transport in the East Greenland Current (EGC) (calculated with respect to a reference salinity of 34.8) is $983 \pm 373 km^3/yr$, e.g. the sea ice export event in 1967/68 is accompanied by a weaker liquid fresh water anomaly of about $400 km^3/yr$ in the early to mid 1970th. Whereas sea ice exports have sharp, isolated peaks, liquid export vary more slowly over several years up to decades. A more detailed discussion on the Arctic fresh water budget is given in a following section.

Fig. 6.8 shows spectra of normalized, anomalous Fram Strait sea ice export from the forced and the coupled experiments and from a 180 year reconstruction of Fram Strait sea ice export by Schmith and Hansen (2003). All three spectra show a similar weak peak in the frequency band between 8-10 years. All time series show that export events are non symmetricly distributed around the mean value. The large positive export events do not have a counter part. The NCEP/NCAR period seems to exhibit a rather typical distribution of the events, compared to the coupled run and the reconstruction.

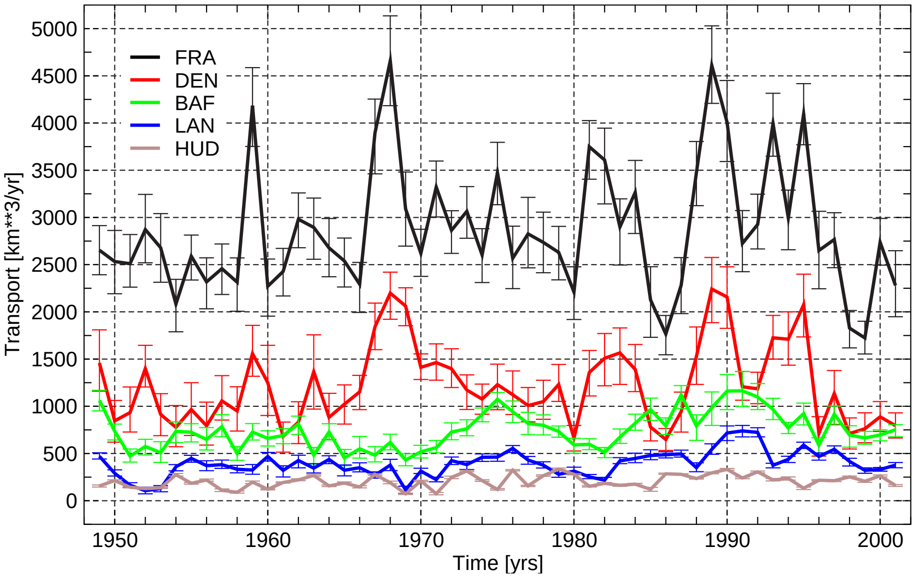

Fig. 6.6: *Ensemble mean volume transports by solid sea ice and snow (winter mean Aug.-Jul.) through Fram Strait (black), Denmark Strait (red), Baffin Bay (green), Lancaster Sound (blue) and Hudson Bay (brown). Error bars indicate the ensemble range. Units are [km^3/yr].*

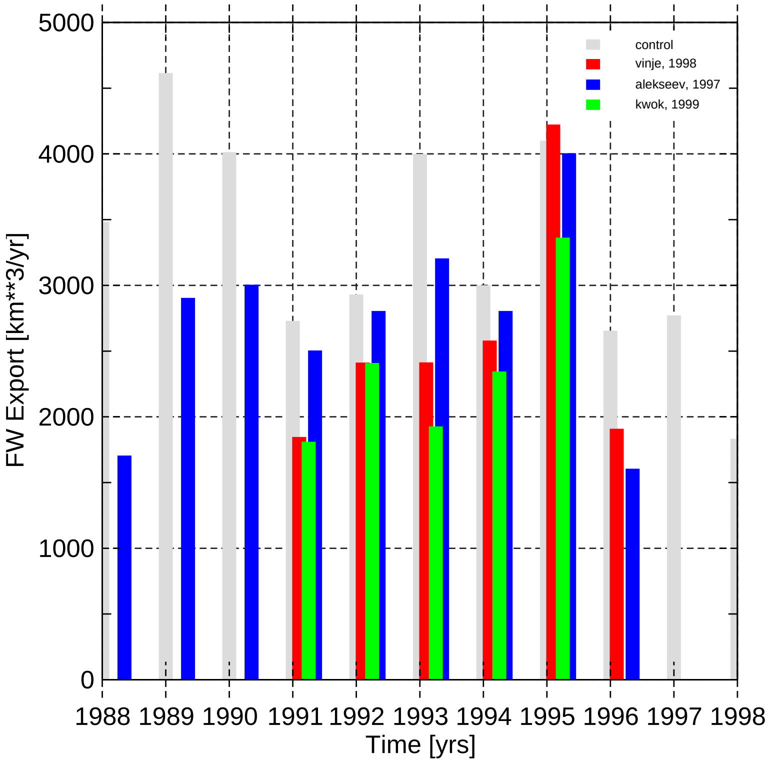

Fig. 6.7: *Fram Strait sea ice export from the simulation (grey) and from several observational estimates. Units are km^3/yr.*

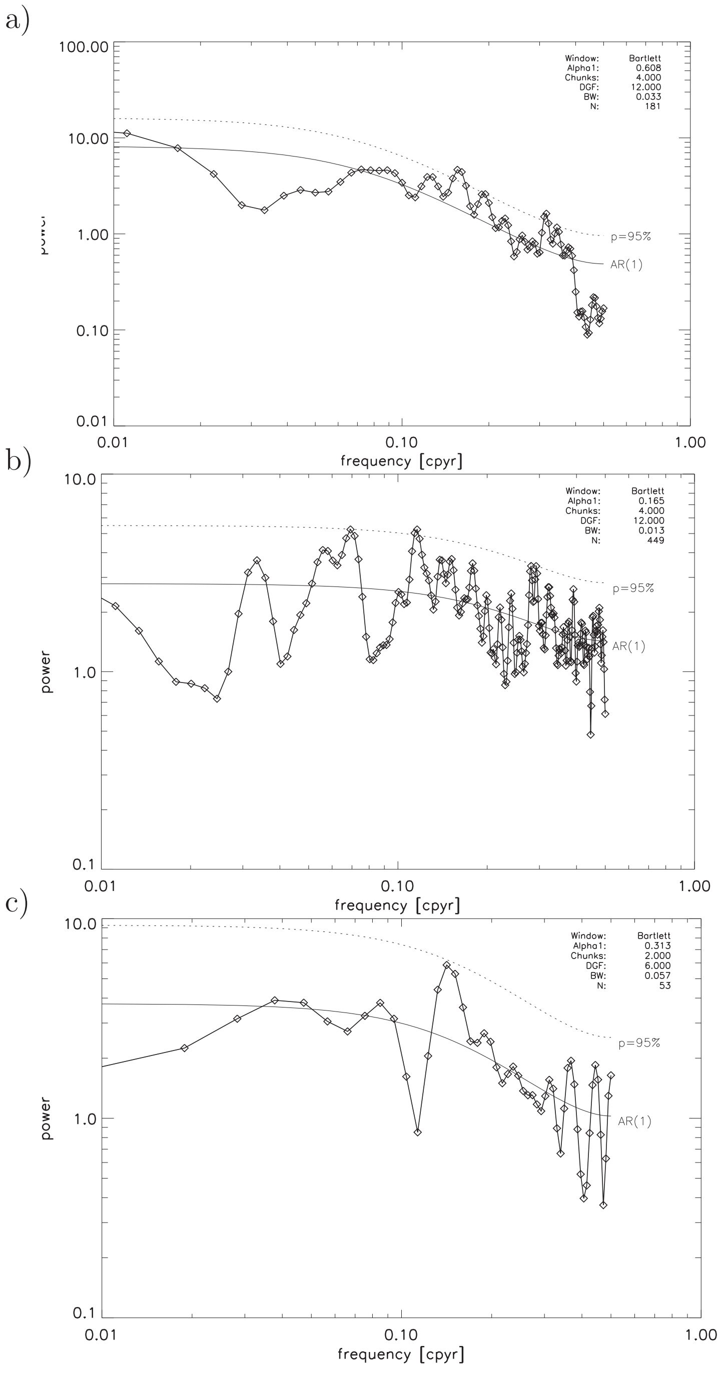

Fig. 6.8: *Power spectra of Fram Strait sea ice export from the forced (a) and the coupled (b) simulation as well as from reconstruction (c).*

6.3.1 Sensitivity Experiments

The sensitivity experiment HPF Q+FW show clearly that the sea ice export in Fram Strait is primarily driven by low-frequency variability in the wind forcing throughout the analyzed period (Fig. 6.9). All major export events from the control integration can be reproduced in the experiment with the hp-filtered thermal and fresh water forcing. The complementary experiment with hp-filtered wind variability fails to reproduce the control integration. Fig. 6.10 shows a lagged regression of Fram Strait sea ice export on NCAR/NCEP sea level pressure and wind stress anomaly (annual means centered on Winter). The wind pattern changes from anti-cyclonic conditions two years prior to large export events to cyclonic conditions during the export events. At a lag of -2 years an anomalous positive SLP anomaly of up to 40 Pa occurs over the central and eastern Arctic domain. The associated wind stress anomalies induce a westward sea ice drift towards the Laptev Sea. Over the Laptev Sea the associated sea ice drift anomaly is rather small, resulting in a convergence of sea ice in this region (e.g. compare Fig. 6.15). At the same time the associated anomalous transports through Fram Strait are weaker than normal and sea ice cover in the Barents Sea is above normal conditions. The last section revealed that the inter-annual variability of the wind stress forcing is producing sea ice thickness anomalies in the East Siberian Sector of the Arctic appr. 2 years before large export events (Fig. 6.4). At a lag of zero years the situation is almost reversed with a negative SLP anomaly of appr. -150 Pa over central and eastern Arctic. The associated cyclonic wind field induces sea ice transport anomalies with a transpolar component at the North Pole and southward component over Fram Strait. The results indicate that the wind forcing is therefore governing the Fram Strait sea ice export by producing ice thickness and ice drift velocities anomalies.

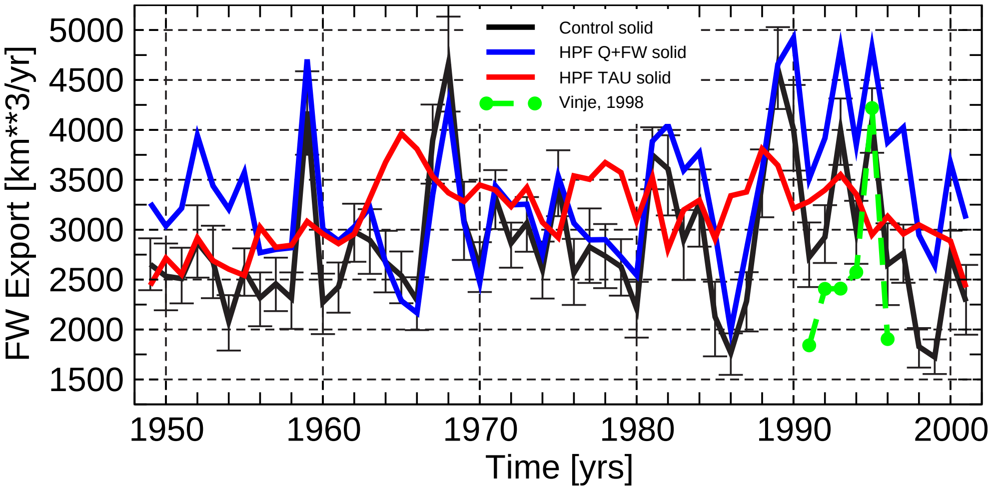

Fig. 6.9: *Fram Strait sea ice export from control run (ensemble annual mean, solid black, thin dashed lines indicate the ensemble range) and the sensitivity runs HPF Q+FW (solid blue) and HPF TAU (solid red) and observations (dashed green). Units are* km^3/yr.

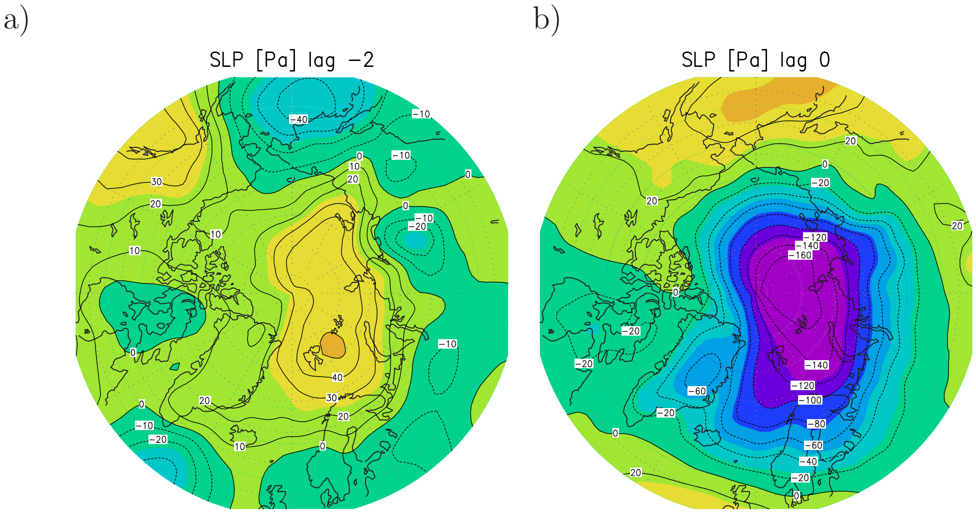

Fig. 6.10: *Regression of Fram Strait sea ice export on annual mean SLP anomalies (Aug.-Jul.) for lags -2 and 0 years. Units are [Pa].*

6.4 Planetary Waves and Fram Strait Fresh Water Export

Hilmer and Jung (2000) showed that Fram Strait sea ice export correlates well with the North Atlantic Oscillation after the mid 1970th. However, the high correlation does not hold for the full NCAR/NCEP period, suggesting an unstable link between Fram Strait sea ice export and the NAO. Recently (Cavalieri and Häkkinen, 2001) and (Cavalieri, 2002) showed a stable relationship between the variability of sea ice export through Fram Strait and the phase of the first zonal planetary wave (wave-1) of SLP (meridionally averaged between 70-80°N). This connection holds for the full NCAR/NCEP period. The shift in the phase of the first planetary wave is to a large part associated with variability of the zonal extent of the Siberian High. Fig. 6.11 shows January monthly means for Fram Strait sea ice export and zonal wave-1 phase of SLP. The correlation of both time series exceeds 0.6 considering the full period 1948 - 2002. For DJF, JFM or annual winter centered means the correlation is slightly weaker, but is still around 0.5 (not shown). The largest outliers that prevent a higher correlation are Januarys of 1968 and 1989 with extreme sea ice exports (associated with the 70th and 90th GSAs) but just average wave-1 phase values. In January 1967 there is an extreme eastward shift in the phase and just average sea ice export. During these periods the anomalous wave-1 phase leads the sea ice export by one year, while for the remaining time the two properties covary with zero lag.

In general enhanced correlations (above 0.4) can be found between January and April, with highest values in January (0.61), and in August (0.44). For the rest of the year correlations are much weaker. Transport through the CAA are anti-correlated with the wave index,e.g. the wind field associated with the high wave-1 phase has a northward flow over the CAA with weaker than average ice export.

The inter-annual variability of the wave1 phase index seems related to the cyclonic/anti-cyclonic circulation regimes proposed by Proshutinsky *et al.* (2002). For high wave-1 phase periods the Arctic atmospheric circulation is in the cyclonic regime inducing a weaker than average Beaufort Gyre circulation and an enhanced Fram Strait sea ice export, and vice versa for the low wave-1 phase.

Composite maps of mean sea level pressure with respect to high and low values of the zonal wave-1 phase show a turning of the local winds over Fram Strait by appr. 90 deg. from northerly parallel towards westward perpendicular direction (Fig. 6.13). This turning is induced by a large scale shift in the atmospheric mass distribution. During the high wave1 phase the Canadian high pressure ridge extents into the Canadian Basin, while the Siberian High shows just a weak north-eastward extent. The Islandic low

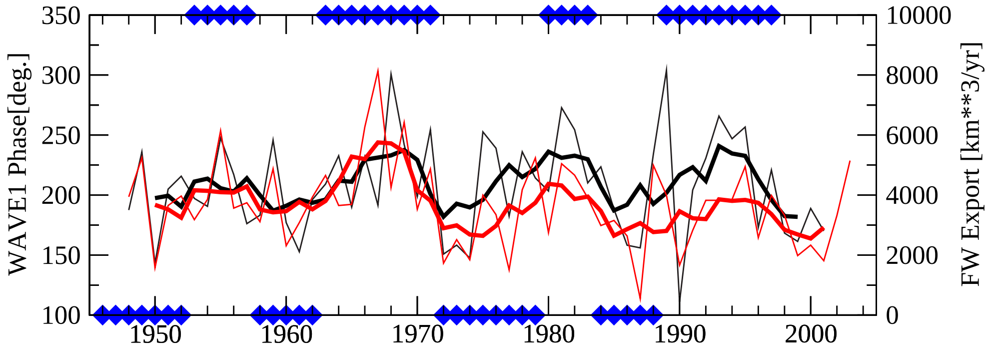

Fig. 6.11: *Fram Strait fresh water export by solid sea ice (black) and phase of zonal wave-1 averaged between 70-80°N (red) for January. Thick lines are smoothed by a 5 year running average. Blue squares indicate the cyclonic (top)/anti-cyclonic(bottom) regimes by Proshutinsky* et al. *(2002). Units are [km^3/yr] and [deg. longitude], respectively.*

pressure trough extents far into the Barents and Kara Seas. During the low wave1 phase the Canadian High pressure ridge is retreated southward, while the Siberian High has a pronounced north-eastward extent, spanning Kara, Laptev and East Siberian Seas. The Islanic Low is deeper, but restricted to the North Atlantic/GIN Sea region, while there are southward winds over the CAA.

Associated sea ice transport anomalies are shown in Fig. 6.14. For the high wave1 phase sea ice export through Fram Strait is enhanched due to northerly winds. Under the influence of the Siberian High pressure ridge a cyclonic circulation anomaly evolves over the East Siberian and Chucki Seas inducing an enchanced transpolar ice drift. CAA transports are weaker due to southerly winds west of Greenland. For the low wave1 phase the situation is reversed. Variability of sea ice transports induced by anomalous wave1 phase shifts is similar to the variability of the seasonal cycle (see Fig. 4.11). Also Proshutinsky and Johnson (1997) associated the two circulation regimes with more prominent summer or winter type atmospheric circulation in respect to the annaul mean. Composits of ocean velocities at 100m depth are shown in Fig. 6.14. Main features are anomalous cyclonic (high phase) and anti-cyclonic (low phase) circulation anomalies in the order of severeal cms^{-1} in the region of the Beaufort Gyre. Associated is a change in sealevel and fresh water contents as suggested by Proshutinsky *et al.* (2002) (see next chapter).

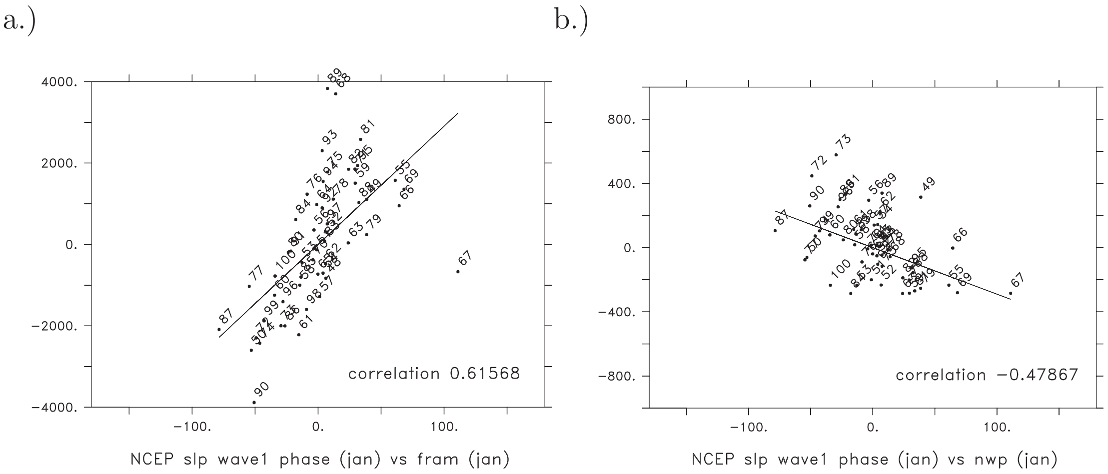

Fig. 6.12: *Scatter plots of January Fram Strait (a) and Canadian Archipelago (b) sea ice export anomalies (ordinate) for the year 1948-2001 versus wave-1 phase anomalies (abscissae). Units are [km^3/yr] and [deg.longitude], respectively.*

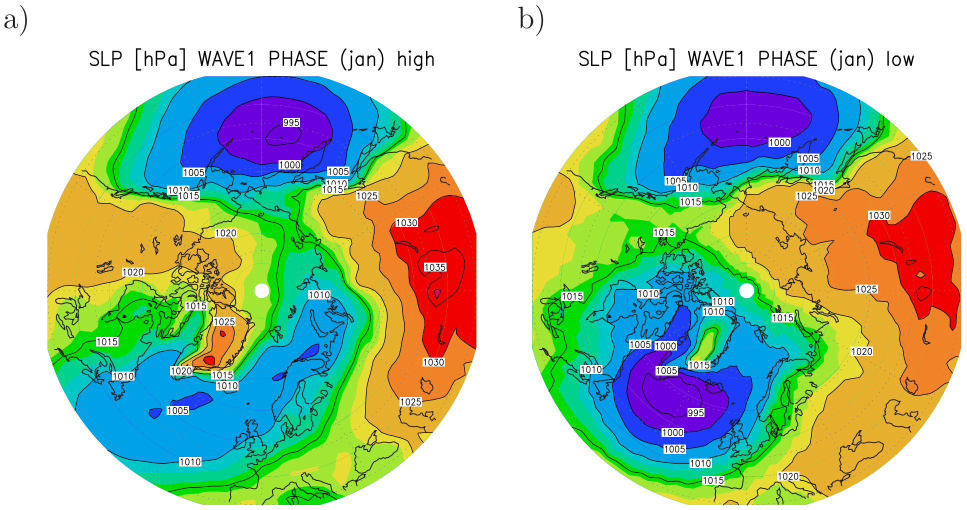

Fig. 6.13: *Composite maps of January SLP for wave-1 phase larger mean + 1 standard deviation (a), and mean less then mean minus 1 standard deviation (b). Units are [hPa].*

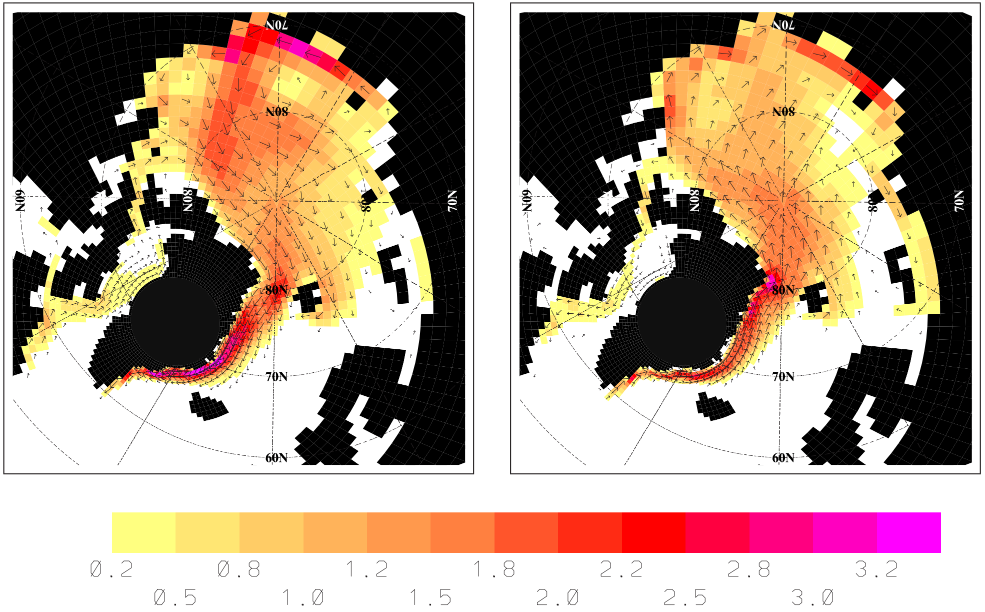

a) High wave-1 phase

b) Low wave-1 phase

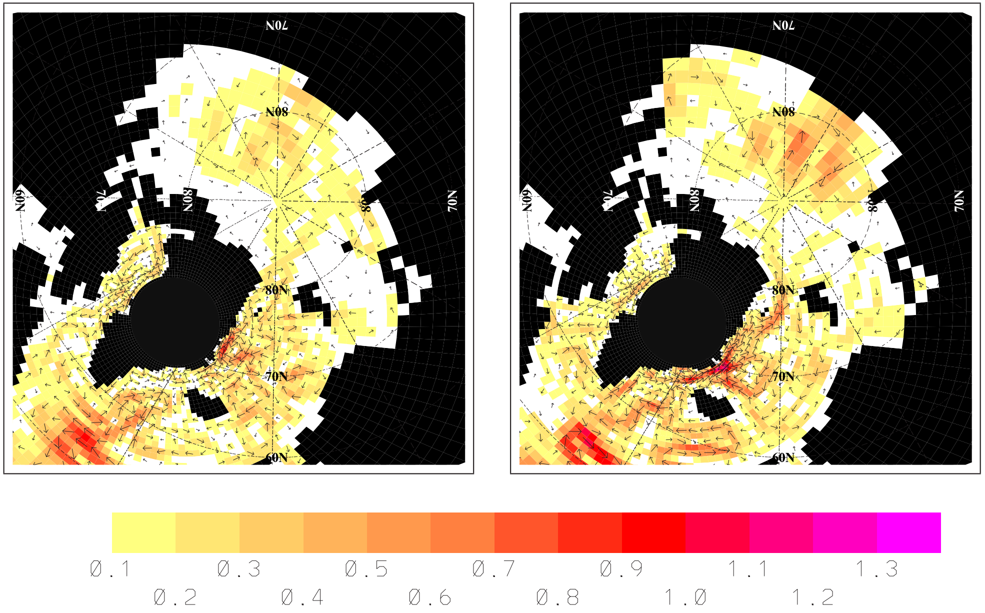

c) High wave-1 phase

d) Low wave-1 phase

Fig. 6.14: *Composite maps of annual mean sea ice transport and ocean velocity (100m) anomalies for wave-1 phase larger mean + 1 standard deviation (a,c), and mean less then mean minus 1 standard deviation (b,d). All values are annual means (Aug.-Jul.). Units are [$dm^2 s^{-1}$] and [cms^{-1}], respectively.*

6.5 Formation and Propagation of Great Salinity Anomalies

Fig. 6.15 illustrates the formation and propagation of the mid 1960th sea ice thickness anomaly that leads to the large Fram Strait ice export event of 1967/68. Anomalous winds lead to an anomalous convergence of sea ice transports in the Laptev Sea in 1965/66. This convergence forms an initial sea ice thickness anomaly of about 1m. The anomaly propagates during the following year across the North Pole into the Canadian Sector and flushes in winter 1967/68 via Fram Strait into the Nordic Seas accompanied by above normal sea ice conditions in th Barents Sea. Transport anomalies via the Canadian Archipelago and from Hudson Bay are slightly negative during this period (Fig. 6.6). A comparison of the mid 1960th event with the other two periods of considerable sea ice exports reveals a close correspondence between all three (Fig. 6.15, 6.16 and 6.17). However, there are also some differences. First, the early 1980th event takes place in a period with less Arctic sea ice volume and thickness in respect to the mid 1960th and end 1980th events (see Fig. 6.1). Furthermore, the early 1980th Fram Strait export anomaly is slightly smaller than the other two. The initial thickness anomaly is formed much closer to the North Pole, and consequently the major part of the fresh water export takes place already one year later in 1980/81 (Fig. 6.16). Transport through the Canadian Archipelago and from Hudson Bay are slightly weaker than their longterm average, consistent to in the mid 1960th event. The late 1980th export event takes place at about the same sea ice volume and thickness level as the mid 1960th event (Fig. 6.17). Again the initial thickness anomaly is formed by convergence of sea ice in the Laptev Sea. However, the Beaufort Gyre has stronger cyclonic circulation component, resulting in above normal Canadian Archipelago transports.

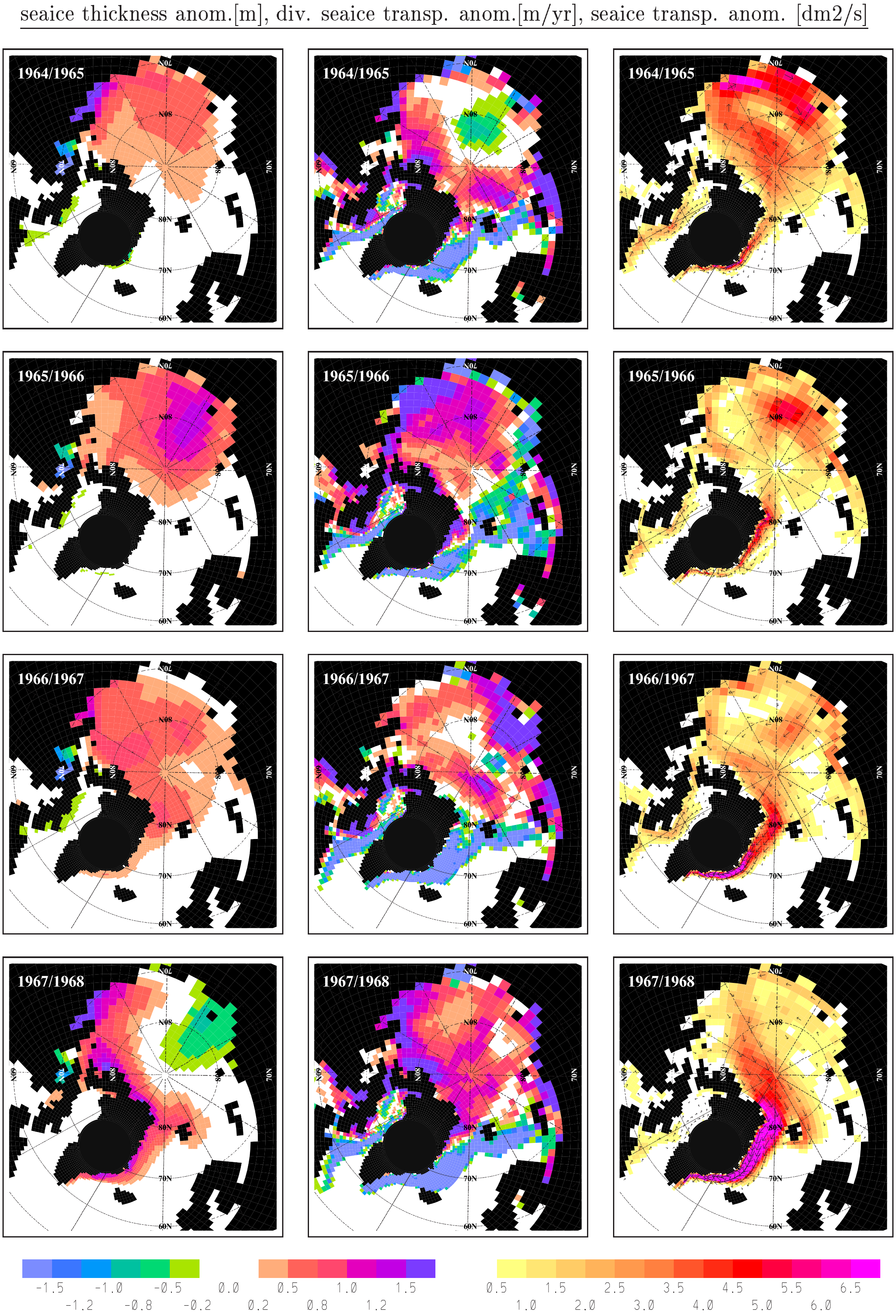

Fig. 6.15: *Ensemble mean sea ice thickness anomaly (left color bar; [m]), sea ice transport divergence anomaly (left color bar; [m/yr]) and sea ice transport anomaly (right color bar; [dm^2/s]) for the years 1965-1969 (winter mean from August to July).*

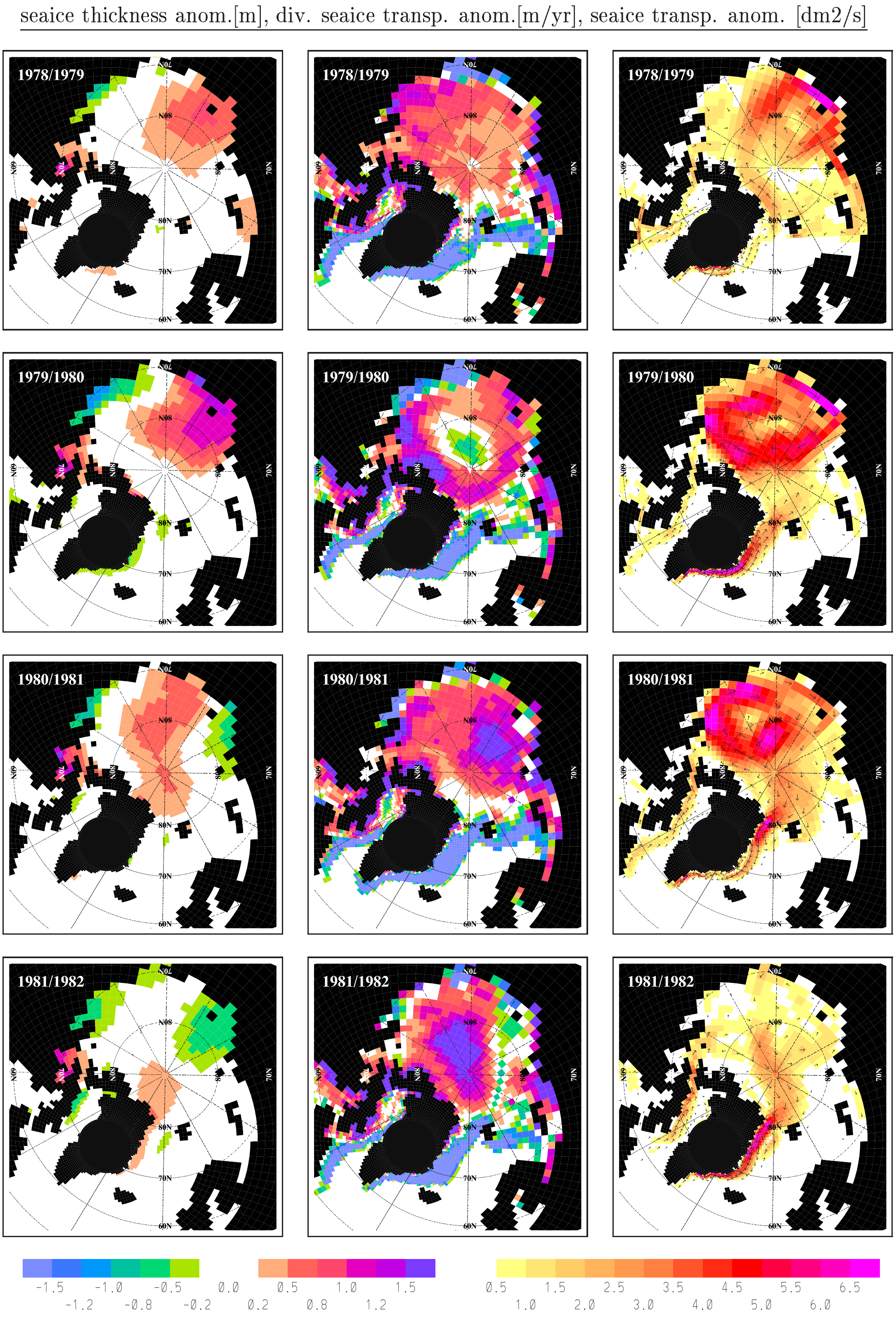

Fig. 6.16: *Ensemble mean sea ice thickness anomaly (left color bar; [m]), sea ice transport divergence anomaly (left color bar; [m/yr]) and sea ice transport anomaly (right color bar; [dm^2/s]) for the years 1979-1982 (winter mean from August to July).*

seaice thickness anom.[m], div. seaice transp. anom.[m/yr], seaice transp. anom. [dm2/s]

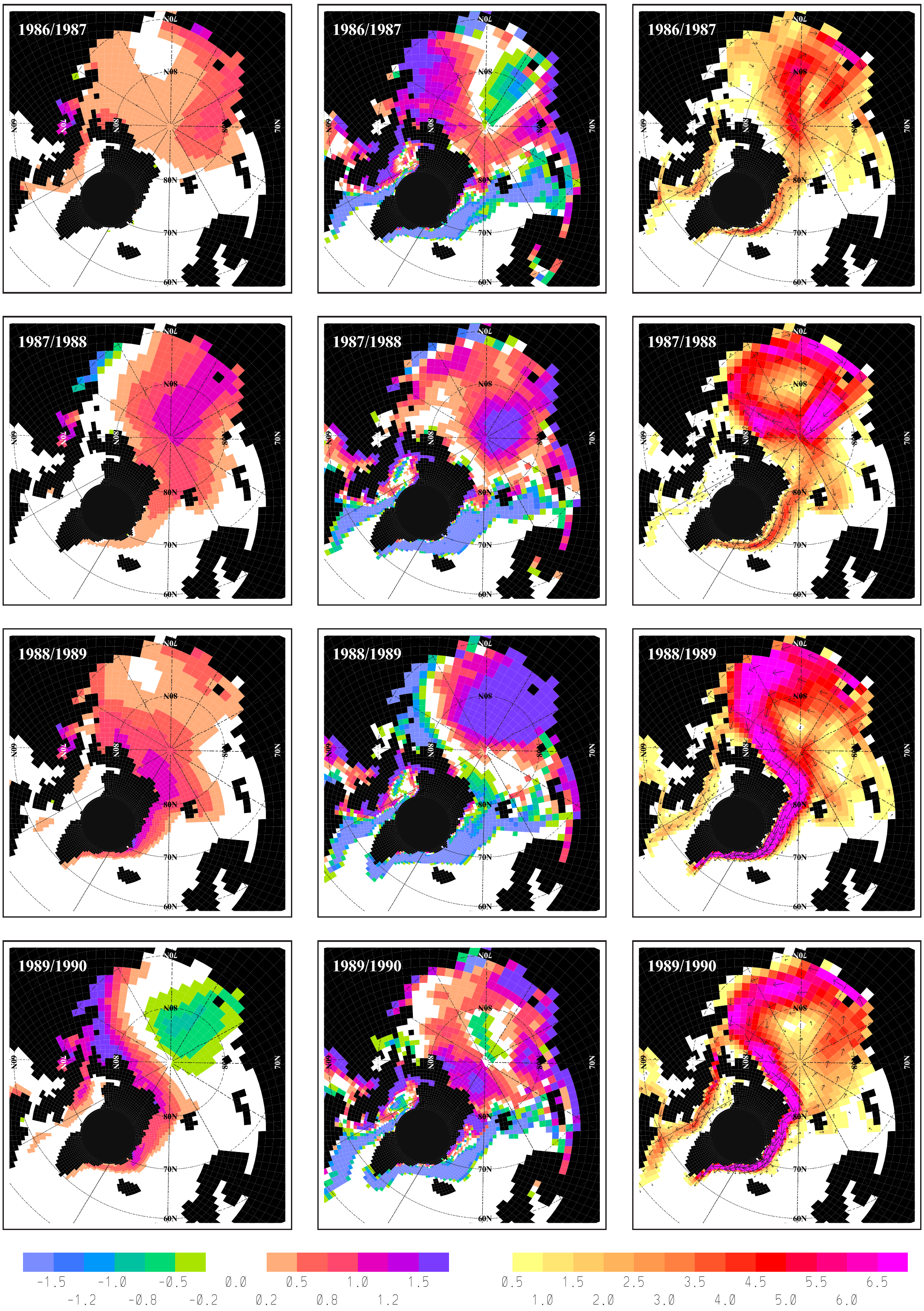

Fig. 6.17: *Ensemble mean sea ice thickness anomaly (left color bar; [m]), sea ice transport divergence anomaly (left color bar; [m/yr]) and sea ice transport anomaly (right color bar; [dm^2/s]) for the years 1987-1990 (winter mean from August to July).*

6.6 Impact of the GSA on the North Atlantic

Sea ice export events immediately influence the upper ocean salinity in the East Greenland Current. Fig 6.18 shows a lag regression of Fram Strait sea ice export onto the salinity anomaly of the upper ocean (0-335 m). Note, that most export events last for two following winters, resulting in lag 0 in the regression analysis based on annual, winter centered values. The regression reveals that average EGC salinity decreases shortly after the ice export event by an amplitude of 0.1 psu per standard deviation of Fram Strait sea ice export, e.g. during the 1967/68 export event the salinity decrease in the EGC locally exceeds -0.25 psu. The low saline water is advected southward around Greenland into the Labrador Sea. One part of the anomaly recirculates in the Subpolar Gyre, while another part enters Newfoundland Basin 3-4 years after the peak in the export event. These anomalies enter the North Atlantic Current and follow the general circulation eastward. However, they vanish before reaching the European basin. This is contrary to the observations by contrary to the observations by Dickson *et al.* (1988). The lifetime of the anomalies in the simulation is probably underestimated due to strong mixing at the subpolar frontal system and the spurious damping effect of the surface salinity relaxation.

The freshening of the Subpolar Gyre after an sea ice export event is associated with a cooling of the upper ocean. Corresponding temperature anomalies in the depth range 0-335 m reach -0.25°C per standard deviation of Fram Strait sea ice export and last for about the same time as the salinity anomalies. Wintertime mixed layer depth in the Subpolar Gyre is strongly reduced during these periods.

Figure 6.19 shows the area-averaged ensemble mean near surface salinity in the central LS and the corresponding observations from Ocean Weather Ship (OWS) Bravo. The salinity decreases shortly after the 1967/68 export event, from 34.7 to 34.3 psu within the following three years. It reaches its minimum in 1971 and recovers afterwards. Around 1974 LS near surface salinity reaches 34.5 again. In both the simulations and the observations, LS deep convection (associated with an increase of surface salinity) reoccurs in winter 1971 and in the following years. The onset of LS deep convection is accompanied by above normal LS sea ice conditions in Davis Strait. This result is consistent with the analysis of Deser *et al.* (2002), who found above normal sea ice in the LS during 1972-74, 1983-85 and 1990-92 in observations. The sensitivity experiments reveal, that severe atmospheric winter conditions over the LS, in particular the thermal+fresh water forcing during positive NAO phases, are driving the deep convection and the sea ice cover anomalies on inter-annual timescale (not shown).

In summary it can be said that the model satisfactorily simulates the observed GSA which occured around 1970 in the LS (Dickson *et al.*, 1988; Lazier, 1995; Belkin *et al.*, 1998). Two additional GSAs are simulated, around 1980 and around 1990, in agreement with Belkin *et al.* (1998) and Häkkinen (2002). Both are less pronounced than the first one, possibly due to an underestimation of the CAA contribution in the simulation. The sensitivity runs reveal that low-frequency variations in the wind stress are sufficient to produce the 1970th GSA of appr. correct size. However, the low surface salinities on the LS persists for a longer time, without the onset of thermally forced deep convection in 1971. The complementary run with the hp-filtered wind stress lacks the export event, and therefore also the GSA. The introduction of an artificial sea ice/fresh water anomaly of $3000km^3$ in 1967/68 into Fram Strait in a climatological forced run (HPF ALL), led to a slightly weaker GSA as in the control run (not shown). Figure 6.19 also shows the strength of the Atlantic THC and the associated heat transport at 30°N.

To assess the impact on the Atlantic THC, the runs HPF ALL with and without artificial GSA are compared. The Atlantic THC is barely affected by the introduction of the sea ice/fresh water anomaly. The difference in volume and heat transport is less than 0.3 Sv (0.05 PW) at 30°N and lasts only for a few years (not shown). The impact of the 1970th GSA seems to be larger in the control run (appr. 1 Sv and 0.1 PW). However, the decrease in THC volume and heat transport is still in the order of one standard deviation of the variability.

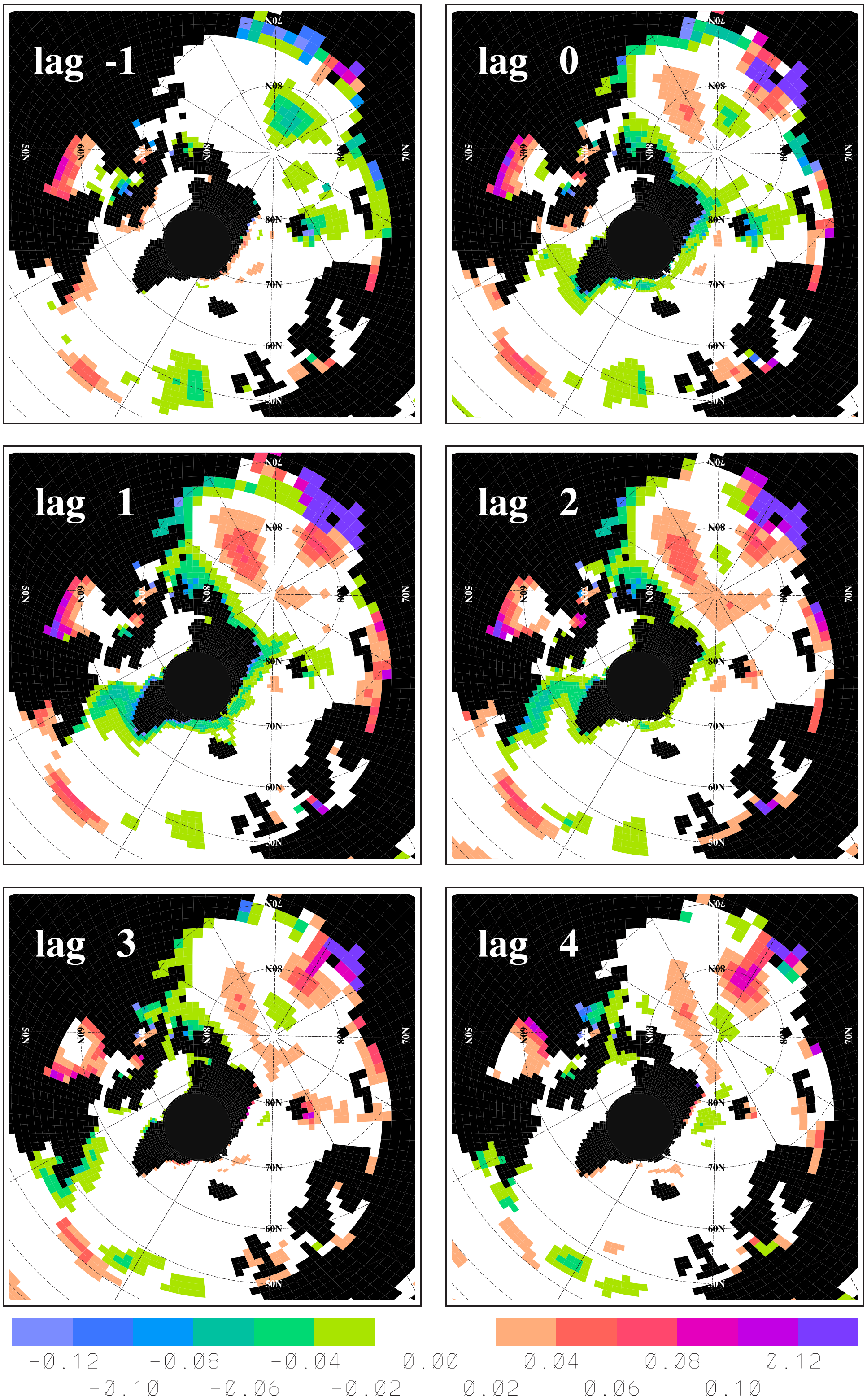

Fig. 6.18: *Regression of annual mean Fram Strait sea ice export on annual mean upper ocean salinity (incl. sea ice and snow) from the control run for different time lags (integer years). Units are δpsu per one standard deviation of Fram Strait sea ice export.*

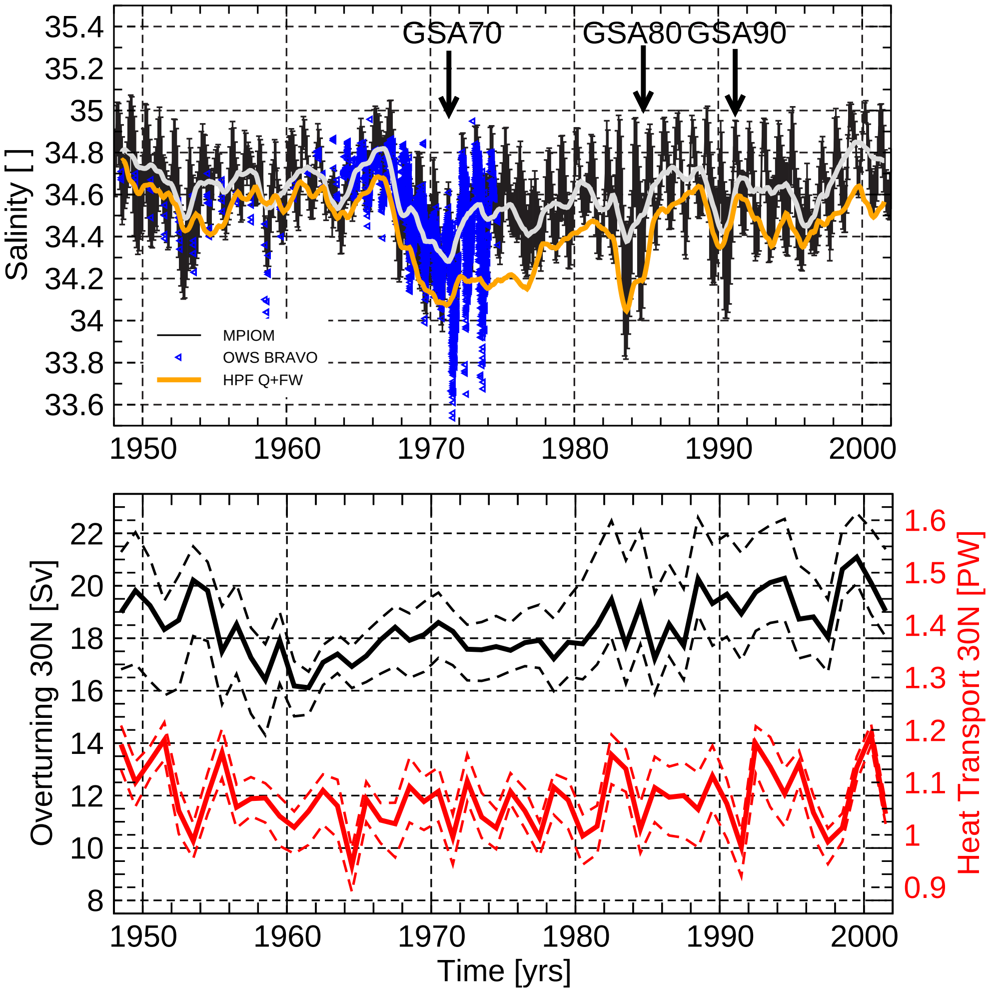

Fig. 6.19: *Upper panel shows Labrador Sea near surface salinity (20-60 m) from control run as monthly mean (ensemble mean, bars indicate the ensemble range; black) and smoothed by a 12 month running mean (gray), sensitivity run HPF Q + FW (orange) and observations from OWS BRAVO (blue triangles). Lower panel shows Atlantic meridional overturning at 30°N (black) and heat transport (red). Thin dashed lines indicate the ensemble range. Units are Sv and PW respectively.*

6.7 Arctic Fresh Water Budget Variability

Fig. 6.20 shows the time evolution of the simulated Arctic fresh water storage due to anomalous sea ice and liquid fresh water and the combination of the two. Arctic fresh water storage exhibits considerable variability on inter-annual to decadal timescales. Solid and liquid anomalies are of comparable amplitude and vary slightly anti-correlated. Exceptions are years shortly after extreme export events, e.g. the late 1960th or late 1980th. The process of brine release during ice build ups and the additional fresh water release during periods of anomalous melting link the solid and liquid fresh water storage. However, extreme export events remove considerable amounts of sea ice from the Arctic domain, and disturb this balance. Liquid fresh water anomalies are stored in the Canandian Basin north of Greenland and in the Beaufort Gyre, while solid anomalies are stored in East Siberian/Laptev sea ice thickness anomalies (Fig. 6.21). Liquid anomalies are calculated in respect to a reference salinity of 34.8. The choice of a reference salinity of 34.0 reveals that fresh water anomalies are indeed stored in the Beaufort Gyre as suggested by Proshutinsky *et al.* (2002) (not shown). However, in respect to a reference salinty of 34.8 the Beaufort Gyre becomes less dominant.

Fig. 6.22 shows the contributions of the individual components to the Arctic fresh water budget variability. The largest contribution to the inter-annual to decadal variability in the Arctic fresh water budget originates in anomalous Fram Strait transports. The solid sea ice part of these transports amounts to appr. 2/3 and the liquid to appr. 1/3 of the total anomalies. Variability in the atmospheric forcing (precipitation, evaporation, runoff and restoring) as well as the variability in the transports through the other passages is considerably smaller. Consequently Arctic fresh water storage covaries in phase with the accumulated Fram Strait exports on inter-annual time scales (Fig. 6.22). Accumulated CAA transports are of comparable size to that through Fram Strait, but vary much slower, more on inter-decadal time scales. Similar slow changes occur in the combined effect of precipitation, evaporation, and restoring of surface salinity in ice free regions. Note, that inter-annual runoff variability is neglected in the study, though it may be of the order of 5-20% of the climalological annual mean of $3300km^3$ (Aagaard and Carmack, 1989). Simulated anomalies in Bering Strait and Barents Shelf fresh water inflow are considerably smaller than the other transports. The simulated Arctic fresh water anomalies show a good agreement to the results by **?**). The authors find the largest contribution to the Arctic fresh water budget in the inflow of saline Atlantic water, contrary to the result found in this simulations. However, consistently to this study they find that fresh water anomalies stored in the Beaufort Gyre seem to have little overall impact on the variability of the Arctic fresh water budget.

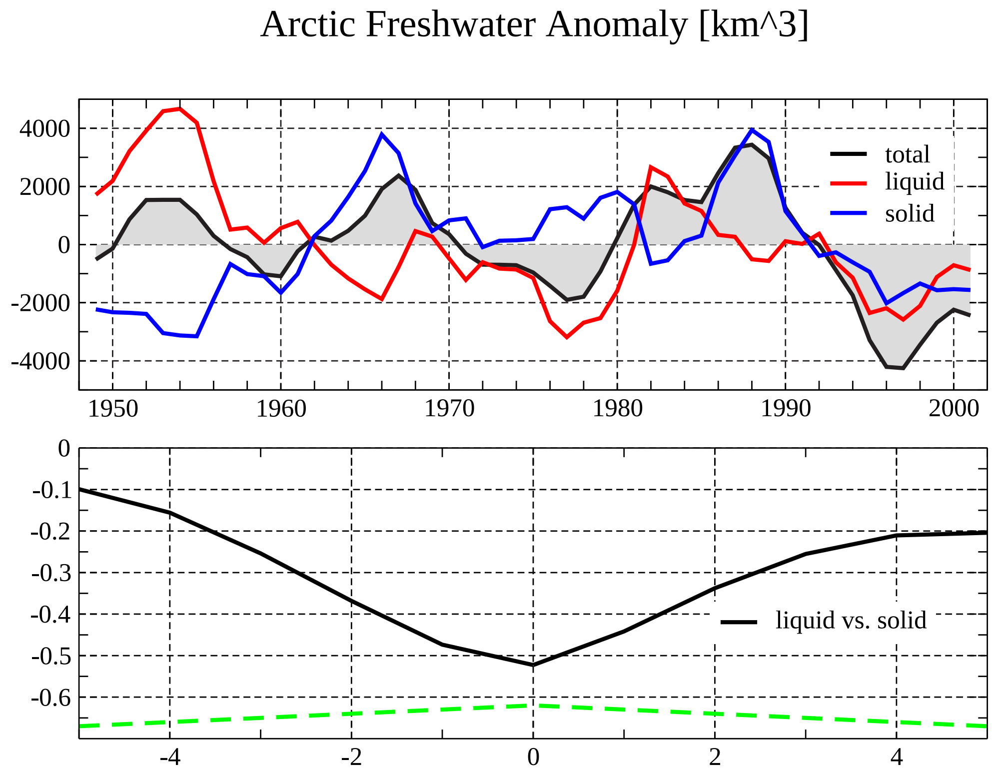

Fig. 6.20: *Upper panel shows time evolution of anomalous Arctic fresh water storage in the entire water column from solid, liquid and both components. All quantities are calculated in respect to reference salinity of 34.8. Units are km*^{3}. *The lower panel shows the correlation coefficient between solid and liquid part (black) for several time lags and the 95% confidence interval.*

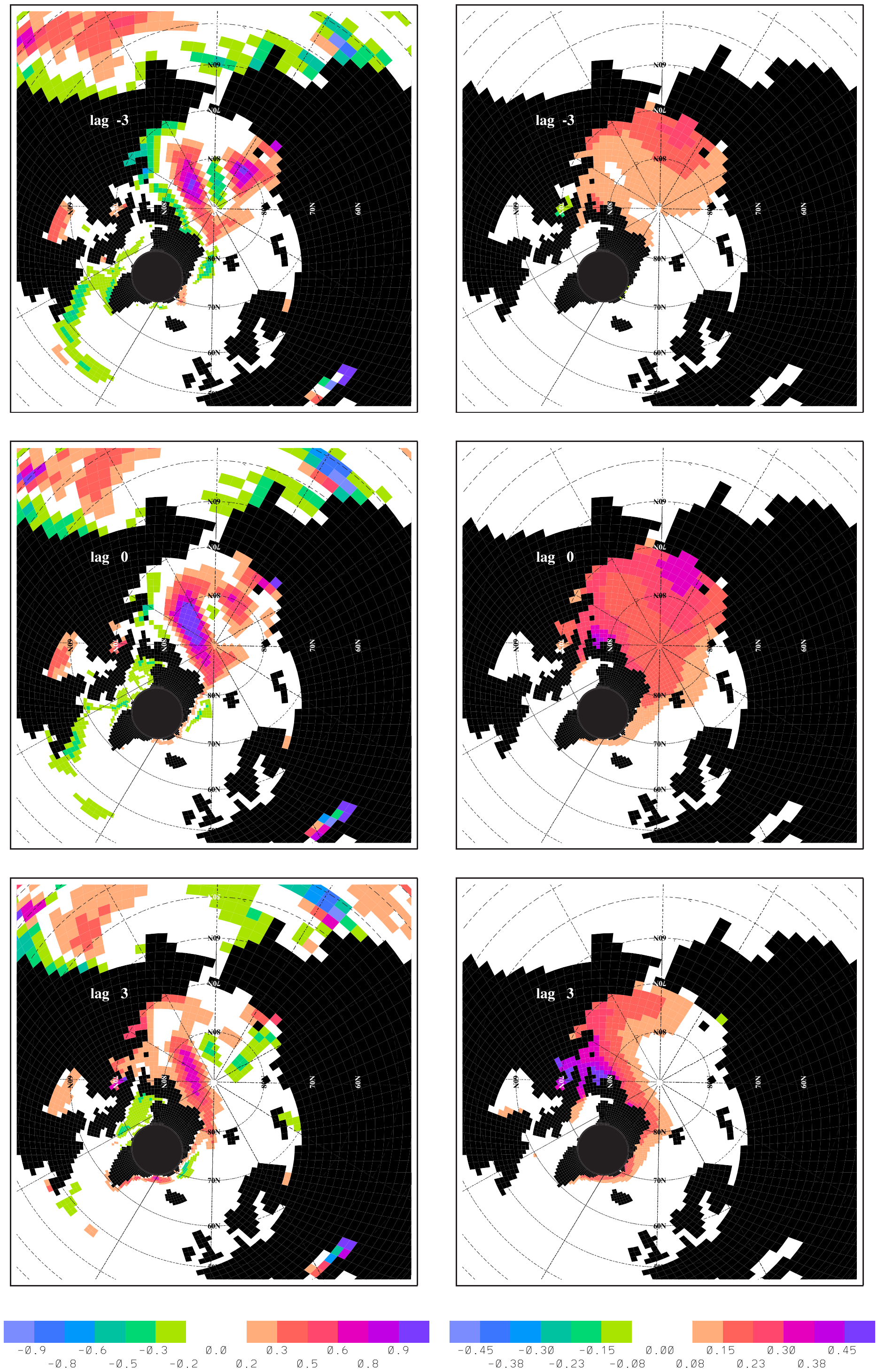

Fig. 6.21: *Lagged regression of liquid (left) and solid (right) basin averaged fresh water anomalies onto the local liquid and solid fresh water content. Quantities are calculated in respect to a reference salinity of 34.8 . Units are m per one standard deviation of liquid (solid) anomalous Arctic fresh water content.*

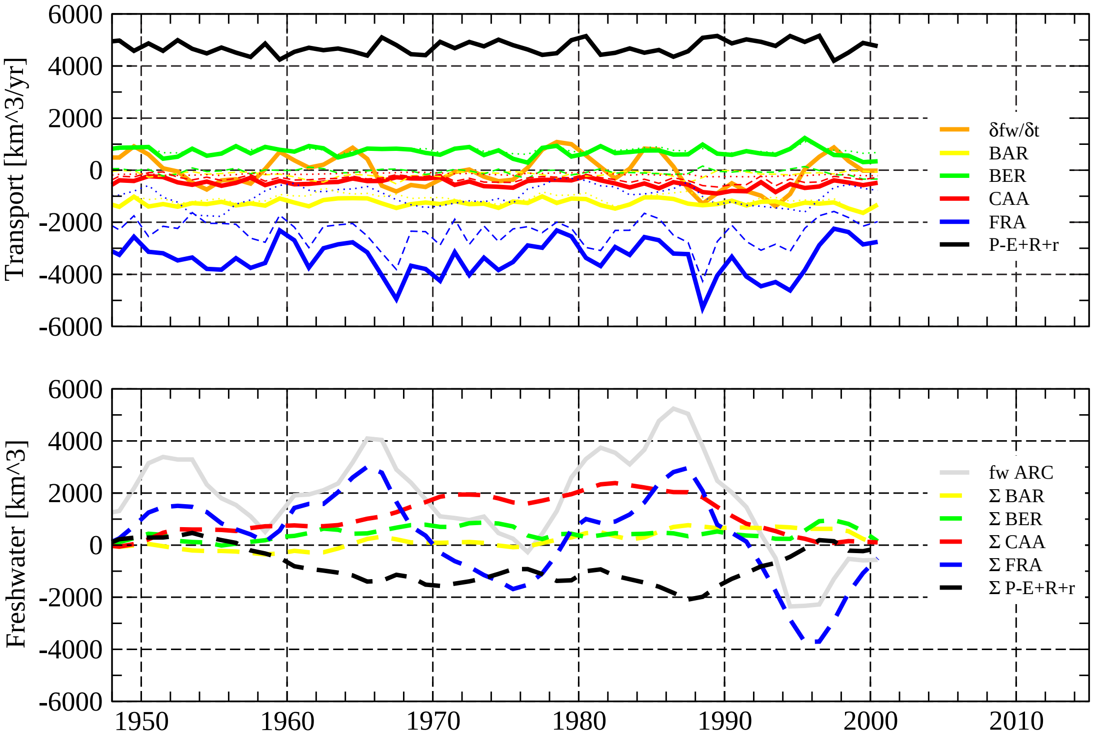

Fig. 6.22: *Upper panel shows Arctic fresh water transports (solid + liquid) through the individual passages (solid fw=dashed, liquid fw =dotted, total fw=thick), the surface fresh water input and the change in fresh water storage (solid + liquid). All quantities are calculated in respect to reference salinity of 34.8. The lower panel shows the time-integrated anomalies of these transports. Units are* km^3/yr *and* km^3*, respectively.*

7. DISCUSSION

Inter-annual to decadal variability of the North Atlantic/Arctic ocean and sea ice is investigated in an ensemble of hindcast simulations for the period 1948-2001 using the ocean/sea ice model MPIOM forced by realistic boundary conditions taken from NCAR/NCEP Reanalysis. This study emphasizes on processes that may affect the Atlantic MOC, e.g. changes in the high latitude deep convection induced by low-frequency shifts in the atmospheric boundary conditions, as well as the interaction between Arctic and North Atlantic ocean via Arctic fresh water exports.

Several properties of the simulated coupled ocean/sea ice system show considerable dependency on the initial conditions, in particular the low frequency variability of the Atlantic MOC. Uncertainty of key quantities with respect to initial conditions is quantified by presenting results in terms of ensemble mean and spread between the ensemble members.

Wintertime deep convection in the Labrador Sea and GIN Sea is found to be weakly anti-correlated during the simulated period. Labrador Sea deep convection is dominated, during the absence of substantial surface salinity anomalies, by inter-annual to decadal variability of the NAO. Also GIN Sea convection follows the low-frequency shifts of the NAO, however the relationship is less strong. Yet the simulations support the existence of a convection seesaw between Labrador Sea and GIN Sea caused by the low-frequency changes in the NAO (Fig. 5.2). The influence of low-frequency variability of the NAO on the LSW properties is clearly visible during the simulation period, in particular the shift in the 1970th (Fig. 5.3, 5.4).

The simulation captures the observed decadal changes in Atlantic water mass structure (e.g. changes in the LSW, Mediteranian Deep Eater and tropical Atlantic surface water properties between the 1950th and 1990th (Fig. 5.5)) and can relate these to changes of the MOC. The results suggests that MOC strength increased during the second half of the last century, mainly caused by the elevated NAO (Fig. 5.11). Results from the coupled model reveal that MOC variability follows NAO variability on inter-annual to decadal timescales. On longer timescales such a relationship is less detectable. However, given the low-frequency trend in the NAO it seems likely that the MOC responds as suggested in this study. Changes in the MOC manifest themself in various dynamical properties, e.g. the North Atlantic Subtropical Gyre, in particular the Gulf Stream/NAC, path and strength

(Fig. 5.8). The Deep Western Boundary Current strength increases due to elevated LSW production, while the overflows from the Nordic Seas where found to weaken by appr. 30%, possibly caused by reduced GIN Sea convection after 1970 (Fig. 5.6, 5.7 and 5.8). However, the simulation fails to reproduce the observed freshening trend of the overflows reported by Hansen *et al.* (2001).

The model captures the observed variability of Arctic sea ice covered area (Fig. 6.2). Simulated changes in the Arctic sea ice volume are found to be caused by sea ice thickness changes, driven in equal parts dynamically and thermodynamically (Fig. 6.4). Arctic sea ice volume decreases after 1980 by appr. 30%, however the trend cancels if the full simulation period is considered.

The model is able to reproduce the chain of processes that led to the formation and propagation of Labrador Sea GSAs observed in the 1970th, 1980th and 1990th. All GSAs are remotely driven by above normal fresh water exports via Fram Strait that have their origin in anomalous Arctic sea ice properties. Figures 6.15, 6.16 and 6.17 show that anomalous winds lead to a convergence of sea ice transports in the East Siberian and Laptev Seas. The resulting positive sea ice thickness anomaly propagates across the North Pole and via Fram Strait into the North Atlantic. Fram Strait ice export variability is primarily forced by low-frequency variations in the winds. In particular, it is associated with variability of the phase of the first zonal planetary wave between 70-80°N, as reported by Cavalieri and Häkkinen (2001) and can be associated with the position and strength of the Siberian and Canadian Highs and Islandic and Aleutian Lows. While moderate Fram Strait sea ice exports and wave-1 phase covary in phase with zero lag, extreme events like the ones associated with the GSAs exhibit a lag of one year. Once a sea ice anomaly of appropriate size enters Fram Strait, a GSA will occur in the LS, consistent with previous results of Häkkinen (1999) for an idealized GSA. The simulated sea ice exports through the Canadian Arctic Archipelago (CAA) and the local fresh water forcing have only minor importance in exciting GSAs, with the exception of the GSA90. Simulated CAA fresh water transports (solid + liquid) anomalies are smaller than those from Fram Strait (in the order of 20-30% of the Fram Strait values). In the simulation, the transports by the CAA and Fram Strait have the tendency to be anti-correlated. The large Fram Strait export events from 1967/68 and 1988/89 are accompanied by relatively weak transports through the CAA, likely linked to the phase of the first zonal planetary wave (Fig. 6.12, 6.13 and 6.14). Only for the GSA90 export event both transports are positive and contribute to the LS GSA (with CAA fresh water transports reaching 50% of the Denmark Straits fresh water transport. During this period an extreme shift in the phase of wave-1 occurs, e.g. 1989 has extreme high values (eastward position) and 1988 and 1990 have extreme low values (westward position). Consistently Fram Strait exports peak in winter 1989 and 1990, while CAA transports have their maximum in winters 1990 to 1992. The forward and backward shift in wave-1 phase might enable contributions to LS GSA90 from both sources - Fram Strait and CAA. However, the model's horizontal resolution does not allow a proper representation of the Canadian Archipelago through-flow, and so some caution is advised in considering the result. There is the possibility of local amplification of the remotely advected low salinity anomalies, once the wintertime deep convection in the LS is weakened or even shut-down, as discussed in Houghton and Visbek (2002). Vertical mixing by wintertime deep convection and hence the local atmospheric forcing over the LS plays an important role in removing the low surface salinities again. In particular, the NAO is driving central LS deep convection and Davis Strait sea ice conditions. As such, the simulation is consistent with the results of Curry *et al.* (1998) and Deser *et al.* (2002). It can be concluded that the local wintertime atmospheric forcing (in particular the thermal and fresh water part) is setting the timescale of the LS surface salinity recovery to it's climatological value. A part of each salinity anomaly leaves the subpolar gyre to the south and can be tracked to the Newfoundland Basin. The simulated anomalies enter the North Atlantic Current, but vanish before reaching the European Basin, contrary to the observations by Dickson *et al.* (1988). The life time of the anomalies in the simulation is probably underestimated due to strong mixing at the subpolar frontal system and the spurious damping effect of the surface salinity relaxation.

Finally, the simulation reveals no strong impact of a single export event on the strength of the North Atlantic THC, contrary to the results of Häkkinen (1999). The LS sinking region is affected only for a few years by the low salinities. An impact on the North Atlantic THC would largely depend on the frequency at which these export events occur, as well as the recovery time of the surface salinity, which is strongly influenced by the local atmospheric forcing.

Arctic fresh water storage exhibits considerable variability on inter-annual timescales with peak to peak variations of up to 7000 km^3 (Fig. 6.20). Simulated variability shows a close correspondence to recent model results by Häkkinen and Proshutinsky (2004). Both solid and liquid fresh water anomalies contribute to this variability in equal parts. Most of the time both are anti-correlated except during and shortly after extreme export events due to the process of brine release associated with melting/freezing events. While solid fresh water is mainly stored in sea ice thickness anomalies that originate in the East Siberian and Laptev Seas the liquid fresh water anomalies are mainly stored in the Beaufort Gyre and the Canadian Basin north of Greenland. In this study, the anomalous Arctic fresh water storage is clearly dominated by inter-annual variability of fresh water export via Fram Strait. This result is somewhat different to the model studies by Häkkinen and Proshutinsky (2004) in which the largest contribution to anomalous Arctic fresh water storage is found in Atlantic water inflow via the Barents Sea. Simulated Fram Strait sea ice exports are closely related to inter-annual atmospheric circulation anomalies, e.g. Fig. 6.11 shows the close relationship of low-frequency shifts in wave-1 phase and Fram Strait sea ice exports. Furthermore, a response of the Beaufort Gyre strength is found. The inter-annual variability of zonal planetary wave-1 phase or the related cyclonic/anti-cyclonic circulation regimes proposed by Proshutinsky and Johnson (1997) influence the Arctic fresh water budget by modifying Fram Strait sea ice export. Fresh Water export via Fram Strait shows an increasing trend, while Arctic fresh water storage shows a decreasing trend during the simulated period. Possibly this trend contributes to the observed freshening in the subpolar North Atlantic, as reported by Curry *et al.* (2003). The simulation suggests that many aspects of observed North Atlantic low-frequency variability can be attributed to atmospheric variability, e.g. NAO or the zonal planetary waves. Experiments with a forced ocean/sea ice model are of course limited due to the lack of a feedback from the ocean/sea ice system to the atmosphere. Yet the hindcast simulations allowed some additional insight into observed variability, like the formation of the GSAs or the changes in the LSW and its relation to changes in the MOC.

Coupled Atmosphere Ocean General Circulation Model studies will allow further investigation of the nature of the Arctic atmospheric variability that seems to control large parts of the Arctic/North Atlantic interaction. Most studies in the literature put their emphasis on NAO/AO variability. The variability of the Siberian and Canadian High (in particular their position and northward extend as well as their interplay with the Islandic Low) seems to be another important factor driving Arctic/North Atlantic exchanges.

8. APPENDIX

Symbol	Description	Value
α_{if}	freezing sea-ice albedo	0.75
α_{im}	melting sea-ice albedo	0.70
α_{sf}	freezing snow albedo	0.85
α_{sm}	melting snow albedo	0.70
α_w	sea water albedo	0.10
λ	wind mixing stability parameter	0.03 kg m^{-3}
ε	emissivity of sea water	0.97
ρ_a	density of air	1.3 kg m^{-3}
ρ_i	density of sea-ice	910 kg m^{-3}
ρ_s	density of snow	330 kg m^{-3}
ρ_w	density of sea water	1025 kg m^{-3}
σ	Stefan-Boltzmann constant	5.5×10^{-8} W m^{-2} K^{-4}
Λ_V	eddy viscosity relaxation coefficient	0.6
Λ_D	eddy diffusivity relaxation coefficient	0.6
c_a	specific heat capacity of air	1004 J kg^{-1} K^{-1}
c_w	specific heat capacity of sea water	4.0×10^3 J kg^{-1} K^{-1}
e	ratio of principle axis of yield ellipse	2.0
g	acceleration due to gravity	9.81 m s^{-2}
k_i	thermal conductivity of sea ice	2.17 W m^{-1} K^{-1}
k_s	thermal conductivity of snow	0.31 W m^{-1} K^{-1}
z_0	wind mixing penetration depth	40 m
A_b	PP background vertical viscosity	1.0×10^{-4} m^2 s^{-1}
A_w	PP wind mixing	5.0×10^{-4} m^2 s^{-1}
A_{VO}	PP vertical viscosity parameter	1.0×10^{-2} m^2 s^{-1}
B_H	biharmonic horizontal viscosity	1.1×10^{-6} s^{-1} $\times$ $(\Delta x^4, \Delta y^4)$
BBL_{max}	maximum BBL thickness	500 m
C	empirical internal ice pressure const.	20
C_{RA}	PP viscosity tuning constant	5.0
C_{RD}	PP diffusivity tuning constant	5.0
C_W	ocean-ice stress bulk transfer	0.0045
D_b	PP background vertical diffusivity	1.0×10^{-5} m^2 s^{-1}
D_H	harmonic horizontal diffusion	2.5×10^{-3} m s^{-1} $\times$ $(\Delta x, \Delta y)$
D_w	PP wind mixing	5.0×10^{-4} m^2 s^{-1}
D_{VO}	PP vertical diffusivity parameter	1.0×10^{-2} m^2 s^{-1}
L_f	latent heat of fusion	2.5×10^6 J kg^{-1}
L_s	latent heat of sublimation	2.834×10^6 J kg^{-1}
L_v	latent heat of vaporisation	2.5×10^6 J kg^{-1}
P^*	empirical internal ice pressure const.	5000 N m^{-1}
S_{ice}	salinity of sea-ice	5 psu
T_{freeze}	freezing temperature of sea water	-1.9°C
T_{melt}	melting temperature of sea ice/snow	0°C
W_T	wind mixing amplitude parameter	5.0×10^{-4} m^2 s^{-1}

Tab. 8.1: Constants and parameters used in the ocean/sea ice model.

BIBLIOGRAPHY

Aagaard, K. and E. Carmack, 1989. The role of sea ice and other fresh water in the Artic circulation. *J. Geophys. Res.*, **94**, 14485–14498.

Bacon, S., W. Gould and Y. Jia, 2003. Open-ocean convection in the Irminger Sea. *Geophys. Res. Lett.*, **30**, doi:10.1029/2002GL016271.

Bader, J. and M. Latif, 2003. The impact of decadal-scale Indian Ocean sea surface temperature anomalies on Sahelian rainfall and the North Atlantic Oscillation. *Geophys. Res. Lett.*, **30**, doi:10.1029/2003GL018426.

Beckmann, A. and R. Döscher, 1997. A method for improved representation of dense water spreading over topography in geopotential-coordinate models. *J. Phys. Oceanogr.*, **27**, 581–591.

Belkin, I. M., S. Levitus and J. Antonov, 1998. Great salinity anomalies in the North Atlantic. *Prog. Oceanogr.*, **41**, 1–68.

Berliand, M. E. and T. G. Berliand, 1952. Determining the net long-wave radiation of the earth with consideration of the effects of cloudiness. Isv. Akad. Nauk. SSSR Ser. Geofis. 1.

Bjerkness, J., 1964. Atlantic air-sea interaction. *Adv. Geophys.*, **10**, 1–82.

Blanke, B., M. Arhan, S. Speich and K. Pailler, 2001. Diagnosing and picturing the North Atlantic segment of the global conveyor belt by mean of an ocean general circulation model. *J. Phys. Oceanogr.*, **32**, 1430–1451.

Bleck, R. and S. Sun, 2004. Diagnostics of the oceanic thermohaline circulation in a coupled climate model. *Global and Planetary Change*, **40**, 233–248.

Broecker, W. S., 1991. The great ocean conveyor. *Oceanography*, **4**, 79–89.

Broecker, W. S., 1997. Thermohaline circulation, the archillis heel of our cliamte system: Will man-made co2 upset the current balance? *Science*, **278**, 1582–1588.

Bryan, K., 1969. A numerical method for the study of the circulation of the world ocean. *J. Computational Phys.*, **4**, 347–376.

Buck, A. L., 1981. New equations for computing vapor pressure and enhancement factor. *J. Appl. Met.*, **20**, 1527–1532.

Budyko, M. I., 1974. *Climate and life*. Academic Press, Int. Geophys. Ser.

Campin, J. M. and H. Goosse, 1999. Parameterization of density-driven downsloping flow for a coarse-resolution ocean model in z-coordinate. *Tellus*, **51A**, 412–430.

Cavalieri, D., 2002. A link between Fram Strait sea ice export and atmospheric planetary wave phase. *Geophys. Res. Lett.*, **29**, doi:10.1029/2002GL014684.

Cavalieri, D. and S. Häkkinen, 2001. Arctic climate and atmospheric planetary waves. *Geophys. Res. Lett.*, **28**, 791–794.

Cayan, D., 1992. Latent and sensible heat-flux anomalies over the northern oceans - driving the sea-surface temperature. *J. Phys. Oceanogr.*, **22**, 859–881.

Cox, G. F. N. and W. F. Weeks, 1974. Salinity variations in sea ice. *J. Glaciol.*, **13**, 109–120.

Curry, R., R. Dickson and I. Yashayaev, 2003. A change in the freshwater balance of the Atlantic Ocean over the past four decades. *Nature*, **426**, 826–829.

Curry, R. and M. McCartney, 2001. Ocean gyre circulation changes associated with the North Atlantic Oscillation. *J. Phys. Oceanogr.*, **31**, 3374–3400.

Curry, R., M. McCartney and J. T.M., 1998. Oceanic transport of subpolar climate signals to mid-depth subtropical waters. *Nature*, **391**, 575–577.

de Ruijter, W., A. Biastoch, S. Drijfhout, J. Lutjeharms, R. Matano, T. Pichevin, P. van Leeuwen and W. Weijer, 1999. Indian-Atlantic interocean exchange: Dynamics, estimation and impact. *J. Geophys. Res.*, **104 (C9)**, 20885–20910.

Defant, A., 1924. Die Schwankungen der atmosphärischen Zirkulation über dem Nord Atlantischen Ozean im 25-jährigen Zeitraum 1881-1905. *Geogr. Ann.*, **6**, 13–41.

Delworth, T., S. Manabe and R. Stouffer, 1993. Interdecadal variations of the thermohaline circulation in a coupled ocean-atmosphere model. *J. Climate*, **6**, 1993–2011.

Delworth, T. and M. Mann, 2000. Observed and simulated multidecadal variability in the Northern Hemisphere. *Clim. Dyn.*, **16**, 661–676.

Dengg, J., A. Beckmann and R. Gerdes, 1996. The Gulf Stream separation problem. In *The warmwatersphere of the North Atlantic Ocean* (edited by W. Krauss), pp. 253–290. Gebrüder Borntraeger, Berlin.

Deser, C., M. Holland, G. Reverdin and M. Timlin, 2002. Decadal variations in the Labrador Sea ice cover and North Atlantic sea surface temperatures. *J. Geophys. Res.*, **107**, art.no. 3035.

Dickson, R., T. Osborn, J. Hurrel, J. Meincke, J. Blindheim, B. Adlandsvik, T. Vinje, G. Alekseev and W. Maslowski, 2000. The arctic ocean response to the North Atlantic Circulation. *J. Climate*, **13**, 2671–2696.

Dickson, R., I. Yashayaev, J. Meincke, B. Turrell, S. Dye and J. Holfort, 2002. Rapid freshning of the deep North Atlantic Ocean over the past four decades. *Nature*, **416**, 832–836.

Dickson, R. R. and J. Brown, 1994. The production of North Atlantic deep water: Sources, rates and pathways. *J. Geophys. Res.*, **99**, 12319–12341.

Dickson, R. R., J. Meincke, S. A. Malmberg and A. J. Lee, 1988. The 'Great Salinity Anomaly' in the northern North Atlantic. *Prog. Oceanogr.*, **20**, 103–151.

Dickson, R. R., J. Meincke, P. Rhines and J. Swift, 1996. Longterm coordinated changes in the convective activity in the North Atlantic. *Prog. Oceanogr.*, **38**, 214–295.

Dickson, R. R., J. Meincke, I. Vassie, J. Jungclaus and S. Osterhus, 1999. Possible predictabillity in overflow from the Denmark Strait. *Nature*, **397**, 243–246.

Dietrich, G., K. Kalle, W. Krauss and G. Siedler, 1975. *Allgemeine Meereskunde*. Gebr. Borntraeger, Berlin, Stuugart.

Dümenil, L., K. Isele, H.-J. Liebscher, U. Schröder, M. Schumacher and K. Wilke, 1993. Discharge data from 50 selected rivers for GCM validation. Report 100, Max-Planck-Institut für Meteorologie, Hamburg, Germany.

Eicken, H., 1992. Salinity profiles of Antarctic sea ice: Field data and model results. *J. Geophys. Res.*, **97**, 15545–15557.

Emery, W., C. Fowler and J. Maslanik, 1997. Satellite-derived maps of Arctic and Antarctic sea ice motion: 1988-1994. *Geophys. Res. Lett.*, **24**, 897–899.

Frankignoul, C., G. de Coetlogon, T. Joyce and S. Dong, 2001. Gulf Stream variability and ocean-atmosphere interactions. *J. Phys. Oceanogr.*, **31**, 3516–3529.

Furevik, T., M. Bentsen, H. Drange, I. Kindem, N. Kvamsto and A. Sorteberg, 2002. Description and validation of the Bergen Climate Model: ARPEGE coupled with MICOM. *Clim. Dyn.*, p. submitted.

Ganachaud, A. and C. Wunsch, 2000. Improved estimates of global ocean circulation, heat transport and mixing from hydrographic data. *Nature*, **408**, 453–457.

Gent, P. R., F. Bryan, G. Danabsoglu, S. Doney, W. Holland, W. Large and J. McWilliams, 1997. The NCAR climate system model global ocean component. *J. Climate*, **11**, 1287–1306.

Gent, P. R., J. Willebrand, T. McDougall and J. C. McWilliams, 1995. Parameterizing eddy-induced tracer transports in ocean circulation models. *J. Phys. Oceanogr.*, **25**, 463–474.

Gordon, A. L., 1978. Deep Antarctic convection west of Maud Rise. *J. Phys. Oceanogr.*, **8**, 600–612.

Greatbatch, R., 2000. *The North Atlantic Oscillation*, Volume 14. Springer Verlag.

Griffies, S. M., 1998. The Gent-McWilliams skew flux. *J. Phys. Oceanogr.*, **28**, 831–841.

Haak, H., J. Jungclaus, U. Mikolajewicz and M. Latif, 2003. Formation and propagation of great salinity anomalies. *Geophys. Res. Lett.*, **30**, 1473, doi:10.1029/2003GLO17065.

Häkkinen, S., 1999. A simulation of thermohaline effects of a great salinty anomaly. *J. Climate*, **12**, 1781–1795.

Häkkinen, S., 2002. Freshning of the labrador sea surface water in the 1990s: Another great salinity anomaly? *Geophys. Res. Lett.*, **29**, 2232–2235.

Häkkinen, S. and A. Proshutinsky, 2004. Freshwater content variability in the arctic ocean. *Geophys. Res. Lett.*, **109**, doi:10.1029/2003JC0011940.

Hall, M. and H. Byrden, 1982. Direct estimates and mechanisms of ocean heat transport. *Deep Sea Res.*, **29**, 339–359.

Hansen, B., W. Turrell and S. Osterhus, 2001. Decreasing overflow from the Nordic Seas into the Atlantic Ocean through the Faroer Bank Channel since 1950. *Nature*, **411**, 927–930.

Hibler, W. D., 1979. A dynamic thermodynamic sea ice model. *J. Phys. Oceanogr.*, **9**, 815–846.

Hilmer, M., 2001. A model study of Arctic sea ice variability. Report 320, Reports of the Institute for Marine Research, University of Kiel, Germany.

Hilmer, M. and T. Jung, 2000. Evidence for a recentchange in the link between the north atlantic oscillation and arctic sea ice export. *Geophys. Res. Lett.*, **27**, 989–992.

Hoerling, M., H. J.Ww and T. Xu, 2001. Tropical origins for recent North Atlantic climate change. *Science*, **292**, 90–92.

Houghton, R. and M. Visbek, 2002. Quasi-decadal salinity fluctuations in the Labrador sea. *J. Phys. Oceanogr.*, **32**, 687–701.

Hurrel, J. W., 1995. Decadal trends in the North Atlantic Oscillation: regional temperatures and precipitation. *Science*, **269**, 676–679.

James, i. and P. James, 1989. Ultra-low-frequency variability in a simple atmospheric circulation model. *Nature*, **342**, 53–55.

Johannessen, O., C. Myrmehl, O. A.M. and H. T., 2002. Ice cover data analysis - Arctic. Technical Report 2, AICSEX.

Johannessen, O., E. Shalina and M. Miles, 1999. Satellite evidence for an Arctic sea ice cover in transformation. *Science*, **286**, 1937–1939.

Johns, W. E., T. N. Lee, R. J. Zantopp and E. Fillenbaum, 1997. Updated transatlantic heat flux at 26.5°N. *WOCE Newsletter*, **27**, 15–22.

Jones, P. D., T. Jonsson and D. Wheeler, 1997. Extension to the North Atlantic Oscillaion using early instrumental pressure observations from Gibraltar ans South-West Iceland. *Int. J. Climatol.*, **17**, 1433–1450.

Jungclaus, J., H. Haak, M. Latif and U. Mikolajewicz, 2004. Arctic-North Atlantic interactions and multidecadal variability of the Meridional Overturning Circulation. *J. Climate*, pp. –.

Kalnay, E. et al., 1996. The NCEP/NCAR 40 year-reanalysis project. *Bull. Amer. Meteor. Soc.*, **77**, 437–470.

Killworth, P. D. and N. R. Edwards, 1999. A turbulent bottom boundary layer code for use in numerical ocean models. *J. Phys. Oceanogr.*, **29**, 1221–1238.

Killworth, P. D., D. A. Smeed and A. J. G. Nurser, 2000. The effects on ocean models of relaxation toward observations at the surface. *J. Phys. Oceanogr.*, **30**, 160–174.

Klinger, B. A., J. Marshall and U. Send, 1996. Representation of convective plumes by vertical adjustment. *J. Geophys. Res.*, **101**, 18175–18182.

Kushnir, Y., 1994. Interdecadal variations in North Atlantic sea surface temperature and associated atmospheric conditions. *J. Climate*, **7**, 141–157.

Kwok, R. and D. Rothrock, 1999. Variability of Fram Strait ice flux and North Atlantic Oscillation. *J. Geophys. Res.*, **104**, 5177–5189.

Large, W. G. and S. Pond, 1982. Sensible and latent heat flux measurements over the ocean. *J. Phys. Oceanogr.*, **12**, 464–482.

Latif, M., K. Arpe and E. Roeckner, 2000. Oceanic control of decadal north atlantic sea level pressure variability in winter. *Geophys. Res. Lett.*, **27**, 727–730.

Latif, M., E. Roeckner, M. Botzet, M. Esch, H. Haak, S. Hagemann, J. Jungclaus, S. Legutke, S. Marsland, U. Mikolajewicz and J. Mitchell, 2004. Reconstructing, monitoring and predicting multi-decadal-scale changes in the north atlantic thermohaline circulation with sea surface temperature. *J. Climate*, p. in press.

Lazier, J. R. N., 1995. The salinity decrease in the labrador sea over the past thirty years. In *Natural Climate Variability on Decade-to-Century time scales* (edited by D. G. Martinson, K. Bryan, M. Ghil, M. M. Hall, T. M. Karl, E. S. Sarachik, S. Sorooshian and L. Talley), pp. 295–304. National Academy Press, Washington, D.C.

Legutke, S. and E. Maier-Reimer, 1999. Climatology of the HOPE-G global ocean general circulation model. Technical Report 21, German Climate Computer Center (DKRZ), Hamburg, Germany.

Levitus, S., T. P. Boyer, M. E. Conkright, T. O'Brien, J. Antonov, C. Stephens, L. Stathoplos, D. Johnson and R. Gelfeld, 1998. World Ocean Database 1998: Volume 1: Introduction. NOAA Atlas NESDIS 18, Ocean Climate Laboratory, National Oceanographic Data Center, U.S. Gov. Printing Office, Wash., D.C.

Macdonald, A. M. and C. Wunsch, 1996a. An estimate of global ocean circulation and heat fluxes. *Nature*, **382**, 436–439.

Macdonald, A. M. and C. Wunsch, 1996b. Oceanic estimates of global ocean heat transport. *WOCE Newsletter*, **24**, 5–6.

Maier-Reimer, E., U. Mikolajewicz and K. Hasselmann, 1993. Mean circulation of the Hamburg LSG OGCM and its sensitivity to the thermohaline surface forcing. *J. Phys. Oceanogr.*, **23**, 731–757.

Mann, M., R. Bradley and M. Hughes, 1998. Global-scale temperature patterns and climate forcing over the past six centuries. *Nature*, **392**, 779 – 787; doi:10.1038/338591999–2018.

Marotzke, J., 1991. Influence of convective adjustment on the stability of the thermohaline circulation. *J. Phys. Oceanogr.*, **21**, 903–907.

Marsland, S. and J.-O. Wolff, 2001. On the sensitivity of southern ocean sea ice to the surface freshwater flux: a model study. *J. Geophys. Res.*, **106**, 2723–2741.

Marsland, S. J., H. Haak, J. H. Jungclaus, M. Latif and F. Roeske, 2003. The Max-Planck-Institute global ocean/sea ice model with orthogonal curvilinear coordinates. *Ocean Modelling*, **5**, 91–127.

Martinson, D., P. Killworth and A. Gordon, 1981. A convective model for the weddell polynya. *J. Phys. Oceanogr.*, **11**, 466–488.

Mauritzen, C., 1996. Production of dense overflow waters feeding the North Atlantic across the Greenland-Scotland Ridge. part 1: Evidence for a revised circulation scheme. *Deep-Sea Research*, **43**, 769–806.

Mauritzen, C. and S. Haekkinen, 1997. Influence of sea ice on the thermohaline circulation in the Arctic-North Atlantic Ocean. *Geophys. Res. Lett.*, **24**, 3257–3260.

McCartney, M. S., 1992. Recirculating components to the deep boundary current in the northern North Atlantic. *Prog. Oceanogr.*, **29**, 283–383.

McCartney, M. S. and R. Curry, 1993. Transequatorial flow of Antarctic Bottom Water in the western Atlantic ocean: Abyssal geostrophy at the equator. *J. Phys. Oceanogr.*, **23**, 1264–1276.

Meincke, J., B. Rudels and F. H.J., 1997. The Arctic Ocean Nordic Seas thermohaline system. *J. Mar. Res.*, **54**, 283–299.

Nowlin, W. D. J. and J. M. Klinck, 1986. The physics of the Antarctic Circumpolar Current. *Rev. Geophys.*, **24**, 469–491.

Oberhuber, J., 1988. An atlas based on the COADS data set: The budget of heat, buoyancy and turbulent kinetic energy at the surface of the global ocean. Technical Report 15, Max-Planck Institut für Meteorologie (MPI).

Oberhuber, J. M., 1993. Simulation of the Atlantic circulation with a coupled sea ice-mixed layer-isopycnal general circulation model. Part I: Model description. *J. Phys. Oceanogr.*, **23**, 808–829.

Pacanowski, R. C. and S. G. H. Philander, 1981. Parameterization of vertical mixing in numerical-models of tropical oceans. *J. Phys. Oceanogr.*, **11**, 1443–1451.

Parkinson, C., D. Cavalieri, H. Gloerson, P. Zwally and J. Cosimo, 1999. Arctic sea ice extent, areas and trends, 1978-1996. *J. Geophys. Res.*, **104**, 20837–20856.

Pickart, R., M. Spall, M. Ribergaard, G. Moore and R. Milliff, 2003. Deep convection in the Irminger Sea forced by the Greenland tip jet. *Nature*, **424**, 152–156.

Price, J. F. and M. Baringer, 1994. Outflows and deep water productions by marginal seas. *Prog. Oceanogr.*, **25**, 162–200.

Proshutinsky, A., R. Bourke and F. McLaughlin, 2002. The role of the Beaufort Gyre in Arctic climate variability: seasonal to decadal climate scales. *Geophys. Res. Lett.*, **29**, doi:10.1029/2002GL015847.

Proshutinsky, A. and M. Johnson, 1997. Two circulation regimes of the wind-driven Arctic Ocean. *J. Geophys. Res.*, **102**, 12493–12514.

Rahmstorf, S., 1996. On the freshwater forcing and transport of the Atlantic thermohaline circulation. *Clim. Dyn.*, **412**, 799–811.

Raible, C., U. Luksch, K. Fraedrich and R. Voss, 2001. North Atlantic decadal regimes in a coupled gcm simulation. *Clim. Dyn.*, **18**, 321–330.

Redi, M. H., 1982. Oceanic isopycnal mixing by coordinate rotation. *J. Phys. Oceanogr.*, **12**, 1154–1158.

Rintoul, S. R. and C. Wunsch, 1991. Mass, heat, oxygen and nutrient fluxes and budgets in the North Atlantic Ocean. *Deep Sea Res.*, **38, Suppl. 1**, S355–S377.

Roach, A., K. Aagaard, C. Pease, S. SALO, W. T., V. Pavlov and M. KULAKOV, 1995. Direct measurements of transport and water properties through the Bering Strait. *J. Geophys. Res.*, **100 (C9)**, 18443–18457.

Rodgers, J., 1990. Patterns of low frequency monthly sea level pressure variability (1899-1996) ans associated wave cyclone frequencies. *J. Climate*, **3**, 1364–1379.

Rodwell, M., D. Rowell and C. Folland, 1999. Oceanic forcing of the wintertime North Atlantic Oscillation and european climate. *Nature*, **398**, 320–323.

Roemmich, D. and C. Wunsch, 1985. Two transatlantic sections: meridional circulation and heat flux in the subtropical north atlantic ocean. *Deep Sea Res.*, **32**, 619–664.

Roether, W., B. Manca, B. Klein, D. Bregant, D. Georgopoulos, V. Beitzel, V. Kovacevic and A. Luchetta, 1996. Recent changes in eastern Mediterranean Deep Waters. *Science*, **271**, 333–335.

Rothrock, D., Y. Yu and G. Maycut, 1999. Thinning of Arctic sea ice cover. *Geophys. Res. Lett.*, **26**, 3469–3472.

Saenko, O., E. Wiebe and A. Weaver, 2003. North Atlantic response to the above-normal export of sea ice from the Arctic. *J. Geophys. Res.*, **108**, 3224, doi:10.1029/2001JCO01166.

Schmith, T. and C. Hansen, 2003. Fram Strait ice export during the nineteenth and twentieth centuries reconstructed from a multiyear sea ice index from southwestern Greenland. *J. Climate*, **16**, 2782–2791.

Semtner, A. J., 1976. A model for the thermodynamic growth of sea ice in numerical investigations of climate. *J. Phys. Oceanogr.*, **6**, 379–389.

Speer, K. and W. Zenk, 1993. The flow of Antarctic Bottom Water into the Brazil Basin. *J. Phys. Oceanogr.*, **23**, 2667–2682.

Steele, M., D. Thomas, D. Rothrock and S. Matin, 1996. A simple model study of the Arctic ocean freshwater balance. *J. Geophys. Res.*, **101**, 20833–20848.

Sutton, R. and M. Allen, 1997. Decadal predictability of north atlantic sea surface temperatures and climate. *Nature*, **388**, 563–567.

Sutton, R. and D. Hodson, 2003. Influence of the ocean on North Atlantic climate variability 1871-1999. *J. Climate*, **16**, 3296–3313.

Talley, L., 2002. Shallow, intermediate, and deep overturning components of the global heat budget. *J. Phys. Oceanogr.*, **33**, 530–560.

Terray, L., S. Valke and A. Piacentini, 1998. Oasis 2.2 ocean atmosphere sea ice soil users guide and reference manual. Technical Report 05, Centre Europeen de Recherche et de Formation en calcul scientifique avance (CERFACS).

Thomson, D. W. J. and J. M. Wallace, 1998. The Arctic Oscillation signature in the wintertime geopotential height and temperature field. *Geophys. Res. Lett.*, **25**(9), 1297–1300.

Timmermann, A., M. Latif, R. Voss and A. Grötzner, 1998. Northern hemisphere intedecadal variability. *J. Climate*, **11**, 1906–1931.

Trenberth, K. E. and A. Solomon, 1994. The global heat balance: heat transports in the atmosphere and ocean. *Clim. Dyn.*, **10**, 107–134.

UNESCO, 1983. Algorithms for computation of fundamental properties of seawater. UNESCO Technical Papers in Marine Science 44, UNESCO.

Vinje, T., 2001. Fram Strait ice fluxes and atmospheric circulation: 1950-2000. *J. Climate*, **14**, 3508–3517.

Vinje, T., N. Nordlund and A. Kvambek, 1998. Monitoring ice thickness in Fram Strait. *J. Geophys. Res.*, **103**, 10437–10449.

Wadhams, P. and N. Davis, 2000. Further evidence of ice thinning in the Arctic Ocean. *Geophys. Res. Lett.*, **27**, 3973–3975.

Walker, G. T. and E. W. Bliss, 1932. World weather v. *Mem. Roy. Met. Soc.*, **4**, 53–84.

Walter, K. and H. Graf, 2002. On the changing nature of the regional connection between the North Atlantic Oscillation and sea surface temperature. *J. Geophys. Res.*, **107**, doi:10.1029/2001JD000850.

Wanner, H., S. Brönnimann, C. Casty, D. Gyalistras, L. Luterbacher, C. Schmutz, D. Stephenson and E. Xoplaki, 2001. North Atlantic Oscillation - concepts and studies. *Surveys in Geophysics*, **22**, 322–382.

Winsor, P., 2001. Arctic sea ice thickness remained constant during the 1990th. *Geophys. Res. Lett.*, **28**, 1039–1041.

Wu, P., R. Wood and P. Stott, 2004. Does the recent freshning trend in the North Atlantic indicate a weakning thermohaline circulation? *Geophys. Res. Lett.*, **31**, doi:10.10.29/2003GL018584.

Zhang, D., M. McPhaden and E. Williams, 2003. Oberservational evidence for flow between the subtropical and tropical Atlantic: the Atlantic Subtropical Cells. *J. Phys. Oceanogr.*, p. submitted.

Acknowledgments

I would like to thank Prof. Dr. Lennart Bengtsson and Prof. Dr. Guy Brasseur for making it possible to write this thesis at MPI in Hamburg. I thank Prof. Dr. Mojib Latif, Prof. Dr. Jens Meincke, Dr. Uwe Mikolajewicz and Dr. Ernst Maier-Reimer for their supervision and steady and patient support of my work. I also thank Dr. Johann Jungclaus and my other colleagues for numerous fruitful discussions which gave me new ideas and insights. Special thanks to my wife Christine for her enormous patience and support. Special thanks also to Dr. Noel Keenlyside and Jürgen Bader for proof-reading the manuscript.

Financial support for this thesis was provided in the framework of SFB 512 “Tiefdruckgebiete und Klimasystem des Nordatlantiks” of the University of Hamburg.

MPI-Examensarbeit-Referenz:

Examensarbeit Nr. 1-79 bei Bedarf bitte Anfragen:
MPI für Meteorologie, Abtlg.: PR, Bundesstr. 55, 20146 Hamburg

Examensarbeit Nr. 80 November 2000	**Vertikalmessungen der Aerosolextinktion und des Ozons mit einem UV-Raman-Lidar** Volker Matthias
Examensarbeit Nr. 81 Dezember 2000	**Photochemical Smog in Berlin-Brandenburg: An Investigation with the Atmosphere-Chemistry Model GESIMA** Susanne E. Bauer
Examensarbeit Nr. 82 Juli 2001	**Komponenten des Wasserkreislaufs in Zyklonen aus Satellitendaten – Niederschlagsfallstudien-** Klepp Christian-Philipp
Examensarbeit Nr. 83 Juli 2001	**Aggregate models of climate change: development and applications** Kurt Georg Hooss
Examensarbeit Nr. 84 Februar 2002	**Ein Heterodyn-DIAL System für die simultane Messung von Wasserdampf und Vertikalwind: Aufbau und Erprobung** Stefan Lehmann
Examensarbeit Nr. 85 April 2002	**Der Wasser- und Energiehaushalt der arktischen Atmosphäre** Tido Semmler
Examensarbeit Nr. 86 April 2002	**Auswirkungen der Assimilation von Meereshöhen-Daten auf Analysen und Vorhersagen von El Niño** Sigrid Schöttle
Examensarbeit Nr. 87 Juni 2002	**Atmospheric Processes in a young Biomass Burning Plume - Radiation and Chemistry** Jörg Trentmann
Examensarbeit Nr. 88 August 2002	**Model Studies of the Tropical 30 to 60 Days Oscillation** Stefan Liess
Examensarbeit Nr. 89 Dezember 2002	**Influence of Sub-Grid Scale Variability of Clouds on the Solar Radiative Transfer Computations in the ECHAM5 Climate Model** Georg Bäuml
Examensarbeit Nr.90 Mai 2003	**Model studies on the response of the terrestrial carbon cycle to climate change and variability** Marko Scholze
Examensarbeit Nr.91 Juni 2003	**Integrated Assessment of Climate Change Using Structural Dynamic Models** Volker Barth

MPI-Examensarbeit-Referenz:

Examensarbeit Nr. 1-79 bei Bedarf bitte Anfragen:
MPI für Meteorologie, Abtlg.: PR, Bundesstr. 55, 20146 Hamburg

Examensarbeit Nr.92 Juli 2003	**Simulations of Indonesian Rainfall with a Hierarchy of Climate Models** Edvin Aldrian
Examensarbeit Nr.93 Juli 2003	**ENSO Teleconnections in High Resolution AGCM Experiments** Ute Merkel
Examensarbeit Nr.94 Juli 2003	**Application and Development of Water Vapor DIAL Systems** Klaus Ertel

ISSN 1614-1199